

# UC Merced

## UC Merced Electronic Theses and Dissertations

### Title

Atmospheric pressure dielectric barrier discharge for environmental applications: Case studies on irrigation water enrichment and dry methane reforming

### Permalink

<https://escholarship.org/uc/item/3n7315xz>

### Author

Buendia, Jose Alejandro

### Publication Date

2018

### Supplemental Material

<https://escholarship.org/uc/item/3n7315xz#supplemental>

Peer reviewed|Thesis/dissertation

UNIVERSITY OF CALIFORNIA, MERCED

**Atmospheric pressure dielectric barrier discharge for  
environmental applications: Case studies on irrigation  
water enrichment and dry methane reforming**

A Thesis submitted in partial satisfaction of the requirements  
for the degree of Master of Engineering

in

Mechanical Engineering

by

Jose Alejandro Buendia

Committee in charge:

Professor Venkattraman Ayyaswamy, Chair  
Professor Gerardo Diaz  
Professor Po-Ya Abel Chuang

2018



This Thesis of Jose Alejandro Buendia, titled Atmospheric pressure dielectric barrier discharge for environmental applications: Case studies on irrigation water enrichment and dry methane reforming, is approved:

---

Venkattraman Ayyaswamy, Chair

Date

---

Gerardo Diaz

Date

---

Po-Ya Abel Chuang

Date

University of California, Merced

2018

To my family and friends.

## ACKNOWLEDGEMENTS

First and foremost, I like to thank my advisor Dr. Venkattraman Ayyaswamy for his incredible patience, support and guidance. He has been invaluable source of support and patience when I needed it most. Without him this thesis would not have been possible. I don't know what I did to deserve such a great advisor but I am grateful for everything he has done for me.

My sincere appreciation is extended to my other dissertation committee members: Dr. Po-Ya Abel Chuang and Dr. Gerardo Diaz for agreeing to be part of my committee and for all their invaluable guidance and feedback. Also, I take this opportunity to express gratitude to UC Merced faculty members for their help and support.

Secondly, I like to thank all my friends who have been with me throughout the highs and lows, who have picked me up and pushed (sometimes thrown) me forward, and who have always seen something great in me. Specifically, I like to thank Anibal Espinoza, Alejandro Lopez, Miriam Yañez, Julio Lopez, Steven Islas, Ala'aldin Alafaghani, Abhishek Kumar Verma, Angela Macedo Andrade, Muhammad Ali Maimaitiaili, Donglei Yang and Edgar Perez-Lopez. You have all provide me with invaluable support, encouragement, and love throughout these three years. I would also like to thank Andres Munoz Hernandez for his advise in navigating graduate school life.

Lastly but certainly not least, I like to thank my family for their crazy amount of love and encouragement they have giving me throughout my life. My parents, Jose and Alicia, have always provide me with everything I need to succeed in life and their sacrifices have allowed me to pursue my goals. My sister, Laura, was the first person to ever help me with my homework and even today she is still helping me whenever I need her. I could not have had a better sister. Without my advisor, friends, and family none of what I've accomplished would have been possible. I am forever in your debt.

Permission to use copyrighted material (Figs. 1-8) was granted by AIP Publishing, Elsevier, John Wiley and Sons, National Academic Press, and IOP Publishing.

## ABSTRACT

Environment applications of atmospheric pressure dielectric barrier discharge (DBD) for irrigation water enrichment and dry methane reforming were studied. The treatment of distilled water with varying amounts of dissolved sodium bicarbonate (representing alkalinity) is considered using an atmospheric pressure electrical discharge. The discharge ignited between a capillary tube (used as powered electrode) and a ground electrode wrapped around the beaker holding the treated water is shown to be comprised of streamers propagating at about 200 m/s. The streamer interaction with water is shown to lead to a decrease in pH and an increase in nitrate concentration due to the injection of  $NO_2$ . The pH variation with time is shown to be similar to a titration curve for acid-base neutralization with final pH values around 3 for 22 minutes of treatment. The nitrate ion concentration increase with time is consistent with a two-rate system-level model that is characterized by two asymptotic rates for  $NO_2$  injection by the plasma. The two asymptotic rates are calibrated to be about  $4.05 \mu\text{mol}/\text{min}$  and  $33.75 \mu\text{mol}/\text{min}$  with the transition between the two rates occurring at the breakeven time that is representative of the time required for all dissolved bicarbonate to be consumed by the plasma treatment. Another system-level model that is based on the observed pH variation is also considered for comparison with measured data. While both system-level models have discrepancies with the measurements, the two-rate model based on the nitrate ion concentration is concluded to be more accurate for determining the  $NO_2$  injection rates. The discrepancies are attributed to the simplicity of the system-level models considered here where the effect of the plasma is completely represented by the injection of just one chemical species in  $NO_2$ . Nevertheless, the proposed system-level models could greatly assist in the design of larger plasma treatment systems with specified alkalinity, pH and nitrate ion levels for irrigation water.

Plasma-assisted biogas conversion was studied and primary results were demonstrated. As in the plasma-assisted water treatment application, a unique and specific atmospheric pressure DBD was designed and built. The DBD was designed with two stainless steel flanges connected by a quartz tube (dielectric). A copper capillary needle was used as the ground electrode whereas a copper sheet wrapped around the dielectric was used as the power electrode. The DBD went through a few modifications for the purpose of improving the conversion of methane to hydrogen. Conversion of methane to hydrogen was as high as 50 % although some results were as low as 2 %.

# TABLE OF CONTENTS

<b>ACKNOWLEDGEMENTS</b> . . . . .	<b>ii</b>
<b>ABSTRACT</b> . . . . .	<b>iii</b>
<b>LIST OF FIGURES</b> . . . . .	<b>vii</b>
<b>LIST OF TABLES</b> . . . . .	<b>xv</b>
<b>1 INTRODUCTION</b> . . . . .	<b>1</b>
1.1 Description of Plasmas . . . . .	1
1.2 Emerging Applications of Non-Thermal Plasmas . . . . .	5
1.2.1 Plasma Medicine . . . . .	5
1.2.2 Plasma-assisted Combustion . . . . .	8
1.2.3 Plasma-assisted Surface Modification . . . . .	9
1.3 Plasmas in Water Treatment . . . . .	11
1.4 Plasmas in Carbon Reforming . . . . .	14
1.5 Research Goals and Objectives . . . . .	16
1.6 Outline of Thesis . . . . .	16
<b>2 EXPERIMENTAL SET-UP AND COMPUTATIONAL ANALYSIS</b> . . . . .	<b>17</b>
2.1 Experimental Set-up for Water Treatment . . . . .	17
2.2 Computational Analysis . . . . .	19
2.3 Experimental Set-up for Carbon Reforming . . . . .	28

<b>3</b>	<b>RESULTS AND DISCUSSION FOR WATER TREATMENT . .</b>	<b>34</b>
3.1	Progression of DBD Reactor Design and Results . . . . .	34
3.1.1	Reactor 1 . . . . .	34
3.1.1.1	Design . . . . .	34
3.1.1.2	pH Results . . . . .	36
3.1.2	Reactor 2 . . . . .	36
3.1.2.1	Design . . . . .	36
3.1.2.2	pH Results . . . . .	37
3.1.3	Reactor 3 . . . . .	37
3.1.3.1	Design . . . . .	37
3.1.3.2	pH Results . . . . .	38
3.1.4	Reactor 3.5 (Volume Based Results) . . . . .	38
3.1.4.1	Design . . . . .	38
3.1.4.2	pH Results . . . . .	39
3.1.5	Reactor 4 . . . . .	40
3.1.5.1	Design . . . . .	40
3.1.5.2	pH Results . . . . .	40
3.1.6	Reactor 5: Versions 1 and 2 . . . . .	42
3.1.6.1	Design . . . . .	42
3.1.6.2	pH Results . . . . .	42
3.2	Final Results & Discussion . . . . .	44
3.2.1	Electrical Characteristics . . . . .	44
3.2.2	pH and $NO_3^-$ Results . . . . .	46
3.2.3	System-Level Model . . . . .	47

3.2.4	0 mg, 1 mg, & 2 mg . . . . .	49
3.2.5	5 mg & 10 mg . . . . .	51
3.2.6	15 mg, 20 mg, & 50 mg . . . . .	53
3.2.7	Post Treatment . . . . .	56
3.2.8	Baseline Results . . . . .	57
3.3	Summary . . . . .	58
<b>4</b>	<b>METHANE REFORMING USING A DIELECTRIC BARRIER DISCHARGE . . . . .</b>	<b>73</b>
4.1	Calibration of Gas Chromatograph . . . . .	73
4.2	Preliminary Results & Discussion . . . . .	75
4.3	Outlook . . . . .	78
<b>5</b>	<b>CONCLUSION &amp; FUTURE RECOMMENDATIONS . . . . .</b>	<b>83</b>
	<b>BIBLIOGRAPHY . . . . .</b>	<b>85</b>
<b>APPENDIX</b>		
<b>A</b>	<b>MATLAB CODES . . . . .</b>	<b>101</b>
A.1	Primary Codes . . . . .	102
A.2	System-Level Model Codes . . . . .	107

## LIST OF FIGURES

<b>1.1</b>	Schematic of a typical phase diagram and corresponding ionized states of matter. Reprinted from [1] with the permission of AIP Publishing. . . . .	2
<b>1.2</b>	Schematic of electron temperature and number density for different discharges, Corona, direct current (DC) discharge, microwave (MW) discharge; dielectric barrier discharge (DBD), radio-frequency discharge (RF), glow discharge, gliding arc, nanosecond pulsed discharge (NSD), arc, magneto-hydrodynamic discharge (MHD), and flame. Reprinted from [2] with the permission of Elsevier. . . .	3
<b>1.3</b>	Dynamics of the healing of venous trophic ulcer during $NO_2$ therapy. Reprinted from [5] with the permission of John Wiley and Sons. . .	6
<b>1.4</b>	Healing dynamics of the festered burn wound in process of $NO_2$ therapy: a) prior to the beginning of treatment and b) after five sessions of $NO_2$ therapy. Reprinted from [5] with the permission of John Wiley and Sons. . . . .	7
<b>1.5</b>	a) Configuration of the tooth bleaching experiment and b) schematic of the plasma jet and of the process. Reprinted from [14] with the permission of John Wiley and Sons. . . . .	7
<b>1.6</b>	a) Facial appearance before and b) 3 months after plasma skin regeneration, with improvement in pigmentation and skin texture. Reprinted from [5] with the permission of John Wiley and Sons. . .	8



<b>1.7</b>	Plasma-coated jet turbine blade (02), Diamond like plasma CVD eyeglass coating (04), plasma-processing microelectronics (14), plasma-treated polymers (16), plasma-treated textiles (17), plasma-treated heart stent (18), and plasma-sputtered window glazing are various different examples of plasma material processing. NOTE: CVD, chemical vapor deposition; HID, high-intensity discharge; LED, light- emitting diode; LCD, liquid crystal display. Reprinted from [62] with the permission of National Academic Press	10
<b>1.8</b>	Schematic diagram of some of the most important species and mechanisms for an argon/humid air plasma in contact with water. Reprinted from [120] with the permission of IOP Publishing copyright 2014. . . . .	13
<b>2.1</b>	Needle design. . . . .	18
<b>2.2</b>	Entire system. . . . .	18
<b>2.3</b>	PVM500 Plasma Power Generator for Conventional and Complex Loads. . . . .	19
<b>2.4</b>	Brooks Instrument Flow Meter . . . . .	19
<b>2.5</b>	90 degree elbow connection with compression fittings. . . . .	20
<b>2.6</b>	1/8 inch compression fittings. . . . .	20
<b>2.7</b>	Schematic of the entire water treatment system. . . . .	21
<b>2.8</b>	Schematic of the entire carbon reforming system. . . . .	29
<b>2.9</b>	Carbon reforming system . . . . .	30
<b>2.10</b>	Gas Chromatograph (GC) 2014 . . . . .	30
<b>2.11</b>	The top end connection design. . . . .	31
<b>2.12</b>	The bottom end connection design . . . . .	31

<b>2.13</b>	The plasma reactor is made of two custom design end connections, quartz tube, a copper sheet wrapped around the quartz tube, and inner 1/8 inch copper rod, and 1/8 inch compression fittings. . . . .	32
<b>2.14</b>	Mass flow controllers. The top is the rated for carbon dioxide and the bottom is rated for methane. . . . .	32
<b>2.15</b>	Hydrogen and methane purifiers. . . . .	33
<b>2.16</b>	Moisture filter was used between the outlet of the plasma reactor and GC. . . . .	33
<b>3.1</b>	The four reactors used before settling on the final design (discussed in Chapter 2). . . . .	35
<b>3.2</b>	Reactor 1 in operation. . . . .	35
<b>3.3</b>	Reactor 1 pH variation as a function of treatment time for distilled water. . . . .	36
<b>3.4</b>	Reactor 2 in operation. . . . .	37
<b>3.5</b>	Comparison of reactors 1-2 pH variation as a function of treatment time for distilled water. . . . .	38
<b>3.6</b>	Reactor 3 in operation. . . . .	39
<b>3.7</b>	Comparison of reactors 1-3 pH variation as a function of treatment time for distilled water. . . . .	40
<b>3.8</b>	Comparison of measured, model prediction, and based line of pH variation as a function of treatment volume for distilled water with 10 mg of dissolved sodium bicarbonate. . . . .	41
<b>3.9</b>	Reactor 4 in operation. . . . .	41
<b>3.10</b>	Comparison of all reactor 1-4 pH variation as a function of treatment time for distilled water. . . . .	42
<b>3.11</b>	Comparison of all reactors pH variation as a function of treatment time for distilled water. . . . .	43

<b>3.12</b>	Comparison of $NO_2$ rate of reactor 3 vs reactor 5 . . . . .	43
<b>3.13</b>	A representative image of the atmospheric pressure streamer discharge in action during a typical water treatment experiment. . .	45
<b>3.14</b>	Time history of current through the atmospheric pressure streamer discharge set-up prior to ignition. The frequency of the sinusoidal current was obtained as 28 kHz. . . . .	45
<b>3.15</b>	Time history of current through the atmospheric pressure streamer discharge set-up during the water treatment by streamers. The frequency of the each sinusoidal sub-cycle was obtained as 28 kHz with the spike in current observed at a frequency of about 7 kHz. .	46
<b>3.16</b>	Variation of pH of the treated water as a function of treatment time by atmospheric pressure streamer discharges for various masses of dissolved sodium bicarbonate ranging from 0 mg to 20 mg. The 50 mg data is not shown in this plot but is presented during analysis using the system-level model. . . . .	48
<b>3.17</b>	Variation of $[NO_3^-]$ in the treated water as a function of treatment time by atmospheric pressure streamer discharges for various masses of dissolved sodium bicarbonate ranging from 0 mg to 20 mg. The 50 mg data is not shown in this plot but is presented during analysis using the system-level model. . . . .	49
<b>3.18</b>	Comparison of measured and system-level model predictions of $d(NO_2)/dt$ variation as a function of treatment time for distilled water with 0 mg of dissolved sodium bicarbonate. . . . .	51
<b>3.19</b>	Comparison of measured and system-level model predictions of pH variation as a function of treatment time for distilled water with 0 mg of dissolved sodium bicarbonate. . . . .	52
<b>3.20</b>	Comparison of measured and system-level model predictions of $[NO_3^-]$ variation as a function of treatment time for distilled water with 0 mg of dissolved sodium bicarbonate. . . . .	53
<b>3.21</b>	Comparison of measured and system-level model predictions of $d(NO_2)/dt$ variation as a function of treatment time for distilled water with 1 mg of dissolved sodium bicarbonate. . . . .	54

<b>3.22</b>	Comparison of measured and system-level model predictions of pH variation as a function of treatment time for distilled water with 1 mg of dissolved sodium bicarbonate. . . . .	55
<b>3.23</b>	Comparison of measured and system-level model predictions of $[NO_3^-]$ variation as a function of treatment time for distilled water with 1 mg of dissolved sodium bicarbonate. . . . .	56
<b>3.24</b>	Comparison of measured and system-level model predictions of $d(NO_2)/dt$ variation as a function of treatment time for distilled water with 2 mg of dissolved sodium bicarbonate. . . . .	57
<b>3.25</b>	Comparison of measured and system-level model predictions of pH variation as a function of treatment time for distilled water with 2 mg of dissolved sodium bicarbonate. . . . .	58
<b>3.26</b>	Comparison of measured and system-level model predictions of $[NO_3^-]$ variation as a function of treatment time for distilled water with 2 mg of dissolved sodium bicarbonate. . . . .	59
<b>3.27</b>	Comparison of measured and system-level model predictions of $d(NO_2)/dt$ variation as a function of treatment time for distilled water with 5 mg of dissolved sodium bicarbonate. . . . .	60
<b>3.28</b>	Comparison of measured and system-level model predictions of pH variation as a function of treatment time for distilled water with 5 mg of dissolved sodium bicarbonate. . . . .	60
<b>3.29</b>	Comparison of measured and system-level model predictions of $[NO_3^-]$ variation as a function of treatment time for distilled water with 5 mg of dissolved sodium bicarbonate. . . . .	61
<b>3.30</b>	Comparison of measured and system-level model predictions of $d(NO_2)/dt$ variation as a function of treatment time for distilled water with 10 mg of dissolved sodium bicarbonate. . . . .	61
<b>3.31</b>	Comparison of measured and system-level model predictions of pH variation as a function of treatment time for distilled water with 10 mg of dissolved sodium bicarbonate. . . . .	62

<b>3.32</b>	Comparison of measured and system-level model predictions of $[NO_3^-]$ variation as a function of treatment time for distilled water with 10 mg of dissolved sodium bicarbonate. . . . .	62
<b>3.33</b>	Comparison of measured and system-level model predictions of $d(NO_2)/dt$ variation as a function of treatment time for distilled water with 15 mg of dissolved sodium bicarbonate. . . . .	63
<b>3.34</b>	Comparison of measured and system-level model predictions of pH variation as a function of treatment time for distilled water with 15 mg of dissolved sodium bicarbonate. . . . .	64
<b>3.35</b>	Comparison of measured and system-level model predictions of $[NO_3^-]$ variation as a function of treatment time for distilled water with 15 mg of dissolved sodium bicarbonate. . . . .	64
<b>3.36</b>	Comparison of measured and system-level model predictions of $d(NO_2)/dt$ variation as a function of treatment time for distilled water with 20 mg of dissolved sodium bicarbonate. . . . .	65
<b>3.37</b>	Comparison of measured and system-level model predictions of pH variation as a function of treatment time for distilled water with 20 mg of dissolved sodium bicarbonate. . . . .	65
<b>3.38</b>	Comparison of measured and system-level model predictions of $[NO_3^-]$ variation as a function of treatment time for distilled water with 20 mg of dissolved sodium bicarbonate. . . . .	66
<b>3.39</b>	Comparison of measured and system-level model predictions of $d(NO_2)/dt$ variation as a function of treatment time for distilled water with 50 mg of dissolved sodium bicarbonate. . . . .	66
<b>3.40</b>	Comparison of measured and system-level model predictions of pH variation as a function of treatment time for distilled water with 50 mg of dissolved sodium bicarbonate. . . . .	67
<b>3.41</b>	Comparison of measured and system-level model predictions of $[NO_3^-]$ variation as a function of treatment time for distilled water with 50 mg of dissolved sodium bicarbonate. . . . .	67

<b>3.42</b>	Measured pH variation with time (up to 60 minutes) after treatment for various masses of dissolved sodium bicarbonate. . . . .	68
<b>3.43</b>	Measured pH variation with time (up to 14 days) after treatment for various masses of dissolved sodium bicarbonate. . . . .	68
<b>3.44</b>	Measured $NO_3^-$ concentration variation with time (up to 60 minutes) after treatment for various masses of dissolved sodium bicarbonate. . . . .	69
<b>3.45</b>	Measured $NO_3^-$ concentration variation with time (up to 14 days) after treatment for various masses of dissolved sodium bicarbonate. . . . .	69
<b>3.46</b>	Baseline pH variation with time (over 22 min). . . . .	70
<b>3.47</b>	Baseline pH variation with time (up to 60 mins). . . . .	70
<b>3.48</b>	Baseline pH variation with time (up to 14 days). . . . .	71
<b>3.49</b>	Baseline $NO_3^-$ concentration variation with time (over 22 min). . . . .	71
<b>3.50</b>	Baseline $NO_3^-$ concentration variation with time (up to 60 mins). . . . .	72
<b>3.51</b>	Baseline $NO_3^-$ concentration variation with time (up to 14 days). . . . .	72
<b>4.1</b>	High standard for GC, FID. . . . .	75
<b>4.2</b>	High standard for GC, FID. . . . .	76
<b>4.3</b>	Low standard for GC, TCD. . . . .	77
<b>4.4</b>	Low standard for GC, TCD. . . . .	78
<b>4.5</b>	Typical chromatogram for methane experiment, FID. . . . .	79
<b>4.6</b>	Typical chromatogram for methane experiment, TCD. . . . .	80
<b>4.7</b>	Methane to hydrogen conversion data done with standard DBD reactor. . . . .	81
<b>4.8</b>	Standard reactor with changing lengths from end of flange. . . . .	81

<b>4.9</b>	Methane to hydrogen conversion data done with modified reactor with two electrodes. . . . .	82
<b>4.10</b>	Modified reactor with two electrodes each of width 1.5 inches. . . .	82

## LIST OF TABLES

<b>3.1</b>	A summary of the pH of distilled water before and after the addition of sodium bicarbonate. . . . .	47
<b>3.2</b>	A summary of the pH-calibrated Average $NO_2$ injection rates and breakeven times for various masses of dissolved sodium bicarbonate. . . . .	63
<b>4.1</b>	List of all gases and their low and high concentration for standard calibration. . . . .	74
<b>4.2</b>	List of gases and their residence time. . . . .	74



# Chapter 1

## INTRODUCTION

Low-temperature plasma physics and technology are diversify and multidisciplinary fields. The plasma parameters can span many orders of magnitude and applications are found in quite different areas of daily life and industrial production (see Fig. 1.7). This chapter will cover the current status of low-temperature plasma research as well as the goals and objective for this thesis. Specifically, the literature review is structured in four parts. The first part, provides an insight to plasma as the fourth state of matter. The second part, dives into the applications and technologies of low-temperature plasma. The third and fourth parts, contain a review on current water treatment and carbon reforming research as well as background on relevant research to this thesis. The last two section providing an outline for the specific goals and objectives of the current thesis and outline for the remainder of the thesis.

### 1.1 Description of Plasmas

Plasmas are commonly referred to as the fourth state of matter (Fig. 1.1) beyond solids, liquids and gases. In other words, providing energy to a solid transforms it into a liquid; providing additional energy to a liquid state creates a gaseous state and finally, providing energy to a gas leads to the creation of plasmas. While this energy can be provided in the form of heat (hypersonic flows involving reentry vehicles lead to plasma formation as a result of the very high temperature), a more efficient approach to creating laboratory plasmas is to provide this energy in the form of electrical energy. In spite of being the fourth state of matter with limited natural presence on earth, 99 % of our universe (including the sun) exists in the plasma state.

Plasmas, in a broad sense, can be classified into equilibrium and non-equilibrium plasmas with the distinction based on the value of electron temperature (mean electron energy) in comparison to the gas temperature. Specifically, equilibrium or thermal plasmas are plasmas in which the electrons are in equilibrium with the heavy particles (gas atoms, ions etc.) with most space plasmas belonging to this category. They are typically characterized by temperatures that are  $\sim 10,000$  K. On the other hand, non-equilibrium or non-thermal plasmas (the plasmas dealt with in this thesis) are characterized by electron temperatures that are significantly higher

than the heavy particles temperatures. Non-thermal plasmas are, therefore, characterized by electron temperatures that are  $\sim 10,000$  K and neutral gas temperatures that are only a few hundred K. The non-equilibrium is a direct consequence of the massive difference in masses between the electrons and heavy particles thereby leading to very inefficient elastic energy exchange during collisions.

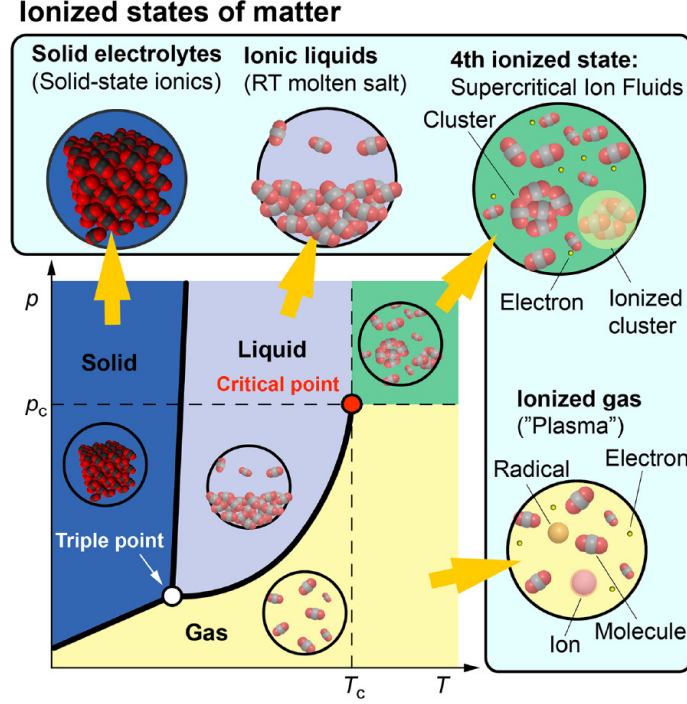


**Figure 1.1:** Schematic of a typical phase diagram and corresponding ionized states of matter. Reprinted from [1] with the permission of AIP Publishing.

Apart from electron temperature, another important parameter of plasmas is the plasma density (electron number density, Fig. 1.2). The number of electrons in conjunction with their energies completely determine the physical and chemical processes that can be initiated by the plasma. While the plasma state is often characterized by the electron temperature (or the mean electron energy), it is important to mention that the electrons in a typical plasma have an energy distribution that is a function of various operating parameters including pressure, characteristic length, and input energy to name a few. The electron energy distribution function (EEDF) under equilibrium conditions is given by

$$g_e(\epsilon) = \sqrt{\epsilon} e^{-\frac{\epsilon}{k T_e}} \quad (1.1)$$

and is referred to as the Maxwellian energy distribution. The electrons in a non-thermal plasma typically do not follow the Maxwellian EEDF. The deviation from a Maxwellian EEDF could either be in the form of a depleted high-energy tail or a replenished high-energy tail. With the EEDF completely quantifying the rate at which various reactions occur, the depleted or replenished tail will influence the reaction rates and hence the chemical processes that could possibly occur in the plasma. For example, one of the reactions in a simple argon plasma is the ionization reaction given by



which has a threshold energy of 15.76 eV (1 eV is  $1.602 \times 10^{-19}$  J). Therefore, only electrons which have an energy higher than this threshold will be able to participate in ionization. Similarly, as will be described in subsequent sections, there is a certain energy requirement associated with the dissociation of  $N_2$  or  $O_2$  (as required by the water treatment application) as well as  $CH_4$  (methane reforming application of current thesis). Plasmas are typically ignited by applying a sufficiently large

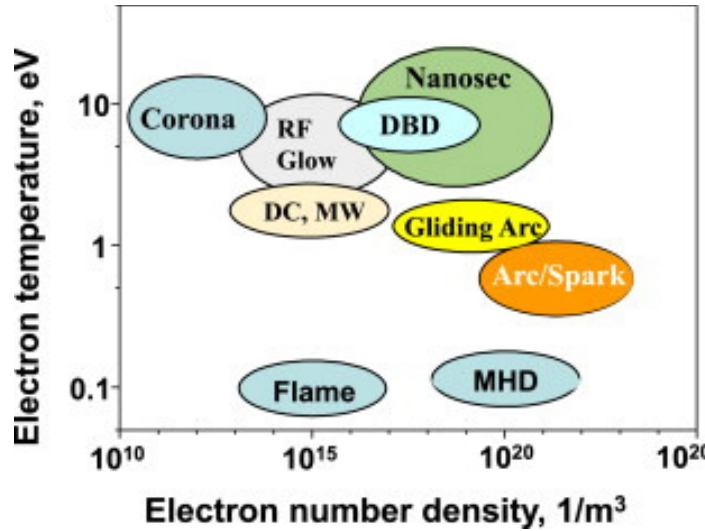


**Figure 1.2:** Schematic of electron temperature and number density for different discharges, Corona, direct current (DC) discharge, microwave (MW) discharge; dielectric barrier discharge (DBD), radio-frequency discharge (RF), glow discharge, gliding arc, nanosecond pulsed discharge (NSD), arc, magneto-hydrodynamic discharge (MHD), and flame. Reprinted from [2] with the permission of Elsevier.

voltage across two electrodes with the voltage requirement depending on various parameters including the operating gas, pressure, distance between electrodes and the electrode material/surface. The applied voltage can either be in the direct current

(DC) regime as well as the alternating current (AC) regime with fundamental differences in the physical mechanisms of ignition. DC plasmas are ignited by energizing ambient free electrons (typically existing at low number densities  $\sim 10^{10}$   $1/\text{m}^3$  even under ambient conditions) which, in turn, can lead to ionization of neutral gas atoms/molecules leading to the formation of ions and additional electrons. The newly created ions (assuming positively charged ions) will drift towards and eventually bombard the cathode leading to the emission of secondary electrons. The secondary electrons can now be energized in the electric field leading to the creation of additional electrons and this feedback process (gas phase ionization combined with secondary electron emission) eventually leads to an avalanche phenomenon leading to the ignition of the plasma with a large number of free electrons and ions. In spite of having free charged particles, it is worth emphasizing that the plasma is quasi-neutral (equally number of positive and negative charge) everywhere except in a small region near the two electrodes where the positive charged species exceeds the negative charged species. This positively charged region near the electrodes is called the plasma sheath.

While DC plasmas are ignited directly between two metallic electrodes, AC plasmas can be ignited between bare metallic electrodes or metallic electrodes covered with a layer of dielectric material. This is a direct consequence of the fact that direct current cannot flow dielectric materials whereas time-varying current can flow through dielectric material. Plasmas that are ignited using electrodes covered with dielectric material are referred to as dielectric barrier discharges (DBDs). Alternating current plasmas have been ignited at a wide range of excitation frequencies from a few kHz (as in the case of the current thesis) to as high as several GHz with a constant push toward the THz limit. One of the most popular applications of non-thermal plasmas is in the materials processing industry with semiconductor chips going through several plasma processing steps before becoming a part of state-of-the-art electronics including computers and smartphones. These plasmas are ignited using radio frequency excitation (MHz frequency) in reactors with a characteristic length  $\sim$  m at very low gas pressure ( $\sim$  100 mTorr). The product of pressure and characteristic length ( $pd$ ) is an important scaling parameter in determining the operating regime of plasmas. During the last two decades, there has been an active interest in igniting plasmas at atmospheric pressures including ambient air leading to the exciting area of microplasma science and engineering with several unique applications that exploit the physical and chemical properties of microplasmas. The  $pd$  scaling is directly responsible for the introduction of microplasmas operating at or near ambient pressures.

Both macroscale and microscale plasmas have several interesting operating regimes depending on the  $pd$  parameter and the applied voltage. While moderate  $pd$  plasmas operate in glow, abnormal glow and arc modes depending on the current flowing through the plasma, high  $pd$  plasmas operate in the streamer mode. In

simple terms, streamers can be looked at as a miniature form of lightning (one of the few natural plasmas observed from earth). The operation of a DBD is inherently connected to streamers propagating from one electrode to the other. The wide range of possible tuning parameters and operating conditions in non-thermal plasmas has led to their application in various fields with some of the more recent ones described in detail in the following section.

## 1.2 Emerging Applications of Non-Thermal Plasmas

Plasma applications range from medical to environment to aerospace to agriculture to material processing (mentioned in previous section) to assisted combustion and chemical conversion to name a few. In total there are nineteen sub-fields of plasma research [1, 3]. This section will cover applications that exploit plasma such as chemistry plasma medicine, plasma-assisted combustion, and plasma-assisted surface modifications.

### 1.2.1 Plasma Medicine

The use of plasma in the medical field is a rapidly developing new area of non-thermal plasma science and engineering [4, 5]. A key in plasma medicine is reactive oxygen and nitrogen species (RONS). RONS-based intercellular signaling research has become more helpful, in recent years, in establishing an explanation or the observed effects of plasma-generated RONS in living tissue [6, 7]. RONS in non-plasma therapies for wound healing, dermatology and cancer treatment has helped show the importance of RONS in plasma therapies. A wide variety of intercellular and intracellular processes are known to have RONS. Although plasma-liquid interaction (will be discussed further in the upcoming section) is not fully understood, plasma-liquid interaction is still a vital part of plasma medicine. Gas phase species generally interact with liquids, in biological interactions. The exact way chemical changes occur during plasma treatment of the cell culture medium [8] may not be completely understood at this time, but the results are undeniable (see Fig. 1.3) and have proven to have the potential to act therapeutically, Fig. 1.4. Plasma treatment has the versatility to treat cancer that has spread over relatively larger areas or is associated with sensitive organs, blood vessels, wound and skin decontamination, and burn wounds, to name a few [9]. Advances in using therapeutic pulsed electric fields appear to be related to plasma success in gene transfection, transdermal drug delivery and possibly to other effects. Typical electric fields magnitudes applied to tissue surfaces are known to be comparable with field strengths that are known to be biologically important [10]. One current research [11], reported that a significant increase in local blood flow and blood  $O_2$  content was induced by applying plasma jets to a mouse's skin. Similar results in human subjects were associated with plasma-induced generation of nitric oxide ( $NO$ ) [12]. The effects of these localized plasma treatments can possibly be transported to more distant regions because of

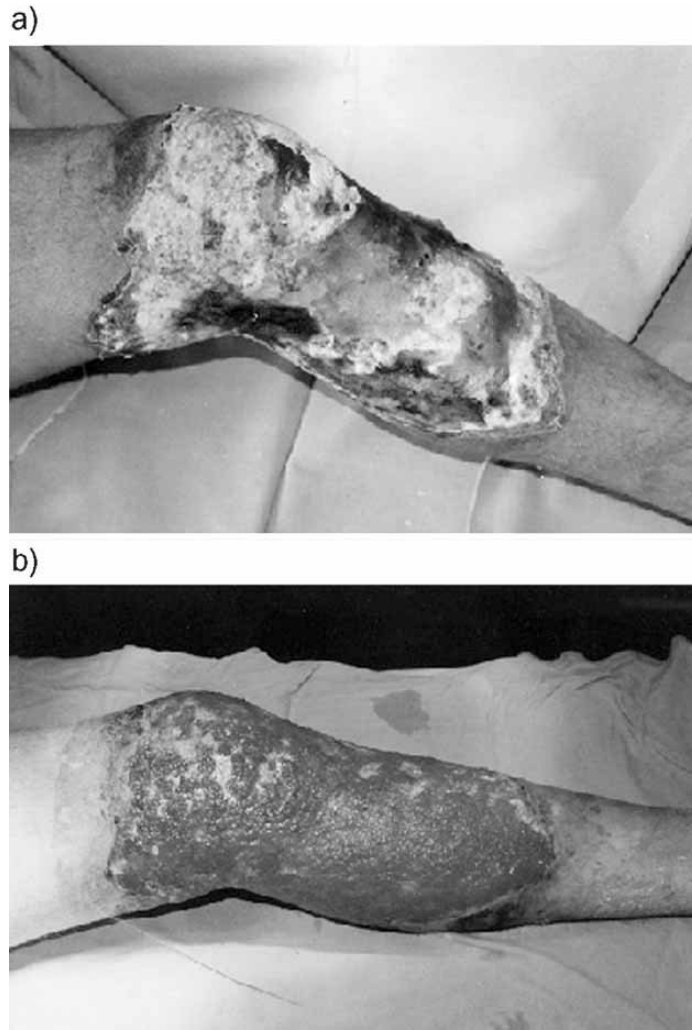


**Figure 1.3:** Dynamics of the healing of venous trophic ulcer during  $NO_2$  therapy. Reprinted from [5] with the permission of John Wiley and Sons.

blood flow. This possibility could change the view of plasma treatment as just a local effect. Non-thermal plasma applied to tumors has demonstrated induce immunogenic cell death, leading to activation of macrophages, generation of tumor specific antigens and associated cytokine release [13]. These exciting results have put more emphasis on developing plasma therapies that can controllably regulate immune responses with minimal side effects. Plasma treatment also has a place in dental and cosmetic applications. Periodontal infections (bacterial infection of the gums and bone) affect 23 % of over 65 year olds and over 75 % of pregnant women [15]. Periodontal infections increase the risk of heart diseases and other



**Figure 1.4:** Healing dynamics of the festered burn wound in process of  $NO_2$  therapy: a) prior to the beginning of treatment and b) after five sessions of  $NO_2$  therapy. Reprinted from [5] with the permission of John Wiley and Sons.

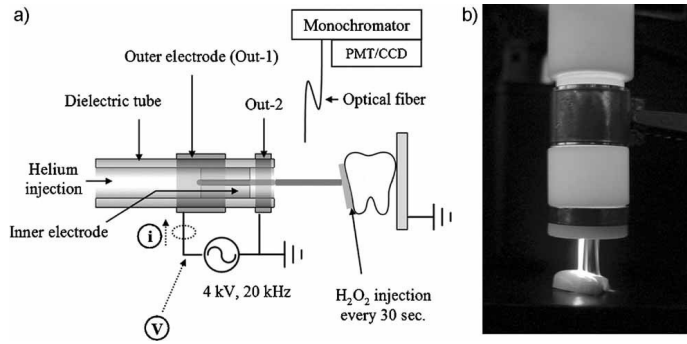


**Figure 1.5:** a) Configuration of the tooth bleaching experiment and b) schematic of the plasma jet and of the process. Reprinted from [14] with the permission of John Wiley and Sons.

medical complications (loss of teeth). Since plasma has the ability to penetrate into microscopic openings between tooth and gum, it would be an ideal candidate for preventive treatment on top of normal dental care. In addition, tooth bleaching (see Fig. 1.5) [14, 16] is another application that has been enhanced by the use of non-thermal plasma. Non-thermal plasma has a synergic effect on tooth bleaching by hydrogen peroxide ( $H_2O_2$ ) because it can generate (among many more species) hydroxyl radicals ( $OH$ ) that contribute significantly to tooth bleaching [17–20]. In cosmetics application, plasma treatment has been used to reconstruct tissue [21–24]

as well as skin rejuvenation (see Fig. 1.6) using nitrogen plasmas [25, 26].



**Figure 1.6:** a) Facial appearance before and b) 3 months after plasma skin regeneration, with improvement in pigmentation and skin texture. Reprinted from [5] with the permission of John Wiley and Sons.

### 1.2.2 Plasma-assisted Combustion

Today more than 80 % of the world's energy is converted by combustion. This has caused the need for alternative energy sources like solar energy and fuel cell technology. However, plasma can be used to improve/assist combustion. Plasma-assisted combustion is an encouraging technology to improve engine performance, increase lean burn flame stability, reduce emissions, and enhance low temperature fuel oxidation and processing [2]. Combustion has been playing a dominant role in air transportation, because of the high energy density of liquid fuels and the advantage of fast refueling. However, combustion in ground transportation still is very inefficient and the combustion of fossil fuels has been a major cause of climate change and air pollution [27–29].

New combustion engine technology such as the Homogeneous Charge Compression Ignition (HCCI) engines [30, 31], Partially Premixed Compression Ignition engines (PPCI) [32], and the Reactivity Controlled Compression Ignition (RCCI) engines [33] have been developed. These engines use a higher compression ratio and lower combustion temperature to increase engine efficiency and reduce emissions and heat losses. Although since these engines operate at high compression ratio and engine load, the drawbacks of not accurately controlling ignition timing and heat release rate may lead to unwanted excessive unburned hydrocarbon emissions or engine knock [34]. Therefore, there is a great need to develop an alternative method with rapid control of engine ignition. Air transportation has had similar



technologies in development to increase the fuel efficiency and meet the demanding emission standards: new lean burn aircraft combustor concepts such as the twin annular premixing swirled (TAPS) lean-burn burners [35, 36], lean direct injection (LDI) burners [37], trapped vortex combustion (TVC) lean burners [38], and pressure gain combustors [39]. The biggest challenges facing these new technologies are flame stability, ignition control, and complete combustion for scramjet engines at subsonic and supersonic propulsion.

Non-thermal plasmas such as microwave discharge [40], low frequency arc discharge [41], streamer high frequency (HF) discharge [42], surface discharge [43], and nanosecond pulsed discharge [44] have showed to enhance ignition, flame stabilization, and fuel/air mixing via chemical, thermal, and plasma induced aerodynamic effects in scramjet engines [45]. In addition, plasma discharge have showed to shorten the ignition delay time, and facilitate the transition from deflagration to detonation in pulsed detonation engines [46, 47]. Gas turbines have also benefited with increased flame stabilization (extended lower lean blowout limit and lean flammability limit) from the use of steady plasma jets [48], gliding arc [49], DC electric field [50], and HF streamer discharge [51] to name a few. Nanosecond pulsed discharge [52], microwave discharge [53], and radio frequency discharge [54], to name a few, have all demonstrated to enhanced ignition in internal combustion engines. Emission control [55] has been effectively reduced through the use of plasma jet [56], pulsed corona discharge [57], and dielectric barrier discharge [58]. Removal of  $SO_x$  [59], unburned hydrocarbons in flue gas [60], and soot formation in the exhausted gas of diesel engines [61] was all showed to be done by using plasma.

### 1.2.3 Plasma-assisted Surface Modification

The large number of species in a non-equilibrium plasma has made it possible for such plasmas to be used for the modification of surfaces of various kinds. In fact, materials processing was one of the first high-profile applications of laboratory plasmas with semiconductor manufacturers using it routinely even today. Fig. 1.7 shows a variety of examples of plasma material processing as well as other plasma technologies that touch daily life [62]. A typical semiconductor chip in today's computers and smartphones go through several plasma processing steps including plasma etching and plasma-enhanced chemical vapor deposition both of which are built on the foundations of plasma chemistry. For example, plasma immersion ion implantation was one of the techniques that revolutionized the process of doping and implantation [63, 64]. Similarly, plasma etching [65–70] and plasma-enhanced chemical vapor deposition [71–73] have been known since the 80s and are still widely used processes. There is a constant push towards controlled atomic layer etching [74, 75] and the physical and chemical properties of low-temperature plasmas play an important role in achieving the industry goals of shrinking semiconductor device dimensions and packing more and more transistors on a chip. Apart from



- |  |  |   |
|--|--|---|
| 01—Plasma TV                               | 09—Plasma-aided combustion                           | 16—Plasma-treated polymers                            |
| 02—Plasma-coated jet turbine blades        | 10—Plasma muffler                                    | 17—Plasma-treated textiles                            |
| 03—Plasma-manufactured LEDs in panel       | 11—Plasma ozone water purification                   | 18—Plasma-treated heart stent                         |
| 04—Diamondlike plasma CVD eyeglass coating | 12—Plasma-deposited LCD screen                       | 19—Plasma-deposited diffusion barriers for containers |
| 05—Plasma ion-implanted artificial hip     | 13—Plasma-deposited silicon for solar cells          | 20—Plasma-sputtered window glazing                    |
| 06—Plasma laser-cut cloth                  | 14—Plasma-processed microelectronics                 | 21—Compact fluorescent plasma lamp                    |
| 07—Plasma HID headlamps                    | 15—Plasma-sterilization in pharmaceutical production |   |
| 08—Plasma-produced $H_2$ in fuel cell      |  |   |

**Figure 1.7:** Plasma-coated jet turbine blade (02), Diamond like plasma CVD eyeglass coating (04), plasma-processing microelectronics (14), plasma-treated polymers (16), plasma-treated textiles (17), plasma-treated heart stent (18), and plasma-sputtered window glazing are various different examples of plasma material processing. NOTE: CVD, chemical vapor deposition; HID, high-intensity discharge; LED, light-emitting diode; LCD, liquid crystal display. Reprinted from [62] with the permission of National Academic Press

materials processing, plasmas have also been widely used for surface modification of various polymers [76–81] with the goal of making the polymer surface more hydrophilic [82] through the attachment of various functional groups. Plasmas have also been reported to trigger polymerization reactions [83, 84] on polymers apart from making the surface more resistant to bacteria [85–87]. These properties of plasma-treated polymers has resulted in their widespread use in treatment of polymers using bioengineering applications [88–90]. With the rapidly growing area of atmospheric pressure microplasmas, we are able to provide localized surface modifications as opposed to large-scale modifications using a low-pressure macroscale plasma.

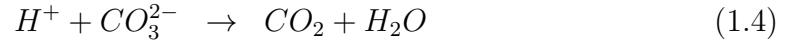
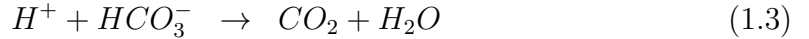
While the above paragraphs briefly discussed three rapidly growing areas that exploit plasma chemistry, the focus of this thesis will be on two environmental applications involving water and energy. The interaction of plasmas with liquids is also relevant to plasma medicine but the liquid that will be considered in the current thesis is water. There is already a great amount of interest in the interaction of plasmas with water as a result of applications in agriculture and water purification and the section below discusses prior work involving the interaction of non-thermal plasmas with water.

### 1.3 Plasmas in Water Treatment

Various technologies have been developed for water treatment, such as magnetic assistance [91], membrane technology [92], nanomaterials [93], and semiconductor photocatalysis [94], to name a few. Although the most conventional water treatment systems, usually employed in city’s water treatment plants, are essentially two processes filtration and disinfection [95]. The draw backs to these systems are the inability to breakdown toxic organic compounds such as volatile organic compounds and pharmaceuticals that may be also present in the water. Advanced oxidation processes (AOPs) [96–99] is one solution by introducing the same species that can be generated by non-equilibrium plasma. For this reason, non-equilibrium plasma is very valuable for water treatment.

The rapidly growing world population, with an estimated 11 billion in 2100 [100], has led to a great emphasis on food security and food production as two major problems that need to be tackled. This, in turn, has contributed to an increased importance of irrigation water management and the need to potentially grow crops in regions that do not have suitable soil or water resources. The acidity or alkalinity of the irrigation water [101] and soil is an important parameter that determines the suitability for agriculture. Specifically, pH measures the concentration of hydrogen ions in the water/soil and should be between 5.5 and 6.5 for most crops to ensure good irrigation water quality [102]. The soil and irrigation water pH play a crucial role in determining the outcomes of plant growth [103]. The alkalinity, determined by the concentration of bicarbonate and carbonate ions (and expressed in units of

ppm or mg/L or milliequivalents/L), should also be limited to ensure healthy crops. While the tolerable levels of alkalinity are specific to the crop and the container size, a general rule of thumb is to limit the bicarbonate levels to 120 mg/L and carbonate levels to 15 mg/L respectively. A common approach to decreasing the pH as well as alkalinity to tolerable limits is acidification [104] or the process of injecting acids into the irrigation water. The hydrogen ions in the acid will react with the bicarbonate/carbonate ions thereby producing carbon dioxide and water as given below



Candidate acids for lowering pH and alkalinity of irrigation water include sulphuric acid, nitric acid, and phosphoric acid with the specific choice depending on various factors including safety, cost, and potential side-effects to name a few. For example, nitric acid, inspite of possessing several advantages including addition of nitrate ( $NO_3^-$ ) ions that assist plant growth is seldom used because of difficulties associated with handling concentrated nitric acid. Magnetic treatment of irrigation water has also been considered as a candidate for soils with high soda content [105, 106]. In this context, the use of electrical discharges ignited by the application of high voltage in ambient air promises to be an attractive alternative for on-the-fly acid generation and pH/alkalinity reduction. In fact, nature presents an excellent example of a similar process wherein lightning strikes lead to nitrogen fixation and enhanced soil fertility (albeit in limited quantities because of their short duration). The electrical discharges considered in this work can be classified as low-temperature laboratory plasmas in contrast to fully-ionized plasmas that are encountered in space as well as nuclear fusion. Low-temperature plasmas exhibit significant degrees of non-equilibrium characterized by hot electrons and cold ions/neutrals and are often referred to as non-thermal plasmas. The hot electrons of plasmas ignited in ambient air have sufficient energy to break the nitrogen and oxygen bonds and triggering a whole host of reactions leading to the formation of  $NO_2$  among other species. The  $NO_2$  when dissolved in water leads to the formation of  $HNO_3$  which, in turn, can consume the bicarbonate ions. The application of non-equilibrium plasma in agriculture [107–109] has flourished in the last ten to twenty years. Specifically, non-equilibrium atmospheric-pressure plasma has been used for inactivation of microorganisms [110], decontamination [111], enhancement of seed germination and plant growth [112], DNA introduction [113], direct water disinfection and water softening using discharges in water [114, 115], wastewater treatment [116], and water purification [95, 117] to name a few. Plasma ignition has been pursued and demonstrated in the gas phase, in the liquid phase [118] as well as multiphase with plasma formation in either gas phase with dispersed droplets or

liquid phase with gas bubbles [119]. In spite of the large number of publications dealing with various aspects of plasma-liquid interaction [120], the interaction with alkaline water that contains dissolved bicarbonates/carbonates has not been considered before. A robust energy-efficient technology for decreasing alkalinity in surface water would greatly benefit irrigation water quality thereby ensuring ideal growth conditions for the crop. An on-demand technique using limited raw materials such as the one proposed here would also ensure that there is no need to handle or transport acids utilized for neutralizing. In this context, the enrichment of irrigation water through the use of atmospheric pressure electrical discharge is one of the focus of this thesis.

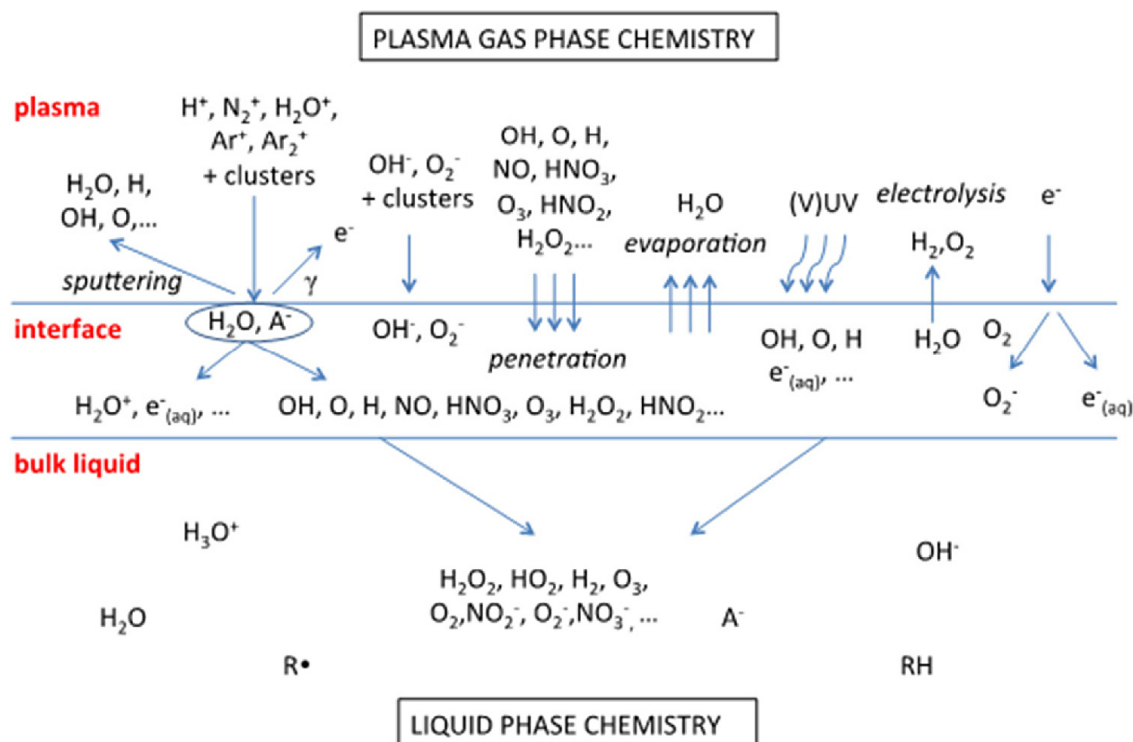
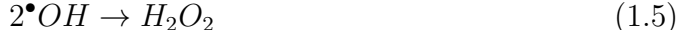


**Figure 1.8:** Schematic diagram of some of the most important species and mechanisms for an argon/humid air plasma in contact with water. Reprinted from [120] with the permission of IOP Publishing copyright 2014.

Plasma-liquid interaction (Fig. 1.8) is a complicated process that involves a large number of reactive species ( $O^\bullet$ ,  $OH^\bullet$ ,  $OH_2^\bullet$ ,  $N^\bullet$ ,  $O_3^\bullet$ ,  $N_2^\bullet$ ,  $N^\bullet$ ,  $OH^-$ ,  $O_2^-$ ,  $O^-$ ,  $O_2^+$ ,  $N_2^+$ ,  $N^+$ ,  $O^+$ ,  $H_2O_2$ ,  $e^-$  etc [121,122]) interaction with the liquid's (water in this work) surface and the bulk liquid. At the plasma-liquid interface a variety of results and methods are use to achieve a better understanding of the physics and

chemistry transport. These results and methods come from the interconnected fields of aerosol science and atmospheric chemistry [123,124], colloidal and interfacial surface chemistry [125], evaporation and condensation [126], and phase equilibrium and gas/liquid solubility [127]. The specific tools used to analyze the gas-liquid interface are classical transport theory [128], classical and non-equilibrium thermodynamics [129]. Monte Carlo and molecular dynamics are also used to analyze the gas-liquid interface [130]. Most if not all chemical reactions occur simultaneously in the bulk gas and liquid phases and interface with transport processes happening as well. A typical reactions that can occur in both phases and in the interface is the formation of hydrogen peroxide by hydroxyl radical recombination [120]:



The process by which the recombinations occurs in the gas, liquid, and interface is:



where the interface reaction is pursued by the injection of the hydrogen peroxide into the liquid:

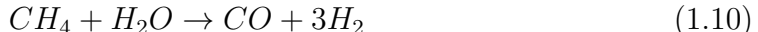


The reaction rates in the bulk gas and liquid phase are the key in modeling of reaction mechanisms. Reactions occurring at the gas phase usually involve collisions between two species. This causes determining rate coefficients in the gas phases by using gas kinetic theory, molecular dynamics, and/or quantum chemical methods. On the other hand, determining the bulk liquid phase's rate coefficients is not as simple. The reactions in the bulk liquid are constantly being impacted by the liquid itself. Because of this there is no unified approach to theoretically derive the reaction rate coefficients in liquids [131]. In addition, non-equilibrium reactants that enter the liquid from the plasma reactions can be dominated. For this reason, rate coefficients in the bulk liquid are found by a non-equilibrium, rate coefficient based analysis. Textbooks [4,132,133], journal articles [134–137], and online data bases are the dominate source for reaction rate coefficients in the bulk liquid. Modeling and simulations of the plasma-liquid interaction [138–145] has increased since the invested interest in plasma medicine, water treatment and plasma-assisted carbon reforming.

#### 1.4 Plasmas in Carbon Reforming

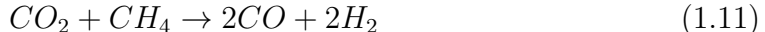
With the growing importance of clean energy technologies in today's world, alternatives to fossil fuel based energy production is actively pursued. Among many

options including solar and wind, fuel cells remain an equally attractive option wherein hydrogen reacts with oxygen to produce a clean product in water. However, hydrogen is seldom available in its natural form thereby requiring an efficient process that can produce hydrogen from other raw materials. One of the most widely used techniques (as of today) to produce hydrogen is the reforming of greenhouse gases such as methane in the presence of steam [146,147] and a catalyst such as Nickel [148–150]. The steam reforming of methane accounts for about 95 % [151,152] of the hydrogen produced and proceeds through the reaction



However, this process occurs at a temperature of about 1200 K and requires this heat to be produced typically from fossil fuel burning. As in the case of most temperature-induced processes, the efficiency of this process is about 70 % [153]. The generation of heat through fossil fuel burning and the subsequent production of clean fuel may reduce the real impact of the clean fuel since the steps involved in its production utilize fossil fuels leading to greenhouse gas emission.

An alternative to this process stems from the possibility of utilizing low-temperature non-thermal plasmas with high energy electrons to trigger the conversion of methane to carbon monoxide and hydrogen [154–156]. More specifically, one could envision a process where two potent greenhouse gases in methane and carbon dioxide react with each other with assistance from the plasma to produce carbon monoxide and hydrogen. The plasma-assisted reaction between methane and carbon dioxide is given by



The mixture of carbon dioxide and methane is a biogas. Biogas is a type of biofuel that is naturally produced from the decomposition of organic waste. When organic waste (animal manure, food scraps, wastewater, and sewage, etc) decomposes in environment absent of oxygen the outcome is the release of a blend of gas that is mainly composed of methane and carbon dioxide. Biogas is an available in California, China, and India, to name a few place. As mention above the use of plasma can be used to converted biogas to a clean fuel (carbon monoxide and hydrogen).

Microwave (MW) plasma [157–159], gliding arc (GA) discharge [160–162], and DBD [163–165] have all been used for the conversion of biogas. Much research has been applied to improving the energy efficiency of the conversion, as well as the selectivity towards value-added chemicals, in combination with catalysis. GA discharge has had energy efficiency of the conversion reported to be 43 % [166–168]. MW plasmas have had energy efficiency conversion of up to 90 % [169–171]. The energy efficiency of a DBD is more limited (typically up to 10 %), [172] but can be improved by inserting packing inside the plasma [173] and the latter also allows the

integration of a catalyst, for the selective production of value-added chemicals. In the view of dry methane reforming, this is the second focus (the first being plasma-assisted irrigation water enrichment) of the current thesis. The next section will cover specific goals and objectives for this thesis.

### 1.5 Research Goals and Objectives

The overarching goal for the water treatment project is to study the interaction of an atmospheric pressure electrical discharge set-up with varying concentrations of sodium bicarbonate dissolved in distilled water. Apart from decreasing the alkalinity by reacting with bicarbonate, the  $HNO_3$  produced due to plasma treatment also assists in increasing the nitrate concentration thereby leading to an enrichment of the irrigation water. In order to achieve this goal the following are specific objectives that will drive the research:

- Design and build DBD reactor for the use of water treatment.
- Measuring pH and nitrate concentration as a function of plasma treatment time.
- The formulation of a system-level model that describes the treatment process.

In the context of reforming methane and carbon dioxide to carbon monoxide and hydrogen, the primary goal of this project is to demonstrate the use and study of plasma-assisted dry methane reforming. The specific objectives to accomplished this goal are:

- Design and build DBD reactor for the use of reforming carbon dioxide and methane to carbon monoxide and hydrogen (clean gas).
- Present primarily data for the conversion of methane to hydrogen.

### 1.6 Outline of Thesis

The remainder of the thesis is outlined as follows. Chapter 2 presents the experimental set-up of the DBD reactor used for water treatment of alkaline water, the formulation of a system-level model that describes the treatment process, and the experimental set-up of the DBD reactor used for converting methane and carbon dioxide to carbon monoxide and hydrogen. Chapter 3 covers the process of selecting the DBD reactor for water treatment as well as presenting the result for decreasing pH and increasing nitrate concentration of bicarbonate water. Chapter 4 present the primary data for converting methane to hydrogen through the use of non-equilibrium atmospheric pressure plasma reactor. Chapter 5 is reserved for summarizing the conclusions and future recommendation.



## Chapter 2

# EXPERIMENTAL SET-UP AND COMPUTATIONAL ANALYSIS

In this chapter, the experimental set-up of the water treatment project, the carbon reforming project will be explained as well as computational analysis for the water treatment project. The water treatment experimental set-up went through various stages of development until the needle design was settled on. The different stages of water treatment experimental set-up will be elaborated on in chapter 3. The carbon reforming experimental set-up did not go through as many changes but instead was inspired by the plasma reactor of Dr. Annemie Bogaerts's group at University of Antwerp. The computational analysis started with predicting the pH of sodium bicarbonate-distilled water reaction. Then the plasma was introduced to the sodium bicarbonate-distilled water mixture as if it was an acid, specifically nitric acid. The next stage of progression was to treat the plasma as nitrogen dioxide.

### 2.1 Experimental Set-up for Water Treatment

The DBD design went through many changes until we settled with the needle design (Fig. 2.1). As can be seen in Fig. 2.1, the DBD is made up of stainless steel tube of dimensions 3 mm outer diameter, 0.5 mm wall thickness, and 49 cm length. The quartz tube and rubber stoppers are used for stability for the stainless steel tube. A 90 degree elbow connections is used to connect the 1/8 inch plastic tubing to the stainless steel tubing. The plastic tubing is connected to the Brooks Instrument Flow Meter via compression fittings. From the Brooks Instrument Flow Meter the plastic tubing is connected to Praxair 3012 High Purity Regulators via compression fittings. The maximum pressure of the regulator is 50 psi. The power supply used (Fig. 2.2) is PVM500 Plasma Power Generator for Conventional and Complex Loads. The ranges of voltages, frequencies and power are 1-40 kV, 20-70 kHz, and 10-300 W respectively. The power supply is propped up by a 13 in by 24 in by 6.5 in wooden box. The wooden box was built so that the power connection could reach the stainless steel and copper sheet comfortably. The copper sheet was warper around the 250 mL beaker and held together with electric tape. During the experiments, the power electrode and ground were switched between the stainless steel tubing and copper sheet depending on the experiments. The copper sheet was

lined up with the surface of the distilled water in the beaker so that measuring the distance between electrodes was simple. The distance between electrodes was measured from the end of the stainless steel tube to the surface of the distilled water. The distances used were 1 mm, 14 mm, and 29 mm. A detail schematic of the entire water treatment system can be seen in Fig. 2.7.



**Figure 2.1:** Needle design.



**Figure 2.2:** Entire system.

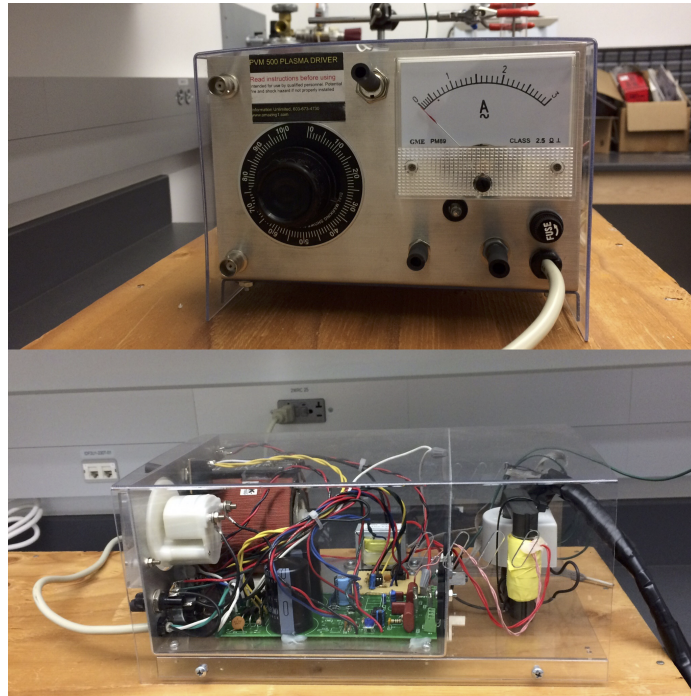


**Figure 2.3:** PVM500 Plasma Power Generator for Conventional and Complex Loads.

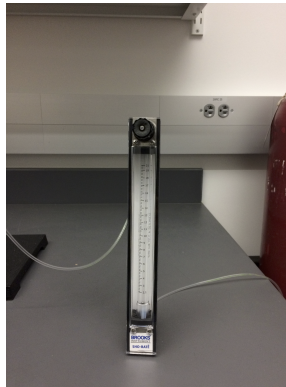


**Figure 2.4:** Brooks Instrument Flow Meter

## 2.2 Computational Analysis

The plasma model was based on a common chemistry problem and from there the set of equations were modified for our purposes. This section will go over



**Figure 2.5:** 90 degree elbow connection with compression fittings.



**Figure 2.6:** 1/8 inch compression fittings.

the sodium bicarbonate-distilled water reaction and show the progression of the modification until our final model was reached. Firstly, dealing with the reaction of adding sodium bicarbonate to the distilled water and predicting the new pH was our goal. Assuming sodium bicarbonate dissolves completely,



which is a safe assumption and benefits with not having to worry about an equilibrium. Once free in solution,  $HCO_3^-$  can act as both an acid giving an a proton and a base becoming neutral carbonic acid,



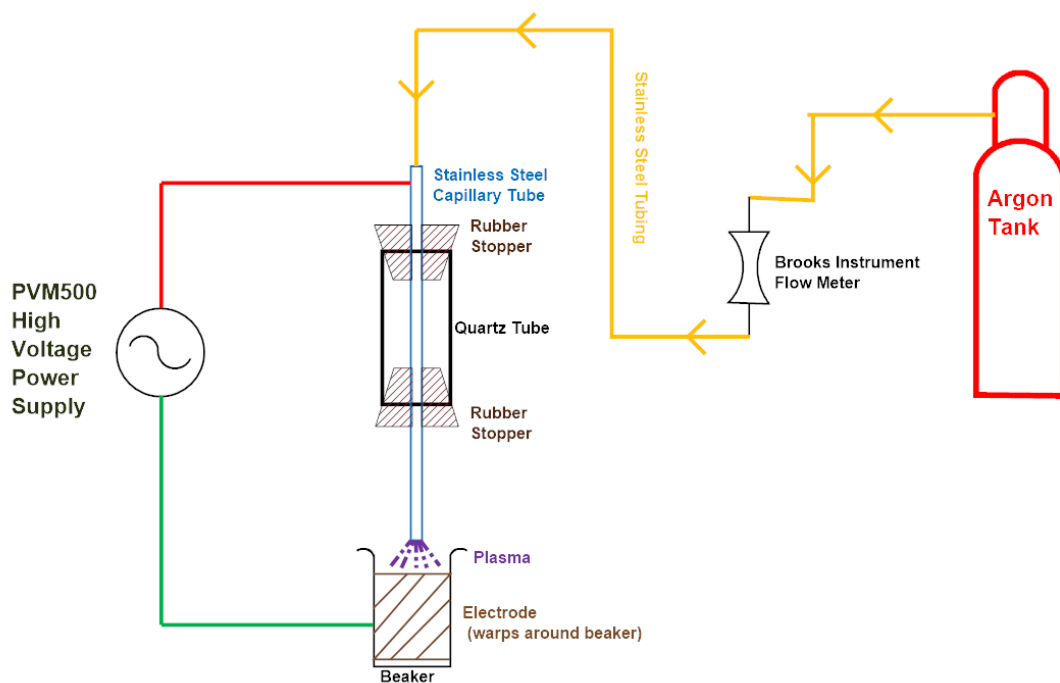


**Figure 2.7:** Schematic of the entire water treatment system.

The hydrogen carbonate ion ( $HCO_3^-$ ) ability to act as an acid and base is called amphiprotic. Carbonic acid can also form carbon dioxide dissolved in water. Carbon dioxide can exchange with the gas phase, entering and leaving the air,



There is finally the ubiquitous autoionization of water,



Now that all the chemical reactions are accounted for the next step is writing

the relevant equilibrium expressions that apply to each of the chemical reactions:

$$\frac{[HCO_3^-][H^+]}{[H_2CO_3]} = K_{a1} \quad (2.7)$$

$$\frac{[CO_3^{2-}]}{[H^+]} = K_{a2} \quad (2.8)$$

$$[H^+][OH^-] = K_w \quad (2.9)$$

$$\frac{[H_2CO_3]}{[CO_2]} = K_{hydration} \quad (2.10)$$

$$\frac{[CO_2]}{P_{CO_2}} = K_{solvation} \quad (2.11)$$

Currently, we have seven unknowns:  $[H_2CO_3]$ ,  $[HCO_3^-]$ ,  $[CO_3^{2-}]$ ,  $[H^+]$ ,  $[OH^-]$ ,  $[CO_2]$ , and  $P_{CO_2}$ . The system is currently under-specified and unsolvable with only five equations to the seven unknowns. Introducing a charge balance and finding a solutions for  $P_{CO_2}$  would do the job. The partial pressure of carbon dioxide,  $P_{CO_2}$ , in the air is not a rigorous constant because the amount of water vapor in the air exhaled and the other factors can change it. Although, terrestrial dry air is composed of about 0.039 % mol of  $CO_2$  and indoor air is typically about 1 % mol of  $H_2O$ . The ambient pressure is about 1.0 bar and using the Dalton's Law, the partial pressure of carbon dioxide,  $P_{CO_2}$  is:

$$\begin{aligned} p_{total} &= p_1 + p_2 + p_3 + \dots + p_n \\ P_{CO_2} &= 0.00039 \times 0.99 \times 1.0 \\ P_{CO_2} &= 0.000386 \text{ bar} \end{aligned} \quad (2.12)$$

Now that  $P_{CO_2}$  is removed as an unknowns, dropping the count to six, its time to introduce a charge balance equations to bring the number of equations to six and making the problem solvable:

$$[HCO_3^-] + 2[CO_3^{2-}] + [OH^-] = [H^+] + [Na^+] \quad (2.13)$$

A new unknown,  $[Na^+]$ , is introduced but a trivial mass balance on sodium converts it into a known. The only source of  $[Na^+]$  for this system is the  $NaHCO_3$ ,

$$[Na^+] = F_{NaHCO_3} \quad (2.14)$$

Now that there are six equations and six unknowns the problem is solvable

in principle. Although, there is a issue with one of the equations,



which makes the assumptions that the chemical reaction happens very fast. In all actuality, the chemical reactions is very slow and will not reach equilibrium on the timescale of the experiment. Since, we want to know the pH as soon as the solution is made we have to assume that Eq. 2.15 does not happen on the timescale of the experiment. To make up for the loss of an equations, a mass balance on carbon will have to be done,

$$Total\ carbon = [H_2CO_3] + [HCO_3] + [CO_3^{2-}] + [CO_2] \quad (2.16)$$

with the atmosphere removed from consideration as a source or sink for carbon (as mention above that carbon dioxide exchanges with the gas phase happens very slowly), all the carbon atoms available to the system come from the  $F_{NaHCO_3}$ . Thus,

$$F_{NaHCO_3} = [H_2CO_3] + [HCO_3] + [CO_3^{2-}] + [CO_2] \quad (2.17)$$

Finally, there are six equations and six unknowns making the problem fully-specified system. Even though, we have a fully-specified system there is one more wrinkle that will simplify the system to five unknowns and five equations. The wrinkle is treating  $CO_{2(aq)}$  and  $H_2CO_{3(aq)}$  as one species, effectively combining the reactions,

$$\begin{aligned} H_2CO_3 &\rightleftharpoons HCO_3^- + H^+ \\ &\text{and} \\ CO_{2(aq)} + H_2O_{(l)} &\rightleftharpoons H_2CO_{3(aq)} \\ &\text{into} \\ CO_{2(aq)or}H_2CO_3 &\rightleftharpoons HCO_3^- + H^+ \\ &\text{where} \\ K_{a1} &= \frac{[HCO_3^-][H^+]}{[H_2CO_3] + [CO_2]} = \frac{[HCO_3^-][H^+]}{[H_2CO_3 + CO_2]} = \frac{[HCO_3^-][H^+]}{[\"H_2CO_3\"]}. \end{aligned} \quad (2.18)$$

The reaction (Eq. 2.18) is kinetically very fast, and once  $CO_2$  is dissolved in water it can rapidly interconvert between carbonic acid and "free" dissolved  $CO_2$ . At any moment, only about 0.2 % of the  $CO_2$  is bound to water as  $H_2CO_3$ , but if some of that is somehow removed, more will quickly form via Eq. 2.18. Another key is that Eq. 2.18 involves water, which is in ample supply and its concentration

is effectively fixed. Considering these two points, it is possible to further simplify this system to treat  $CO_{2(aq)}$  and  $H_2CO_{3(aq)}$  as one and the same, provided we use  $K_{a1} = 4.46 \times 10^{-7}$ . Now the chemical expressions are:



where the equilibrium equation associated with the above chemical expressions are,

$$K_{a1} = 4.46 \times 10^{-7} = \frac{[HCO_3^-][H^+]}{[^{\prime\prime}H_2CO_3^{\prime\prime}]} \quad (2.22)$$

$$K_{a2} = 4.69 \times 10^{-11} = \frac{[CO_3^{2-}]}{[H^+]} \quad (2.23)$$

$$(2.24)$$

The equilibrium equation associated for the autoionization of water is given by

$$K_w = [H^+][OH^-] \quad (2.25)$$

While the nominal value of  $K_w = 10^{-14}$ , this work used  $K_w = 10^{-2p_{H,initial}}$  where  $p_{H,initial}$  is the initial pH of the distilled water without dissolved  $NaHCO_3$  and plasma treatment. The charge balance is,

$$[HCO_3^-] + 2[CO_3^{2-}] + [OH^-] = [H^+] + F_{NaHCO_3} \quad (2.26)$$

$$(2.27)$$

The mass balance on carbon is,

$$F_{NaHCO_3} = [H_2CO_3] + [HCO_3^-] + [CO_3^{2-}] + [CO_2] \quad (2.28)$$

Now with the equilibrium equations, charge balance, and mass balance solving the system is needed. Starting the the mass balance on carbon (Eq. 2.28), plugging in the Eq. 2.22 and solving for  $[HCO_3^-]$  we get:

$$[HCO_3^-] = F_{NaHCO_3} \left( \frac{1}{\frac{[H^+]}{K_{a1}} + 1 + \frac{K_{a2}}{[H^+]}} \right) \quad (2.29)$$

Simplify the above expression by factoring  $\frac{1}{K_{a1}[H^+]}$  from the denominator and



Eq. 2.29 becomes:

$$[HCO_3^-] = F_{NaHCO_3} \left( \frac{K_{a1}[H^+]}{[H^+]^2 + K_{a1}[H^+] + K_{a1}K_{a2}} \right) \quad (2.30)$$

Using Eq. 2.22 to plug into the the charge balance:

$$[HCO_3^-] + 2 \left( \frac{K_{a2}[HCO_3^-]}{[H^+]} \right) + [OH^-] = [H^+] + F_{NaHCO_3} \quad (2.31)$$

Factoring out  $[HCO_3^-]$  and plugging in Eq. 2.31:

$$F_{NaHCO_3} \left( \frac{K_{a1}[H^+]}{[H^+]^2 + K_{a1}[H^+] + K_{a1}K_{a2}} \right) \left( 1 + \frac{2K_{a1}}{[H^+]} \right) + [OH^-] = [H^+] + F_{NaHCO_3} \quad (2.32)$$

Now plugging in Eq. 2.25 into Eq. 2.32:

$$F_{NaHCO_3} \left( \frac{K_{a1}[H^+]}{[H^+]^2 + K_{a1}[H^+] + K_{a1}K_{a2}} \right) \left( 1 + \frac{2K_{a1}}{[H^+]} \right) + \frac{K_w}{[H^+]} = [H^+] + F_{NaHCO_3} \quad (2.33)$$

Multiplying Eq. 2.33 by  $[H^+]$  and moving everything to the right side:

$$F_{NaHCO_3} \left( \frac{K_{a1}[H^+]^2}{[H^+]^2 + K_{a1}[H^+] + K_{a1}K_{a2}} \right) \left( 1 + \frac{2K_{a1}}{[H^+]} \right) - F_{NaHCO_3}[H^+] + K_w - [H^+]^2 = 0 \quad (2.34)$$

Factoring out  $F_{NaHCO_3}$  and multiplying by -1, the final form is:

$$[H^+]^2 - F_{NaHCO_3} \left[ \left( \frac{K_{a1}[H^+]^2}{[H^+]^2 + K_{a1}[H^+] + K_{a1}K_{a2}} \right) \left( 1 + \frac{2K_{a1}}{[H^+]} \right) - [H^+] \right] - K_w = 0 \quad (2.35)$$

Using Matlab's `fsolve()` function to solve Eq. 2.35 will find the  $[H^+]$ . Knowing  $[H^+]$  then solving for the pH of  $NaHCO_3$ -water mixture is simple:

$$pH = \log_{10}([H^+]) \quad (2.36)$$

The next progression to the plasma model was to consider mixing  $NaHCO_3$  solution with plasma treated water. One of the many reactions that happens in the interaction with the low temperature plasma and water is the creation of  $NO_3^-$  which causes the pH of water to decrease. With the free flowing hydrogen ions

and nitrate in the water, nitric acid ( $HNO_3$ ) can be created. After treating the water for 22 minutes with plasma and decreasing the pH to between 3 and 4 our assumption was to consider the "plasma water" as  $HNO_3$ . Mixing  $HNO_3$  solution and  $NaHCO_3$  solution is very similar to the previous analysis of adding  $NaHCO_3$  to water. Most of the equations will remain the same with slight changes to the mass balance on carbon and the charge balance. The changes come with considering the two volumes of each solution and the negative charge of  $[NO_3^-]$ .

$$\frac{F_{NaHCO_3}V_b}{V_a + V_b} = [H_2CO_3] + [HCO_3^-] + [CO_3^{2-}] + [CO_2] \quad (2.37)$$

$$[HCO_3^-] + 2[CO_3^{2-}] + [OH^-] + [NO_3^-] = [H^+] + \frac{F_{NaHCO_3}V_b}{V_a + V_b} \quad (2.38)$$

With  $V_a$  and  $V_b$  being the volumes of the  $HNO_3$  solution and  $NaHCO_3$  water solution. Taking the new mass balance and charge balance equations, Eq. 2.30 becomes

$$[HCO_3^-] = \frac{F_{NaHCO_3}V_b}{V_a + V_b} \left( \frac{K_{a1}[H^+]}{[H^+]^2 + K_{a1}[H^+] + K_{a1}K_{a2}} \right) \quad (2.39)$$

Using Eq. 2.39 and plugging into Eq. 2.38 with similar analysis as Eq. 2.31 through Eq. 2.35 results in:

$$[H^+]^2 - \frac{F_{NaHCO_3}V_b}{V_a + V_b} \left[ \left( \frac{K_{a1}[H^+]^2}{[H^+]^2 + K_{a1}[H^+] + K_{a1}K_{a2}} \right) \left( 1 + \frac{2K_{a1}}{[H^+]} \right) - [H^+] \right] - K_w - [NO_3^-][H^+] = 0 \quad (2.40)$$

The last detail to deal with is  $[NO_3^-]$ ,

$$[NO_3^-] = \frac{C_{HNO_3}V_b}{V_a + V_b} \quad (2.41)$$

Plugging in Eq. 2.41 into Eq. 2.40 provides the final form to be solve with Matlab's `fsolve()` function:

$$[H^+]^2 - \frac{F_{NaHCO_3}V_b}{V_a + V_b} \left[ \left( \frac{K_{a1}[H^+]^2}{[H^+]^2 + K_{a1}[H^+] + K_{a1}K_{a2}} \right) \left( 1 + \frac{2K_{a1}}{[H^+]} \right) - [H^+] \right] - K_w - \frac{C_{HNO_3}V_b}{V_a + V_b}[H^+] = 0 \quad (2.42)$$

The solution to Eq. 2.42 and the use of Eq. 2.36 would provide with the pH of the  $NaHCO_3$  solution and  $HNO_3$  solution mixture.

The last progression step to the final model form is considering the plasma as  $NO_2$  being injected into the water sample. This assumption was made so that  $HNO_3$  could be introduced via the interaction of  $NO_2$  and  $H_2O$ . In addition,  $NO_2$  is a by product of the plasma interacting with the air so representing the plasma as  $NO_2$  is possible. This can be seen in the chemical reaction of:



Eq. 2.43 is assumed to happen very fast so no consideration of equilibrium reaction is necessary. In this new situation, the equilibrium equations as before with the past two analysis stay the same. The mass balance on carbon is the same as in Eq. 2.28 from finding the pH of  $NaHCO_3$  and distilled water mixture. The charge balance will take into account the negative charge of  $NO_3^-$  but there will be no consideration of different volumes. Therefore, the final system of equations will be:

$$K_{a1} = \frac{[HCO_3^-][H^+]}{[H_2CO_3]} \quad (2.44)$$

$$K_{a2} = \frac{[CO_3^{2-}]}{[HCO_3^-][H^+]} \quad (2.45)$$

$$K_w = [H^+][OH^-] \quad (2.46)$$

$$F_{NaHCO_3} = [H_2CO_3] + [HCO_3^-] + [CO_3^{2-}] + [CO_2] \quad (2.47)$$

$$[HCO_3^-] + 2[CO_3^{2-}] + [OH^-] + [NO_3^-] = [H^+] + F_{NaHCO_3} \quad (2.48)$$

Using Eq. 2.45, plugging into the new charge balance, and solving for  $[HCO_3^-]$  will result in,

$$[HCO_3^-] = F_{NaHCO_3} \left( \frac{K_{a1}[H^+]}{[H^+]^2 + K_{a1}[H^+] + K_{a1}K_{a2}} \right) \quad (2.49)$$

Now as before using Eq. 2.49 and the same analysis as Eq. 2.31 through Eq. 2.35 will result in,

$$[H^+]^2 - F_{NaHCO_3} \left[ \left( \frac{K_{a1}[H^+]^2}{[H^+]^2 + K_{a1}[H^+] + K_{a1}K_{a2}} \right) \left( 1 + \frac{2K_{a1}}{[H^+]} \right) - [H^+] \right] - K_w - [NO_3^-][H^+] = 0 \quad (2.50)$$

The model considers  $[NO_3^-]$  as input so everything in Eq. 2.50 is known except for  $[H^+]$ . Similar as before the solution of Eq. 2.50 and Eq. 2.36 will provide the pH of the plasma treated water.

### 2.3 Experimental Set-up for Carbon Reforming

This carbon reforming system is made of two distinct parts: the plasma reactor and the Gas Chromatograph (GC) 2014 (Fig. 2.10). The GC-2014 does all the analysis work of the the ionized methane or carbon dioxide or mixture of both. The GC-2014 has Flame Ionization Detector (FID) and Thermal Conductivity Detector (TCD). The FID detects carbon base molecules: methane, carbon dioxide, carbon monoxide, ethane, and ethylene. The TCD detects hydrogen, oxygen, and nitrogen. The plasma reactor (Fig. 2.13) is made up of a quartz tube connected to two custom stainless steel end connections. The top connection has two 1/8 inch compression fittings (Fig. 2.6). The bottom end connection has one 1/8 inch compression fittings. The design of the end connections can be seen in Fig. 2.11 and Fig. 2.12. The plasma reactor is a standard DBD reactor (more so than the reactor for the water treatment experiments) with a inner copper rod and outer copper sheet. The dimensions of the rod are 1/8 inch diameter and 12 inch in length. Two different copper sheets sizes were used as the outer electrodes; both were 8 inch in length and the widths were 1.5 inch and 3 inch. Individual Sierra Smarttrak 100 series Mass Flow Controller were used for methane and carbon dioxide, as seen in Fig. 2.14. The mass flow controllers were each rated to controller flows of up to 1.0 slm with three decimals of precision. The connections of the mass flow controllers were compression fittings.

There were three different type of filters used: hydrogen, methane, and moisture filter. The hydrogen and methane filters can be seen in Fig. 2.15. Moisture filter can be seen in Fig. 2.16. A detail schematic of the entire carbon reforming system can be seen in Fig. 2.8. Hydrogen, argon, and air gases were used for the GC-2014. Hydrogen and air were used for FID and TID specifically whereas argon was used as a background gas. The regulator used for hydrogen and argon was 3012 High Purity Dual Stage Nickel-Pated Brass Barstock Body, Four-port Configuration, 316 Stainless Steel Diaphragm. The air was supplied by the in-laboratory supply. The regulators used for methane and carbon dioxide were 4012 Critical Purity Dual Stage Brass Barstock, Six-port Configuration, 316 Stainless Steel Diaphragm regulator and 3008 Specialty Purpose Single Stage Chrome-Plated Brass Barstock Body, 316L Stainless Steel Diaphragm, Electrically Heated regulator, respectively. All regulators max pressure was 250 psi. All outlet connections for each regulator was 1/8 inch compression tube fittings (Fig. 2.5). The max pressure of the air supply was 100 psi. All the tubing was 1/8 inch stainless steel. The type of gas tanks used were methane 5.0, research 99.999 % T cylinder, carbon dioxide Laser Star, 5.0 99.999 % K cylinder, argon 4.8, 99.999 % K cylinder, and hydrogen 5.0, 99.999 % UHP K cylinder. Before going into how everything is connected, its worth noting that all the tubing was 1/8 inch stainless steel.

The hydrogen regulator is connected to the hydrogen filter. The hydrogen filter then connects to the GC-2014. The argon regulator was directly connected to

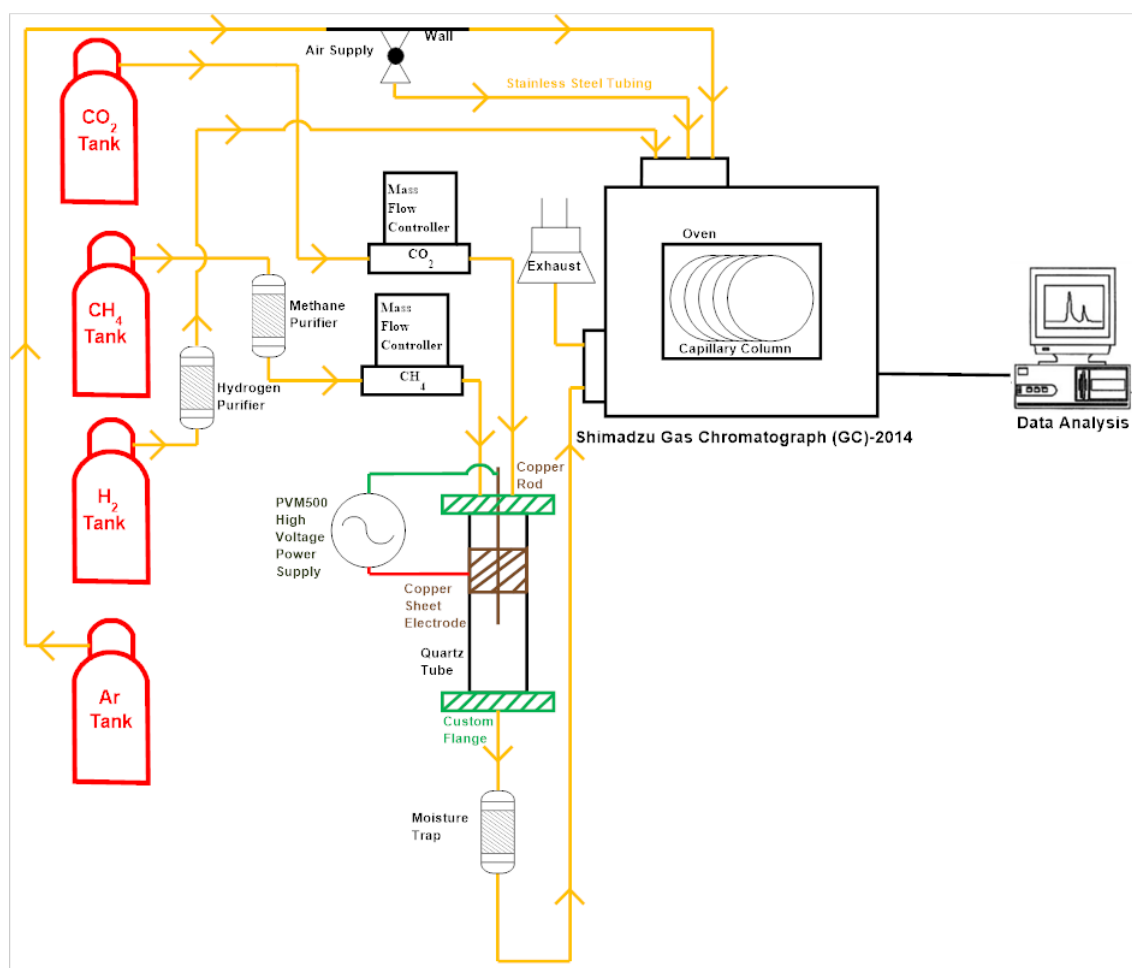


**Figure 2.8:** Schematic of the entire carbon reforming system.

the GC-2014 as well as the air. The methane gas flowed through the regulator into the methane purifier then into the mass flow controller then flowing to the plasma reactor. The carbon dioxide flowed through the regulator directly into the mass flow controller then flowing to the plasma reactor. The power supply was connected to the copper sheet warped around the quartz tube (power electrode) and the inner copper rode (ground electrode). After the methane and carbon dioxide are ionized, the gases flow out of the reactor into the moisture filter. The moisture filter was added to the system to compensate for any water produced by the process of carbon reforming. Once the ionized gases flow out of the moisture trap, they flow directly into the GC-2014. A 1 mL sample is taken by the GC-2014 to be analyzed. The rest of the gas is flow out of the GC-2014 and into the exhaust. The GC-2014 analysis takes fourteen minutes.



**Figure 2.9:** Carbon reforming system



**Figure 2.10:** Gas Chromatograph (GC) 2014

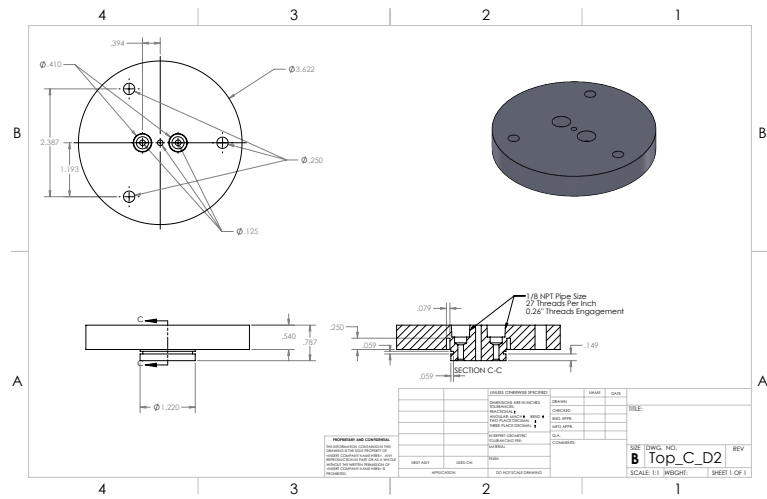


**Figure 2.11:** The top end connection design.

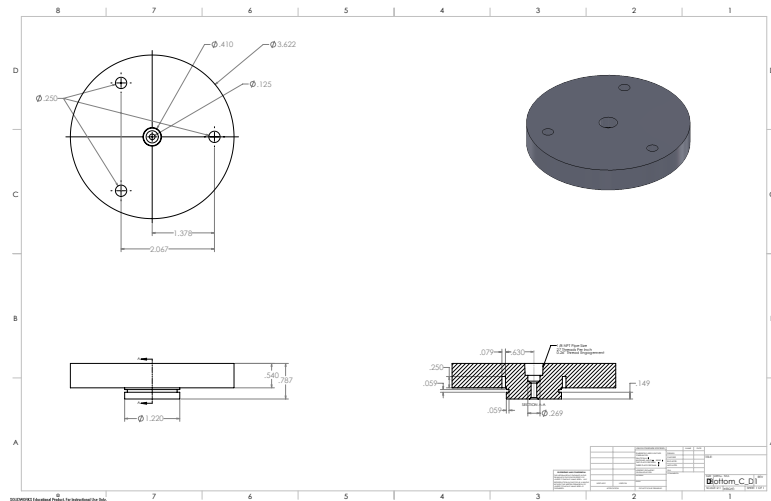


**Figure 2.12:** The bottom end connection design

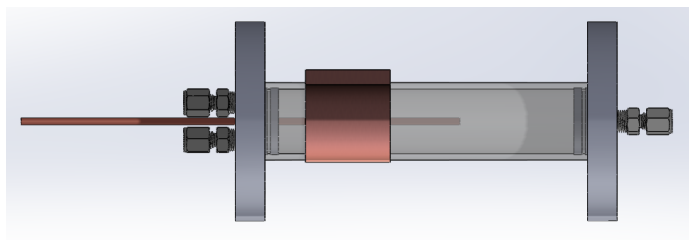


**Figure 2.13:** The plasma reactor is made of two custom design end connections, quartz tube, a copper sheet wrapped around the quartz tube, and inner 1/8 inch copper rod, and 1/8 inch compression fittings.

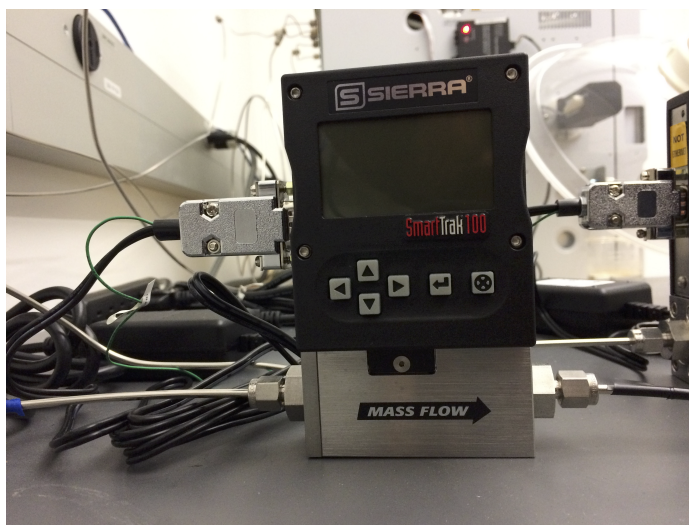


**Figure 2.14:** Mass flow controllers. The top is the rated for carbon dioxide and the bottom is rated for methane.





**Figure 2.15:** Hydrogen and methane purifiers.



**Figure 2.16:** Moisture filter was used between the outlet of the plasma reactor and GC.

## Chapter 3

# RESULTS AND DISCUSSION FOR WATER TREATMENT

This chapter contains a discussion of the previous DBD reactor designs (Fig. 3.1), their advantages and disadvantages, summary of their specific pH results, and the path from one DBD reactor design to the next to finally the final DBD reactor design. The second half of this chapter will discuss the various result (pH,  $NO_3^-$ , and  $NO_2$  rate) of reactor five (the final design). The results themselves are split into cases of amount of  $NaHCO_3$  in distilled water and grouped together for best representation of the data. Therefore, the order is as such: 0 and 1 mg, 2, 5, and 10 mg, 15, 20, and 50 mg, and finally baseline results. The chapter will end with a brief summary.

### 3.1 Progression of DBD Reactor Design and Results

#### 3.1.1 Reactor 1

##### 3.1.1.1 Design

The progress of designing a DBD reactor for water treatment started with replicating a common DBD reactor [174, 175]. The idea was to have a familiarity building and operating a DBD reactor before proceeding to designing a unique reactor. Fig. 3.2 shows reactor 1 in operation. The dimensions of reactor 1 went through some revision before the final parameters were chosen. Both copper electrodes were of equal width and length, 20 mm and 203.2 mm respectively. The dielectric (quartz tube) inner diameter was 10 mm and the outer diameter was 12 mm. The electrodes were wrapped around the quartz tube. The distance between both electrodes was 145 mm with the power electrode 20 mm from the end of the quartz tube. The distance from the end of the tube to the surface of the water was 25 mm. A rubber stopper was use to seal the quartz tube as well as allowing an entrance for the plastic tube carrying the argon gas. The flow rate of the argon gas was 21 slm. All the dimensions were chosen based on a trail and error bases that provided the best stability of the plasma while maintaining a length of the plasma plume that would reach the surface of the water.

The issues with reactor 1 was that the design was not structurally sound and inconsistence of the plasma. The electrodes would frequently sliding causing

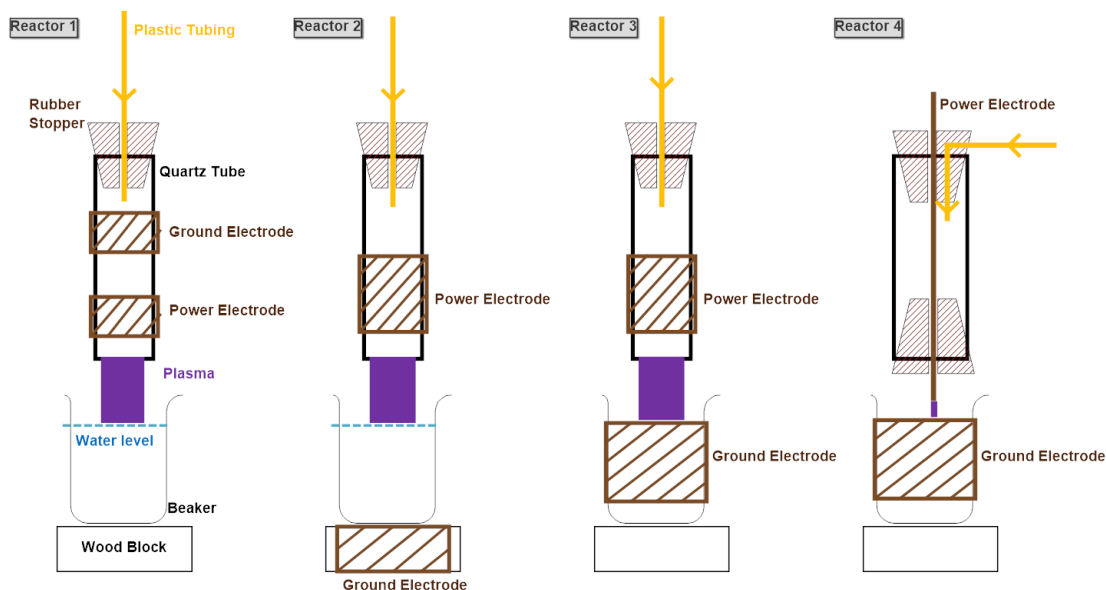


**Figure 3.1:** The four reactors used before settling on the final design (discussed in Chapter 2).

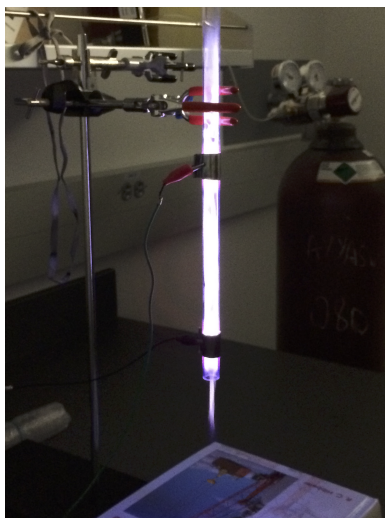


**Figure 3.2:** Reactor 1 in operation.

the dimension to be comprised during experiments. This would lead to the plasma plume to change length. Although the problem of the sliding electrodes was later solved through the use of thermal paste reactor 1 was ultimately an exercise in

understanding the design and operation of a DBD reactor. Note that there will be no voltage or current showed for reactors 1-4 because there were issues with obtaining accurate measurements.

### 3.1.1.2 pH Results

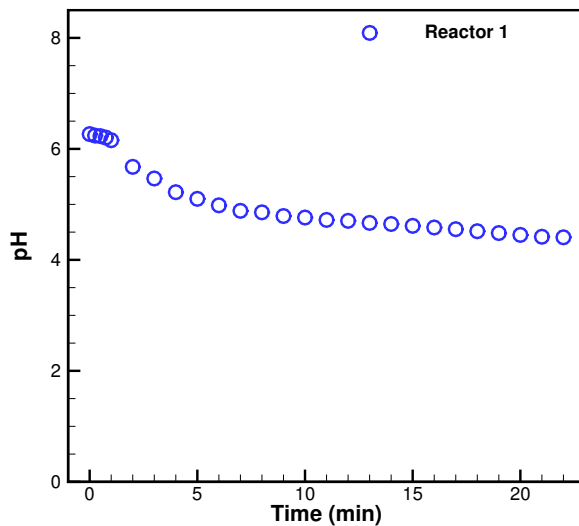


**Figure 3.3:** Reactor 1 pH variation as a function of treatment time for distilled water.

The pH results for reactor 1 can be seen in Fig. 3.3. As can be seen, the pH starts at about 6 and drops to about 4.4 after 22 mins of treatment time. Distilled water was used for these experiments and no sodium bicarbonate was added. The volume of distilled water treated for each experiment was 250 mL. It will be seen later that these pH results were improved upon with the final reactor design. Its worth noting that all pH and  $\text{NO}_3^-$  measurements are average values of three to five sample sets. Error bars were exclude for the sake of clarity.

## 3.1.2 Reactor 2

### 3.1.2.1 Design

Fig. 3.1 and Fig. 3.4 show the schematic and real-time operation of reactor 2. The adjustments from reactor 1 to reactor 2 were moving the ground electrode to underneath the beaker. The ground electrode was wrapped around the wood block. The distance between electrodes, power electrode from the end of the quartz

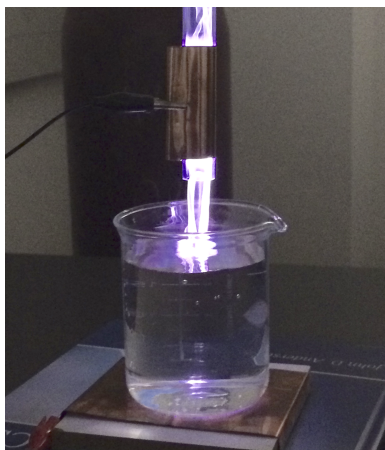


**Figure 3.4:** Reactor 2 in operation.

tube, and quartz tube from surface of the water were all the same as in the reactor 1 design. The power electrodes width was changed to 76 mm. The flow rate stayed the same at 21 slm. The idea behind the changes for reactor 2 was that the electric field around the water would be improve and therefore causing more reactive species to be created leading to improvement in the pH reduction. In addition, with the ground electrode underneath the beaker it was hypothesized that the streamers would penetrate the water trying to reach the ground electrode possibly causing more reaction in the water. It's worth noting that at this point and until the final design (reactor 5) was reached  $NO_3^-$  measurements were not considered.

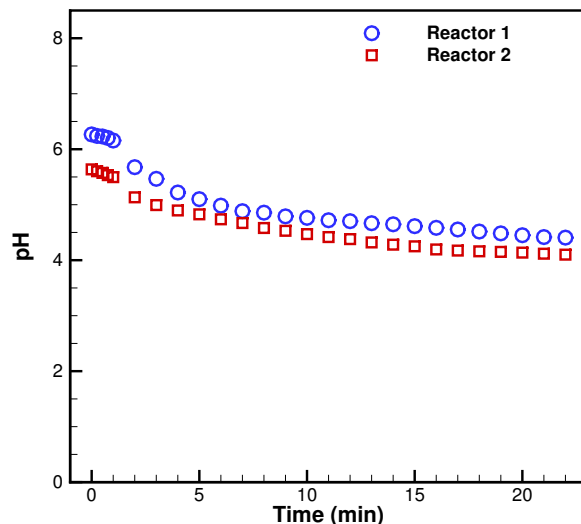
### **3.1.2.2 pH Results**

Fig. 3.5 shows the pH results for reactor 2. The results are very similar to that of Fig. 3.3. Both initial pHs and final pHs started around 6 and end at about 4. This shows that the changes from reactor 1 to reactor 2 were not enough to improve pH reduction dramatically. The key adjustment made from reactor 2 to reactor 3 was to warp the ground electrode around the beaker. Reactor 3 will be discussion in detail in the following subsection.

## **3.1.3 Reactor 3**

### **3.1.3.1 Design**

Fig. 3.6 shows reactor 3 in action. As can be seen in the schematics (Fig. 3.1) of reactors 1-4, the only change from reactor 2 to reactor 3 was warping the ground electrode around the beaker. The thought process for this change was to again improve the electric field by decreasing the distance between the electrodes. The



**Figure 3.5:** Comparison of reactors 1-2 pH variation as a function of treatment time for distilled water.

ground electrode was lined up with the surface of the water so that distance between electrodes was 70 mm (less than half than in the previous two designs).

### 3.1.3.2 pH Results

As can be seen in Fig. 3.7 the pH results are similar to that of reactor 1 and 2. Although, the distances between electrodes was less than half of the previous reactor designs the increase in electric field did not lead to enhancement of the pH reduction. This lead to the beginning steps of designing a system level model. Understanding the chemical reactions in the water was the next step taken that lead to final reactor design.

### 3.1.4 Reactor 3.5 (Volume Based Results)

#### 3.1.4.1 Design

The lack in change of pH results from reactor 1-3 lead to the change in the experiment. The changes came in the way of considering the plasma treated water as an acid,  $HNO_3$ . Previously, we considered the plasma as  $HNO_3$  but that cause problems in calculating the molar concentration of the injecting acid. With the new classification of treated water as  $HNO_3$  the next step was to use this new "acid" to treated normal distilled water and alkaline water (distilled water with the addition of  $NaHCO_3$ ). Using  $HNO_3$  as a the considered acid and not another acid, such as

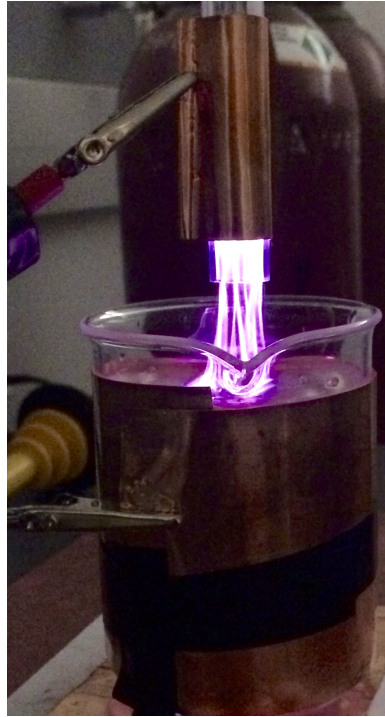


**Figure 3.6:** Reactor 3 in operation.

sulfuric acid, is because one of the reactive specie injected in the water is  $NO_2$  and once the  $NO_2$  dissolves and reacts with the water  $HNO_3$  is created.

#### 3.1.4.2 pH Results

The details of the model can be found in Chapter 2, Section 2.1. Although, the key ideas will be covered here. The first version of the model would guess the molar concentration of the acid but the final version would use the final pH of the plasma created acid and calculate the molar concentration by

$$C_{HNO_3} = 10^{-pH_{HNO_3}} \quad (3.1)$$

where  $C_{HNO_3}$  is the molar concentration of  $HNO_3$  and  $pH_{HNO_3}$  is the pH of the acid. Using Eq. 3.1 and Eq. 2.32 a predication of pH variation as function of treatment volume was possible. Fig. 3.8 shows comparison of measured, model prediction, and based line of pH variation as a function of treatment volume for distilled water with 10 mg of dissolved sodium bicarbonate. The based line results is the pH variation for untreated distilled water. This was done to provide more evidence that the treated water could be considered as  $HNO_3$  acid. As can be seen

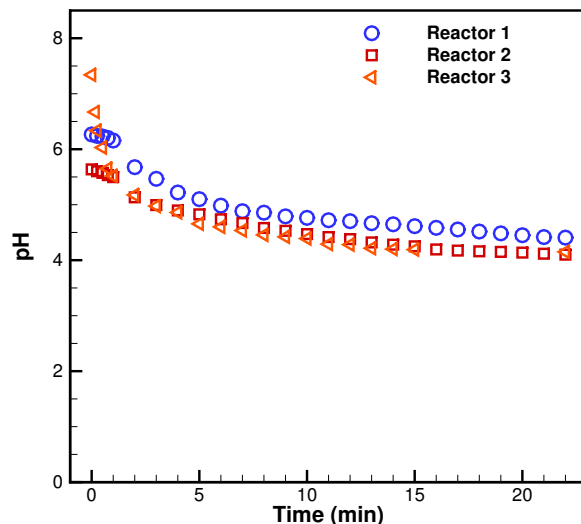


**Figure 3.7:** Comparison of reactors 1-3 pH variation as a function of treatment time for distilled water.

in Fig. 3.8 the model accurately predicates the measured data. The based line data does not change. The  $HNO_3$  model would service as the base for the system-level model. Before reaching the final design of the DBD reactor, a glow discharge plasma was considered next.

### 3.1.5 Reactor 4

#### 3.1.5.1 Design

Reactor 4 (Fig. 3.1 and Fig. 3.9) had a copper solid rod (powered electrode) mounted vertically using a quartz tube with rubber stoppers at both ends. The rubber stoppers were equipped with holes wide enough in order to hold the copper rod in place. The copper rod has a diameter of 3.175 mm and length of 30.48 cm. It should be mentioned that the length of the powered electrode has no significant role to play in the plasma properties and was chosen to be long enough to facilitate the installation (shown in Fig. 3.1). The argon gas was flow through a plastic tube that came in on the side of the top rubber stopper. The flow rate was 21 slm. The copper rod was 4 mm from the surface of the water.

#### 3.1.5.2 pH Results

Reactor 4's pH results can be seen in Fig. 3.10 as well as pH results for reactors 1-3. Its obvious that reactors 1-4 all the very similar pH reduction results.



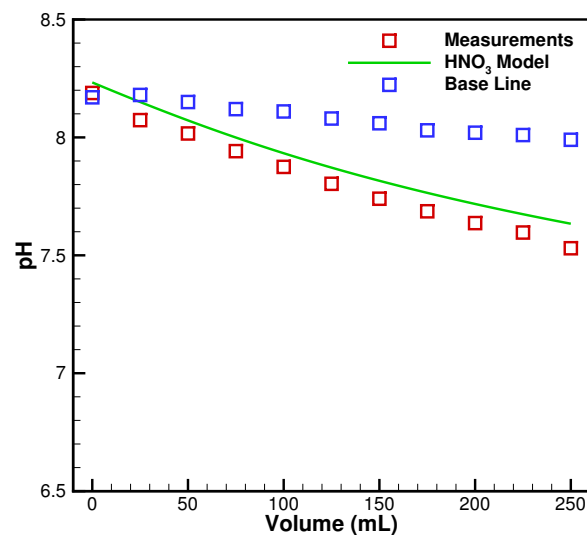


**Figure 3.8:** Comparison of measured, model prediction, and based line of pH variation as a function of treatment volume for distilled water with 10 mg of dissolved sodium bicarbonate.

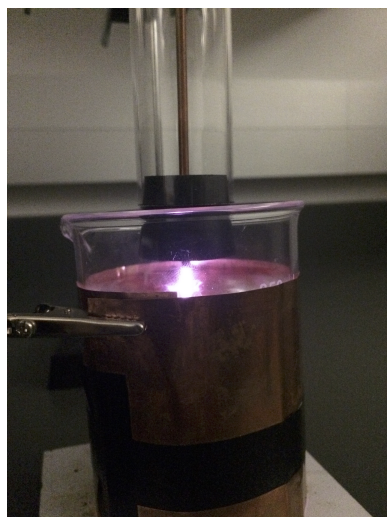


**Figure 3.9:** Reactor 4 in operation.

One key difference from reactor 4 results is that reactor 4 has a delay response to the plasma treatment. Reactor 1-3 results have an almost immediate decrease in

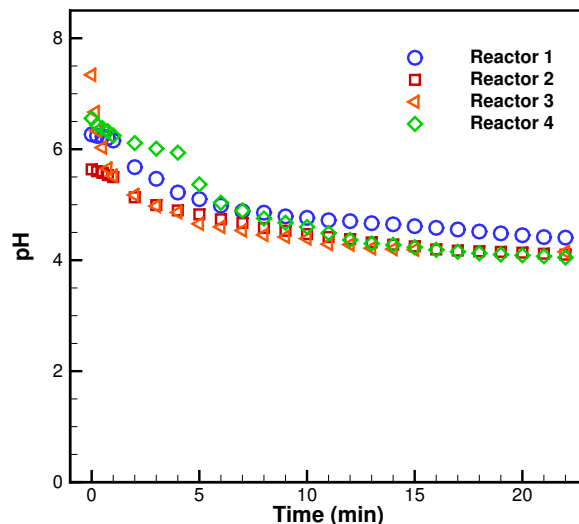


**Figure 3.10:** Comparison of all reactor 1-4 pH variation as a function of treatment time for distilled water.

pH where as it take five minutes to see the the same decrease rate in reactor 4's pH results.

### 3.1.6 Reactor 5: Versions 1 and 2

#### 3.1.6.1 Design

The design of reactor 4 lead to the use of stainless steel capillary tube as the powered electrode. The argon gas was flowed through the tube. The thought process was that a stainless steel capillary tube with a inner and outer diameter of 2 mm and 3 mm, respectively, would enhance the electric field. The argon gas was flowed through the tube. A detailed breakdown of the design of reactor 5 can be seen in Chapter 2. There were two version of reactor 5 before reaching the final design: the first version had the distance between the capillary tube and the surface of the water as 1 mm and the second had the distance as 14 mm. The third and final design had the distance as 29 mm.

#### 3.1.6.2 pH Results

Fig. 3.11 shows comparison of all reactors' pH variation as a function of treatment time for distilled water. From Fig. 3.11, it can be see that versions 1 and 2 for reactor 5 have almost identical results to that of the previous reactors. The most dramatic of results is that of the final design of reactor 5. It's very clear that

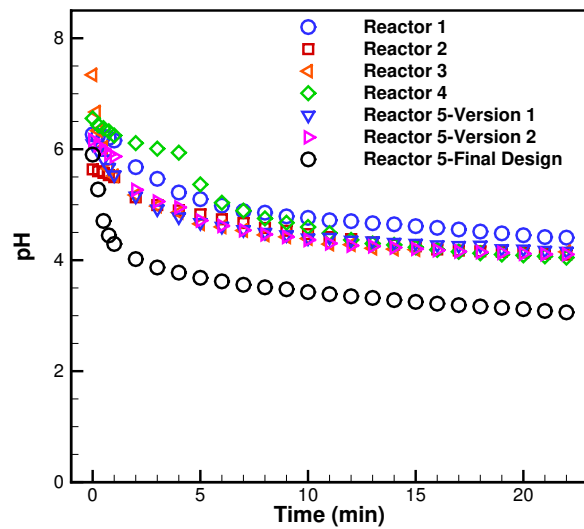


**Figure 3.11:** Comparison of all reactors pH variation as a function of treatment time for distilled water.

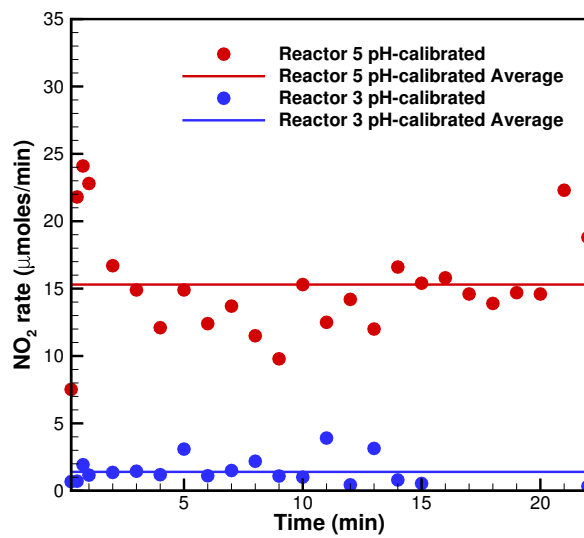


**Figure 3.12:** Comparison of  $NO_2$  rate of reactor 3 vs reactor 5

in the first minute, the final design had a greater slope than all other reactors. For this reason, the final design of reactor 5 was ultimately chosen. It worth mentioning that after the first minute of plasma treatment all reactors' pH results had the very similar slopes. Fig. 3.12 shows the comparison of  $NO_2$  rate of reactor 3 vs reactor 5. The  $NO_2$  rate for reactor 5 is almost 11 times greater than that of reactor 3. Fig. 3.12 shows the possible reason for the dramatic difference in pH reduction for reactor 5 in comparison to all other reactors. Since reactors 1-4 had similar pH results, reactor 3 was used as representative for reactors 1, 2 and 4 pH results. The  $NO_2$  rate data was found using the system-level model.

## 3.2 Final Results & Discussion

This section presents the results obtained for the plasma treatment of distilled water with dissolved sodium bicarbonate and analyzes the results using two system-level models - one based on calibration using pH data and the other based on the nitrate concentration measurements. The experiments involved dissolving a predetermined mass of sodium bicarbonate in 250 ml of distilled water followed by its treatment using the atmospheric pressure streamer discharge set-up described earlier. The two quantities measured in this work include the hydrogen ion concentration (pH) and the nitrate ion concentration. The mass of dissolved sodium bicarbonate varied from 0 mg (pure distilled water) to 50 mg (200 mg/L alkalinity) with the plasma treatment time fixed at 22 minutes. The pH and nitrate concentration were measured at intervals of 1 minute except during the first minute when measurements were made at 15 s, 30 s and 45 s. Before presenting the treatment results, we first present some data on the electrical characteristics of the atmospheric pressure streamer discharge used for the water treatment.

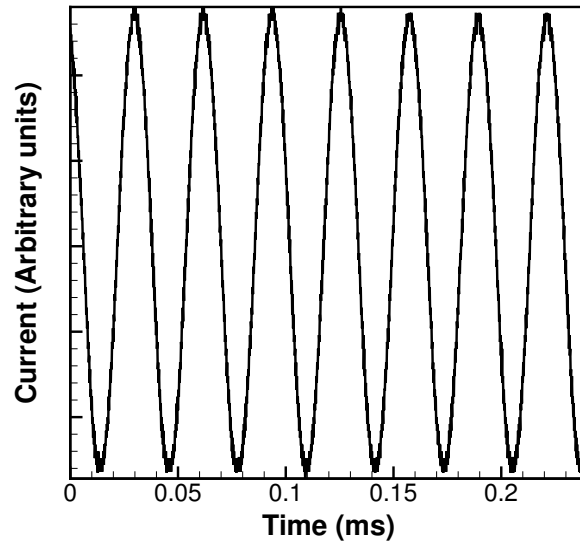
### 3.2.1 Electrical Characteristics

Fig. 3.13 shows the atmospheric pressure streamer discharges in action during a typical water treatment experiment. Fig. 3.14 shows the time history of the current flowing through the circuit prior to plasma ignition. It can be seen clearly that the signal is sinusoidal with a time period of about 0.035 ms thereby translating to a frequency of about 28 kHz. Even though the voltage history is not shown here, it was sinusoidal with a peak voltage of about 16 kV.

In contrast, Fig. 3.15 shows the time history of current after the streamers are ignited and the differences are immediately obvious. Specifically, a single cycle can further be divided into sinusoidal sub-cycles with the peak value increasing from one sub-cycle to another. The time period of each sub-cycle is comparable to the time period of current prior to plasma ignition. This behavior can be directly attributed to the combined effect of the propagating streamer discharge and the applied sinusoidal voltage. When a streamer is generated, its length increases over time until it comes in contact with the water surface at which stage its propagation



**Figure 3.13:** A representative image of the atmospheric pressure streamer discharge in action during a typical water treatment experiment.



**Figure 3.14:** Time history of current through the atmospheric pressure streamer discharge set-up prior to ignition. The frequency of the sinusoidal current was obtained as 28 kHz.

is halted. This is clearly observed in the time history of the current signal. The increase in length of the streamer can be correlated with a decreasing load resistance which in turn translates to an increasing peak current. This increase in peak current occurs until the streamer propagation ends when it comes in contact with the water

surface (streamers are not powerful enough to propagate in water in this case). This instant is accompanied by a spike in the time history of current. Once this happens, the next streamer is generated and the process continues. The speed of propagation of these streamers can be estimated using the time period of the signals once the streamers are ignited and the distance between the electrode tip and the water surface. For example, using a distance of 29 mm (for which results are shown here), and a time period of 0.15 ms, the speed of propagation is about 200 m/s.

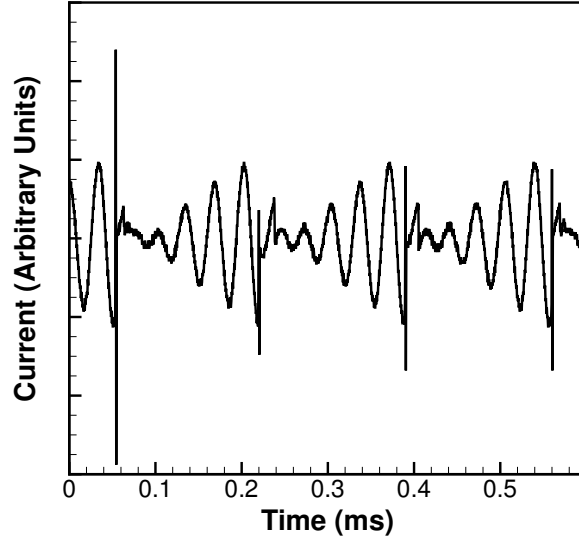


**Figure 3.15:** Time history of current through the atmospheric pressure streamer discharge set-up during the water treatment by streamers. The frequency of the each sinusoidal sub-cycle was obtained as 28 kHz with the spike in current observed at a frequency of about 7 kHz.

### 3.2.2 pH and $\text{NO}_3^-$ Results

Fig. 3.16 shows the measured pH as a function of treatment time for various quantities of dissolved sodium bicarbonate in distilled water including 0 mg, 1 mg, 2 mg, 5 mg, 10 mg, 15 mg, 20 mg and 50 mg. The initial pH of the distilled water without any dissolved bicarbonate is about 6 which increases to a maximum of 8 with the addition of sodium bicarbonate. Table 3.1 summarizes the pH values of the distilled water before and after the addition of sodium bicarbonate. It should be noted that the pH of distilled water even before the addition of bicarbonate is not an absolute constant and demonstrates small variations. This initial pH is an input parameter to our system-level model as will be reiterated while summarizing

**Table 3.1:** A summary of the pH of distilled water before and after the addition of sodium bicarbonate.

$NaHCO_3$ mass (mg)	Initial pH	Final pH
0	5.90	5.90
1	5.85	6.84
2	6.29	7.21
5	6.38	7.43
10	6.03	7.73
15	6.37	7.90
20	6.02	7.99
50	6.35	8.15

results from the model. Fig. 3.16 shows that the plasma treatment leads to a reduction in the pH much like a titration curve between the weak base (sodium bicarbonate solution) and a strong acid. In particular, while treatment of distilled water without any added sodium bicarbonate demonstrates a rapid reduction in pH right from the start of treatment, 15 mg of dissolved sodium bicarbonate leads to an initial period of slow decrease in pH followed by a rapid reduction when almost all bicarbonate is consumed by the treatment. The presence of bicarbonate leads to a time delay in the pH reduction. The similarity of the plasma treatment response to a titration curve is attributed to the injection of  $NO_2$  into the water which in turn leads to the formation of  $HNO_3$  that consumes the bicarbonate ions leading to the formation of sodium nitrate. In order to present data supporting this claim, the nitrate concentration measured as a function of time is shown in Fig. 3.17. The nitrate concentration increases with plasma treatment time for all dissolved masses of sodium bicarbonate with the overall rate of increase decreasing with increasing initial alkalinity of the treated water.

### 3.2.3 System-Level Model

In order to interpret the observed data and potentially make predictions for other initial concentrations of bicarbonate, we utilize the system-level model. To reiterate, the system model takes in the rate of injection of  $NO_2$  into the treated water by the plasma streamers and predicts the pH and  $[NO_3^-]$  as a function of time. While the rate of injection of  $NO_2$  is a function of plasma operating parameters, it is not directly controllable and depends on various geometrical and electrical parameters including those of the treated water. As a result, the rate of injection of  $NO_2$  ( $d(NO_2)/dt$ ) is used as a fitting parameter in order to interpret the measured data for pH and  $[NO_3^-]$ .

Two different approaches were adopted to explain the measured data with the only difference between the two approaches being the calibration of the the

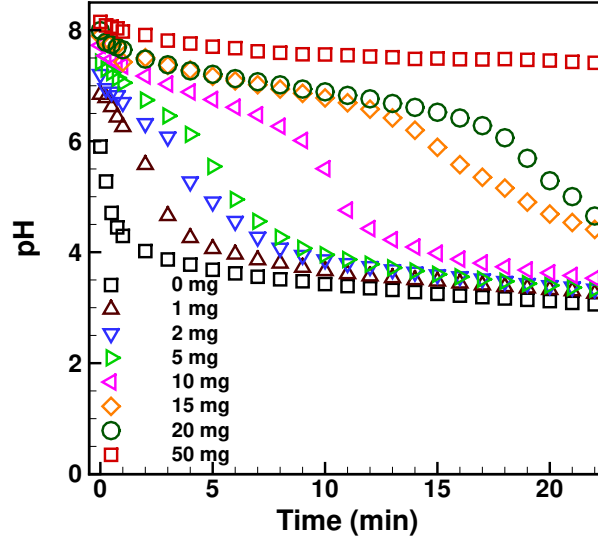


**Figure 3.16:** Variation of pH of the treated water as a function of treatment time by atmospheric pressure streamer discharges for various masses of dissolved sodium bicarbonate ranging from 0 mg to 20 mg. The 50 mg data is not shown in this plot but is presented during analysis using the system-level model.

$d(NO_2)/dt$  parameter. For the first approach, we calibrated the  $d(NO_2)/dt$  parameter using the pH measurements. In this approach, we assumed a constant  $d(NO_2)/dt$  value during the time interval between any two pH measurements (typically 1 minute for most of our data points) and solved for the  $d(NO_2)/dt$  value that led to agreement between the system-level model predictions and the measurements. In other words, this process began with the initial pH value (which is same as the final pH value of the previous time interval - one minute except for the first minute of treatment where more measurements were made) and computed the  $d(NO_2)/dt$  value during that time interval. This process allowed for the  $d(NO_2)/dt$  fed into the system-level model to vary during the 22 minutes of treatment and is referred to as the *pH-calibrated*.

While the above approach is excellent for fitting measured data exactly, we also compare measurements and system-level model predictions using the average  $d(NO_2)/dt$  value based on the variable  $d(NO_2)/dt$  obtained as part of the *pH-calibrated* approach. To reiterate, this second approach is referred to as *pH-calibrated Average* and utilizes a constant (time-averaged)  $d(NO_2)/dt$  as input to the system-level model. Finally, our third approach is based on  $[NO_3^-]$  data and is



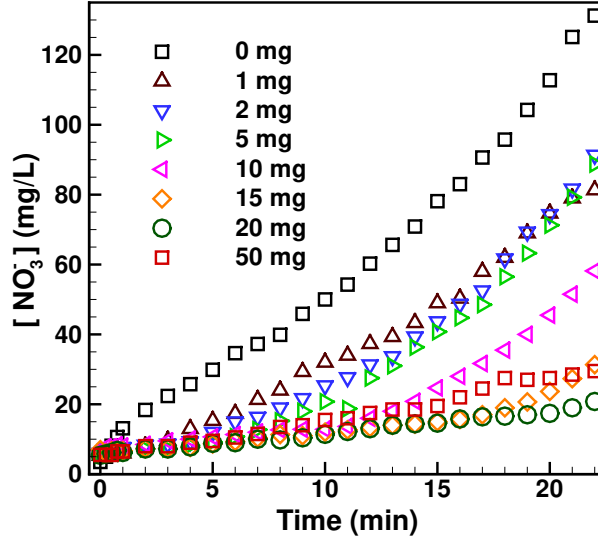


**Figure 3.17:** Variation of  $[NO_3^-]$  in the treated water as a function of treatment time by atmospheric pressure streamer discharges for various masses of dissolved sodium bicarbonate ranging from 0 mg to 20 mg. The 50 mg data is not shown in this plot but is presented during analysis using the system-level model.

built on the fact that two constant  $d(NO_2)/dt$  regions (approximately linear variation in  $[NO_3^-]$ ) could be observed in all  $[NO_3^-]$  measurements as a function of time. The third approach uses a constant  $d(NO_2)/dt$  rate until a certain time during treatment (referred to as the *breakeven time*) and a different (increased) constant  $d(NO_2)/dt$  rate for times after the *breakeven time*. Physically, the *breakeven time* could be viewed as an estimate of the time required to consume all sodium bicarbonate initially dissolved in the distilled water. As a result of the use of two constant  $d(NO_2)/dt$  rates in the third approach, we refer to it as the *Two-rate model*. Each of the model approaches outlined above were used to interpret and analyze the pH and  $[NO_3^-]$  variation with time for various masses of dissolved sodium bicarbonate.

### 3.2.4 0 mg, 1 mg, & 2 mg

Figs. 3.18-3.20 summarize the results obtained for treatment of pure distilled water with 0 mg of dissolved sodium bicarbonate. Fig. 3.18 shows the variation of  $d(NO_2)/dt$  rate as calibrated using the measured pH variation with time along with the average value of  $d(NO_2)/dt$  over the 22 minute duration. The average  $d(NO_2)/dt$  rate was determined to be  $15.3 \mu\text{mol}/\text{min}$  indicating that the streamers inject an estimated  $336.6 \mu\text{mol}$  of  $NO_2$  into the treated water. Fig. 3.19 shows

the comparison of measured and predicted pH variation with time and as expected the model predictions using a variable  $d(NO_2)/dt$  rate (*pH-calibrated* model) agrees well with the measured pH. Also, the *pH-calibrated Average* model uses the average  $d(NO_2)/dt$  rate of  $15.3 \mu\text{mol}/\text{min}$  based on the *pH-calibrated* model. The predictions of the *pH-calibrated Average* model and the *pH-calibrated* model are both comparable with each other indicating that using the average  $d(NO_2)/dt$  value leads to a good description of the pH reduction due to plasma treatment. However, when comparing the predictions of  $[NO_3^-]$  using both *pH-calibrated* and *pH-calibrated Average* models with the measurements, the agreement is less impressive. In particular, both models lead to severe under-prediction of  $[NO_3^-]$ . On closer observation of the measured  $[NO_3^-]$  concentrations in Fig. 3.20, it is clear that the variation is almost linear with a variation of  $128 \text{ mg}/\text{L}$  over 22 minutes. With the volume of treated water being  $250 \text{ mL}$ , this is equivalent to injecting  $32 \text{ mg}$  of  $NO_3^-$  ions over 22 minutes or equivalently, about  $1.5 \text{ mg}$  of  $NO_3^-$  ions every minute. Assuming that the streamers inject  $NO_2$  gas into the water which is then converted into  $NO_3^-$  ions through the reaction



where  $124 \text{ mg}$  of  $NO_3^-$  ions requires  $138 \text{ mg}$  of  $NO_2$  gas injected,  $1.5 \text{ mg}/\text{min}$  of  $NO_3^-$  ion injection is equivalent to  $1.67 \text{ mg}/\text{min}$  (or  $27 \mu\text{mol}/\text{min}$ ) of  $NO_2$  injection. While this is an approximation to the  $NO_2$  injection rate, closer examination of the measured  $NO_3^-$  ions showed that using  $d(NO_2)/dt = 33.75 \mu\text{mol}/\text{min}$  agrees well with the experimental data. It should be mentioned that the two-rate model for the case of no dissolved  $NaHCO_3$  essentially corresponds to a single-rate model with the breakeven time of  $0 \text{ s}$  (since there is no  $NaHCO_3$  to be consumed). As can be seen from Fig. 3.20, an  $NO_2$  injection rate of  $33.75 \mu\text{mol}/\text{min}$  for the entire treatment time agrees well with the measured  $[NO_3^-]$ . The corresponding pH variation as shown in Fig. 3.19 leads to good overall agreement even though it over-estimates the pH reduction leading to an eventually lower pH ( $2.71$ ) than the measurements ( $3.06$ ).

Figs. 3.21-3.23 summarize the results obtained for treatment of pure distilled water with  $1 \text{ mg}$  of dissolved sodium bicarbonate. Fig. 3.21 shows the variation of  $d(NO_2)/dt$  and the average  $d(NO_2)/dt$  rate was determined to be  $10.49 \mu\text{mol}/\text{min}$  indicating that the streamers inject an estimated  $230.78 \mu\text{mol}$  of  $NO_2$  into the treated water. Fig. 3.22 shows the comparison of measured and predicted pH variation with time and similar to the  $0 \text{ mg}$  case the *pH-calibrated Average* model and the *pH-calibrated* model show good agreement with the measured pH. Although the *emphpH-calibrated Average* model does show deviation in a slightly faster decrease in pH. The two-rate model shows a delay in the pH reduction with rate of  $4.05 \mu\text{mol}/\text{min}$  until a breakeven time of  $9 \text{ min}$  and  $33.75 \mu\text{mol}/\text{min}$  after that which leads to a better agreement. As was seen in the  $0 \text{ mg}$  case and will be seen in other

cases, the *pH-calibrated Average* model and the *pH-calibrated* model severely under-predicted the  $[NO_3^-]$  (see Fig. 3.23). The two-rate model with a breakeven time of 9 min shows good agreement even though the transition period is not full captured by the two-rate model. The transition period not being full captured by the two-rate model is a function of how the model works in that the breakeven time is the intersection of the two different  $d(NO_2)/dt$  rates. Figs. 3.24-3.26 summarize the results obtained for treatment of pure distilled water with 2 mg of dissolved sodium bicarbonate. The 1 mg and 2 mg cases show very similar results to each other due to the 1 mg difference. The 2 mg case results shows all the same characteristics in the emphpH-calibrated Average model, the *pH-calibrated* model, and two-rate model with regards to the pH and  $[NO_3^-]$ .

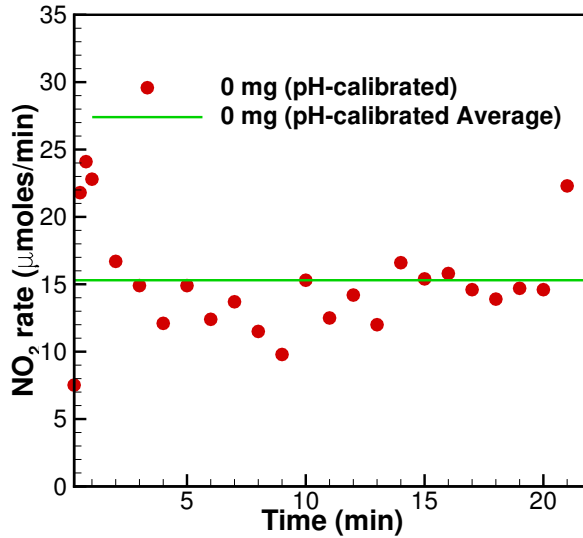


**Figure 3.18:** Comparison of measured and system-level model predictions of  $d(NO_2)/dt$  variation as a function of treatment time for distilled water with 0 mg of dissolved sodium bicarbonate.

### 3.2.5 5 mg & 10 mg

Figs. 3.28 and 3.29 compare the results obtained using all three models with the measured pH and  $[NO_3^-]$  for 5 mg of dissolved sodium bicarbonate. As expected, the pH-calibrated model agrees well with the measured pH variation since the rate of injected  $NO_2$  is suitably varied with time to enable good agreement. With the average  $d(NO_2)/dt$  of  $11.25 \mu\text{mol/min}$  (see Fig. 3.27), the pH-calibrated Average model also leads to good overall agreement even though the region of rapid decrease

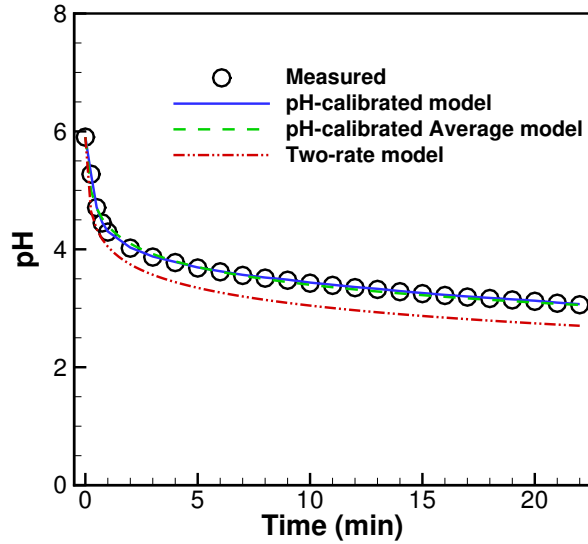


**Figure 3.19:** Comparison of measured and system-level model predictions of pH variation as a function of treatment time for distilled water with 0 mg of dissolved sodium bicarbonate.

in measured pH is predicted with a slight delay by the pH-calibrated Average model. With rates of  $4.05 \mu\text{mol}/\text{min}$  until a breakeven time of 9 min and  $33.75 \mu\text{mol}/\text{min}$  after that, the two-rate model leads to significant under-prediction of the pH decrease until the breakeven time after which the agreement is much better. As in the cases previous, the final pH value predicted by the two-rate model is lower than the measured pH. On the other hand, the agreement with measured  $[\text{NO}_3^-]$  is excellent for the two-rate model. It should be emphasized that the rate of  $\text{NO}_2$  injection after the breakeven time is same as the  $\text{NO}_2$  rate used for the 0 mg, 1 mg and 2 mg case thereby highlighting the consistency of  $\text{NO}_2$  injection across multiple cases.

Figs. 3.31 and 3.32 present the comparisons for 10 mg of dissolved  $\text{NaHCO}_3$  with similar findings as the 5 mg case. Fig. 3.30 shows the variation of  $d(\text{NO}_2)/dt$  and the average  $d(\text{NO}_2)/dt$  rate was determined to be  $10.49 \mu\text{mol}/\text{min}$  indicating that the streamers inject an estimated  $270.82 \mu\text{mol}$  of  $\text{NO}_2$  into the treated water. Once again, it should be mentioned that the two-rate model uses the same rates before and after breakeven time as the previously considered cases. The breakeven time was observed to be 15 minutes and was the only parameter changed in the two-rate model. As for the 5 mg case, the pH-calibrated Average model delays the onset of the rapid reduction of pH with the two-rate model leading to an even larger time delay.

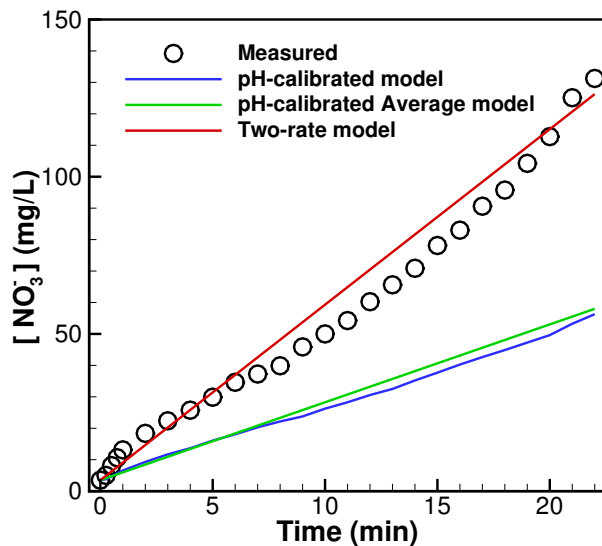


**Figure 3.20:** Comparison of measured and system-level model predictions of  $[NO_3^-]$  variation as a function of treatment time for distilled water with 0 mg of dissolved sodium bicarbonate.

### 3.2.6 15 mg, 20 mg, & 50 mg

Similar trends as in the 5 mg and 10 mg cases were observed for the 15, 20 and 50 mg cases (Figs. 3.33-3.41) with the breakeven time being about 20 minutes for the 15 mg and over the treatment time for 20 and 50 mg cases. In other words, the 20 and 50 mg cases were both explained well with a constant rate of  $4.05 \mu\text{mol}/\text{min}$  over the entire treatment time. Table 3.2 summarizes various parameters based on pH and  $[NO_3^-]$  calibrations for all masses of  $NaHCO_3$  considered in this work. With all the measured results and system-level model predictions presented, it is imperative to point out certain aspects of the comparisons. The atmospheric pressure streamer discharge certainly injects a whole host of species into the treated water with dissolved  $NaHCO_3$ . However, the system-level model assumes the primary species to be  $NO_2$  which is assumed to dissolve in water producing the  $NO_3^-$  ions. With the rate of injection of  $NO_2$  being one of the crucial input parameters that is calibrated using the measurements, utilizing the measured concentration of  $NO_3^-$  ions for this calibration is more accurate considering that the injection of other gases by the plasma will likely not affect the  $NO_3^-$  concentration. On the contrary, the calibration of  $dNO_2/dt$  using pH measurements is likely to be less accurate since most of the other species injected by the plasma play a role in affecting the pH of the treated water. Therefore, relating the pH change directly to the rate of  $NO_2$  injection is not possible. As a result, we hypothesize that the  $dNO_2/dt$  calibrated

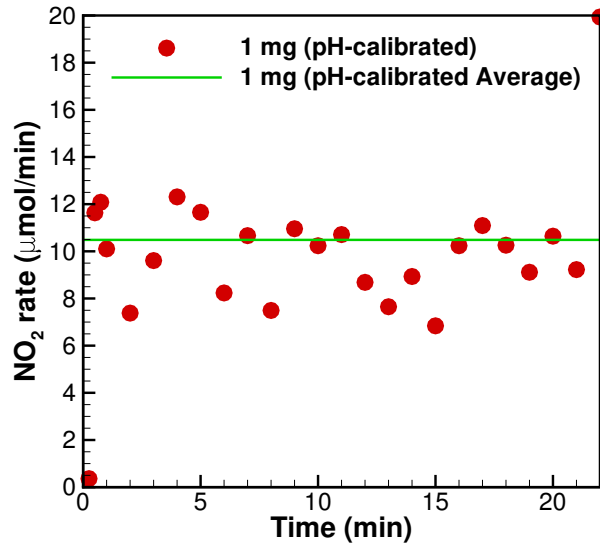


**Figure 3.21:** Comparison of measured and system-level model predictions of  $d(NO_2)/dt$  variation as a function of treatment time for distilled water with 1 mg of dissolved sodium bicarbonate.

based on the  $[NO_3^-]$  (two-rate model) is more representative of the effect of the plasma in terms of  $NO_2$  injection. The deviation between the predictions of the two-rate model and the measurements could partly be attributed to the asymptotic  $d(NO_2)/dt$  rates that are being used thereby not providing a completely accurate description of the transition between the two rates before and after the breakeven time respectively. The proposed two-rate model could potentially be improved by including a finite transition period (as opposed to the instantaneous transition of the two-rate model) during which the  $d(NO_2)/dt$  varies linearly between  $4.05 \mu\text{mol/min}$  to  $33.75 \mu\text{mol/min}$ . However, this would include an additional fitting parameter - the transition duration - apart from the durations for the two asymptotic rates. The requirement for more parameters, while providing greater flexibility to explain the data also leads to greater uncertainties. Therefore, this approach was not pursued in the current work. The other reason for the possible deviation between measured pH and the prediction of the two-rate model is the simplistic nature of the model where  $NO_2$  is assumed to be the primary species injected. It is possible that additional species injection accounts for part of the pH decrease but is not accounted for in the current analysis thereby leading to the deviation.

The other point worthy of discussion is the observed variation of breakeven times as seen in Table 3.2. While the breakeven times for the 1 mg, 2 mg and 5 mg cases being the same could be misleading, it is likely caused by the nature of

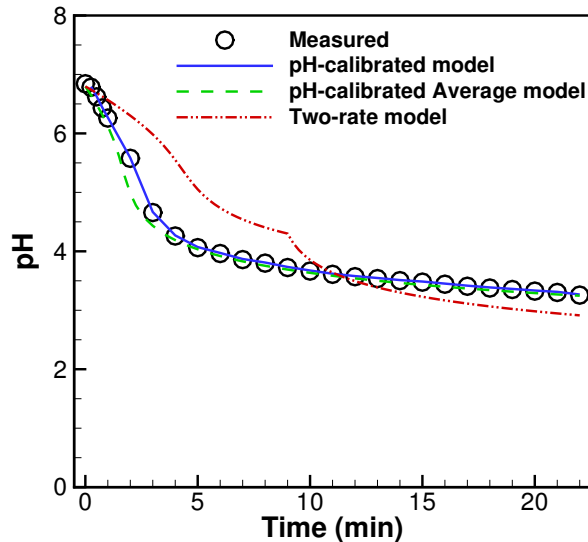
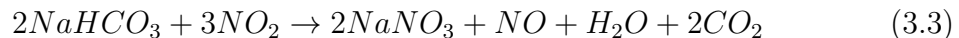


**Figure 3.22:** Comparison of measured and system-level model predictions of pH variation as a function of treatment time for distilled water with 1 mg of dissolved sodium bicarbonate.

the asymptotic analysis where the breakeven time is determined as the intersection point of the asymptotes. It is clear from the measured  $[NO_3^-]$  (Fig. 3.17) data that the 1 mg, 2 mg and 5 mg cases overlap during times less than 5 minutes and times greater than 15 minutes. The breakeven times determined from the intersection of the asymptotes can be compared with an estimate of the time that would be required to consume the given mass of  $NaHCO_3$  in conjunction with the pre-breakeven  $NO_2$  injection rate of  $4.05 \mu\text{mol}/\text{min}$ . The chemical reaction that describes the consumption of  $NaHCO_3$  by  $NO_2$  is given by



where 1 mole (84 g) of  $NaHCO_3$  is consumed by 1.5 moles (93 g) of  $NO_2$ . As a result, 1 mg of  $NaHCO_3$  requires 1.11 mg of  $NO_2$  to be completely consumed. At an injection rate of  $4.05 \mu\text{mol}/\text{min}$  ( $251.1 \mu\text{g}/\text{min}$ ), the time for consumption is obtained as 4.42 min for the 1 mg case thereby reiterating the fact that the breakeven time provides a good order of magnitude estimate of the time required to consume all bicarbonate. For 10 mg, this analysis would predict 44.2 min to consume all  $NaHCO_3$  which is greater than the breakeven time of about 15 min indicating that the rate of injection begins at the pre-breakeven asymptotic rate and then gradually

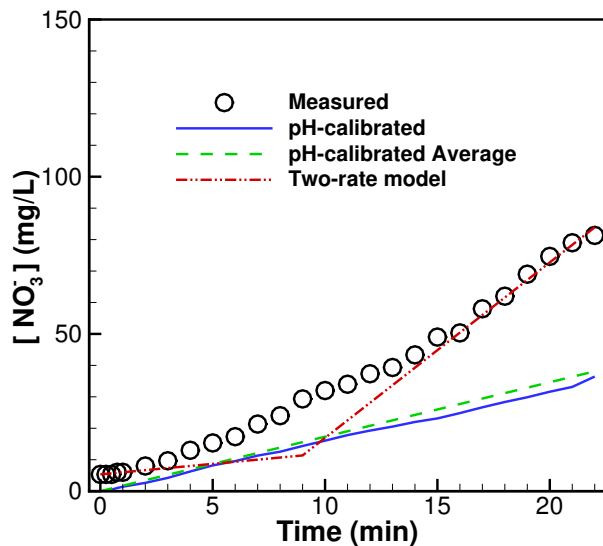


**Figure 3.23:** Comparison of measured and system-level model predictions of  $[NO_3^-]$  variation as a function of treatment time for distilled water with 1 mg of dissolved sodium bicarbonate.

increases to the post-breakeven asymptotic rate of  $33.75 \mu\text{mol}/\text{min}$ . Therefore, utilizing the pre-breakeven asymptotic rate for the entire duration for which  $NaHCO_3$  is consumed leads to deviation from the observed breakeven time. Also, as seen in Table 3.2, the pH-calibrated Average  $NO_2$  rates demonstrate significant variation across various cases thereby making the pH-calibrated Average model infeasible for use as a predictive system-level model to design scaled-up versions of the proposed set-up.

### 3.2.7 Post Treatment

As a final set of measurements, the pH and  $[NO_3^-]$  of the treated solutions was monitored for 14 days with the results for  $[NO_3^-]$  presented in Figs. 3.44 and 3.45. Fig. 3.44 shows the variation of  $[NO_3^-]$  for the first 60 minutes post-treatment by the plasma where it is clearly seen that the  $[NO_3^-]$  increases with time after treatment for all masses of dissolved sodium bicarbonate. While this could seem contradictory, we hypothesize that it could be due to conversion of nitrite (introduced by the plasma) to nitrate. Fig. 3.45 presents the results for  $[NO_3^-]$  over a period of 14 days (336 hours) post-treatment where it is seen that the presence of  $NaHCO_3$  leads to a slightly different behavior. While the nitrate concentration continues to increase throughout the 14 day period for the 0 mg case, the cases with a small quantity of bicarbonate reach a constant nitrate concentration within a few days. On the



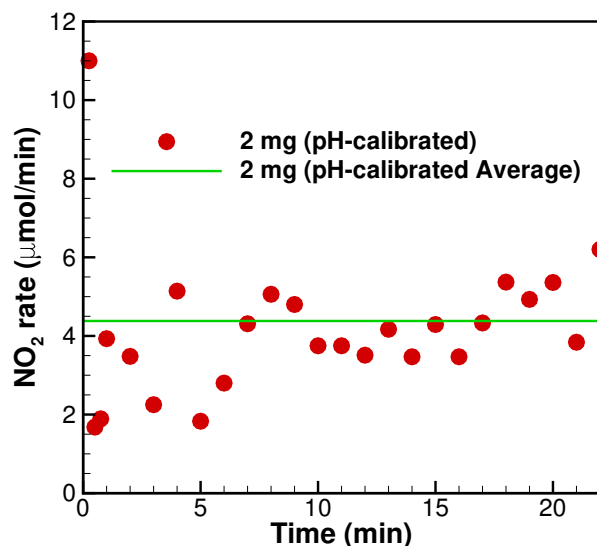


**Figure 3.24:** Comparison of measured and system-level model predictions of  $d(NO_2)/dt$  variation as a function of treatment time for distilled water with 2 mg of dissolved sodium bicarbonate.

other hand, the 15 mg, 20 mg and 50 mg cases eventually lead to a reduction in the nitrate ion concentration. The pH for all of these cases did not change over the period of 14 days.

### 3.2.8 Baseline Results

Measurements of untreated distilled water were taken to provide evidence that the plasma was in fact decreasing the pH and increasing the  $NO_3^-$  concentration. The pH and nitrate concentration (Fig. 3.46 and Fig. 3.49) were measured at intervals of 1 minute except during the first minute when measurements were made at 15 s, 30 s and 45 s over 22 mins. Over the 22 mins both the pH and nitrate concentration do not change. After the 22 mins, measurements were taken every 5 mins over 60 mins. Again, the pH and nitrate concentration (Fig. 3.47 and Fig. 3.50) do not change after 60 mins. Finally, measurements were taken over 14 days intervals of 1 day. As can be seen in Fig. 3.48 and Fig. 3.51, the pH and nitrate concentration do not change. These results are not surprising since there is no chemical reaction mechanism occurring to increase or decrease the pH or nitrate concentration dramatically. There are small changes in the pH and nitrate concentration but those are insignificant, especially in comparison to previous water treatment results.

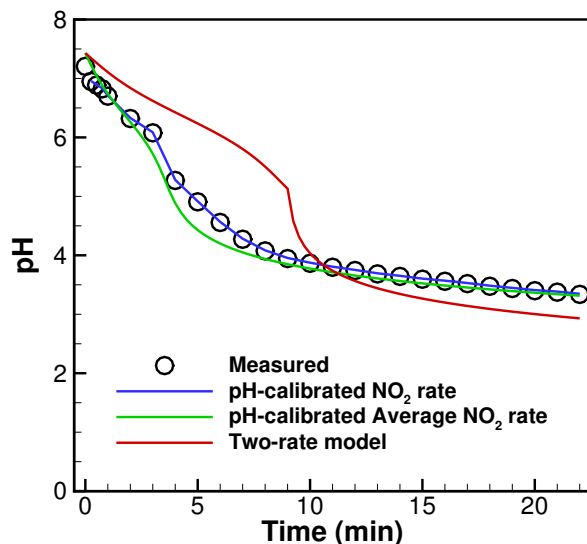


**Figure 3.25:** Comparison of measured and system-level model predictions of pH variation as a function of treatment time for distilled water with 2 mg of dissolved sodium bicarbonate.

### 3.3 Summary

The treatment of bicarbonate-dissolved distilled water using an atmospheric pressure streamer discharge was studied using experiments combined with a system-level model interpretation of the observations. The discharge was ignited using a capillary tube as powered electrode with the ground electrode wrapped around the beaker filled with solution to be treated. Measurements of the current flowing through the discharge indicated streamer propagation velocities of about 200 m/s which interacted with the treated solution to inject  $NO_2$  among other species. The pH and  $[NO_3^-]$  were measured as a function of treatment time for various masses of dissolved sodium bicarbonate. The pH variation with treatment time was shown to be similar to a traditional titration curve of reaction between an acid and base with an initial period of slow variation followed by a steep reduction in pH before settling down at values between 3 and 4. On the other hand, the  $[NO_3^-]$  variation with time demonstrates an increase characterized by two different asymptotic slopes corresponding to early and long-term behavior. The early and long-term rates of  $NO_3^-$  addition by the plasma was consistent across all cases considered thereby motivating the two-rate model as one of the system-level models to explain the measurements. While the two-rate model was based on the  $[NO_3^-]$  measurements, the other model considered in this work was based on the pH measurements where the  $NO_2$  injection rate was predicted based on the observed pH variation.

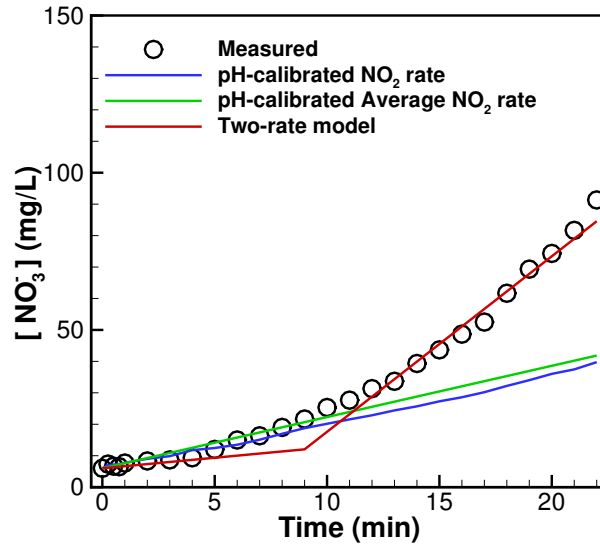


**Figure 3.26:** Comparison of measured and system-level model predictions of  $[NO_3^-]$  variation as a function of treatment time for distilled water with 2 mg of dissolved sodium bicarbonate.

The discrepancies between the measurements and the system-level model indicates that the current model does not account for certain species that contribute to the pH reduction. Nevertheless, the two-rate model is likely to provide a good first estimate of the influence of the plasma for reducing alkalinity of irrigation water. Specifically, the two-rate model could be used to scale-up the system for reducing the alkalinity or increasing the nitrate concentration to desired levels. Finally, the pH and  $NO_3^-$  modifications induced by the plasma were shown to last for at least 14 days with the  $NO_3^-$  concentration increasing post-treatment for limited masses of sodium bicarbonate.

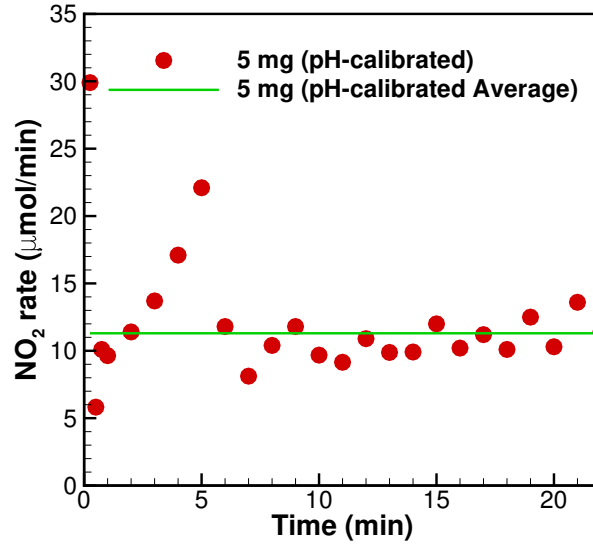


**Figure 3.27:** Comparison of measured and system-level model predictions of  $d(\text{NO}_2)/dt$  variation as a function of treatment time for distilled water with 5 mg of dissolved sodium bicarbonate.

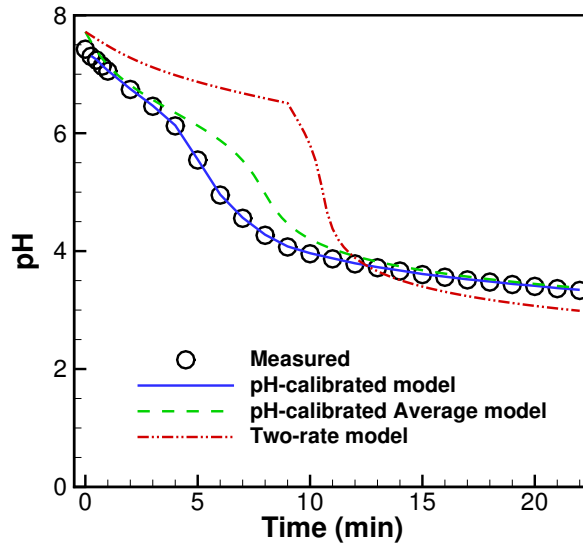


**Figure 3.28:** Comparison of measured and system-level model predictions of pH variation as a function of treatment time for distilled water with 5 mg of dissolved sodium bicarbonate.

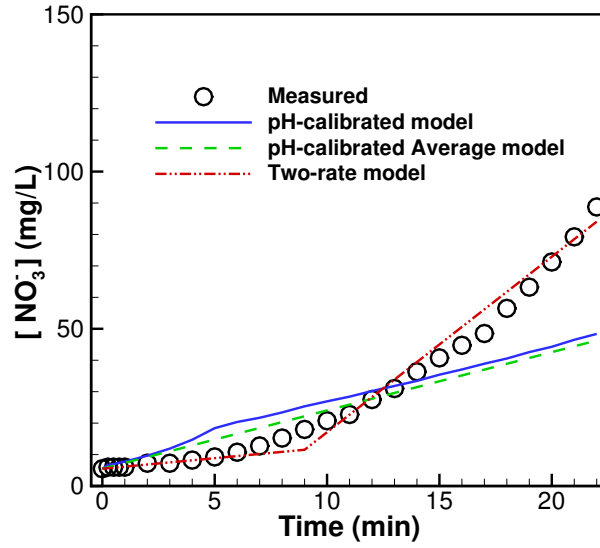


**Figure 3.29:** Comparison of measured and system-level model predictions of  $[NO_3^-]$  variation as a function of treatment time for distilled water with 5 mg of dissolved sodium bicarbonate.

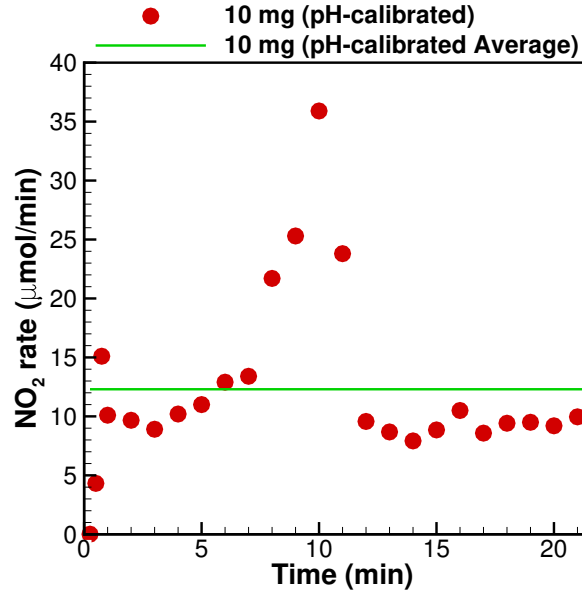


**Figure 3.30:** Comparison of measured and system-level model predictions of  $d(NO_2)/dt$  variation as a function of treatment time for distilled water with 10 mg of dissolved sodium bicarbonate.

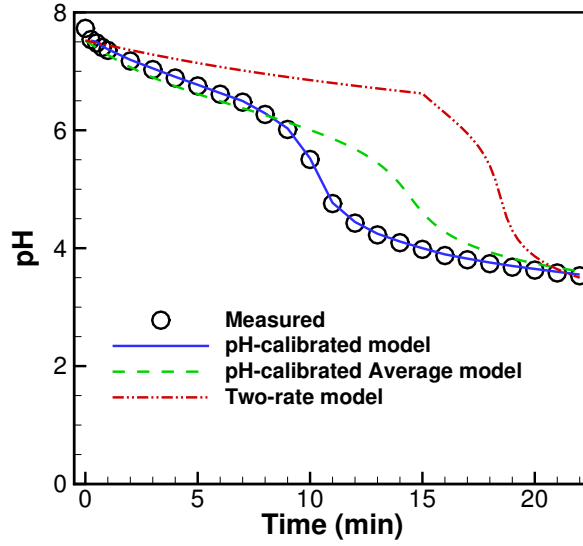


**Figure 3.31:** Comparison of measured and system-level model predictions of pH variation as a function of treatment time for distilled water with 10 mg of dissolved sodium bicarbonate.

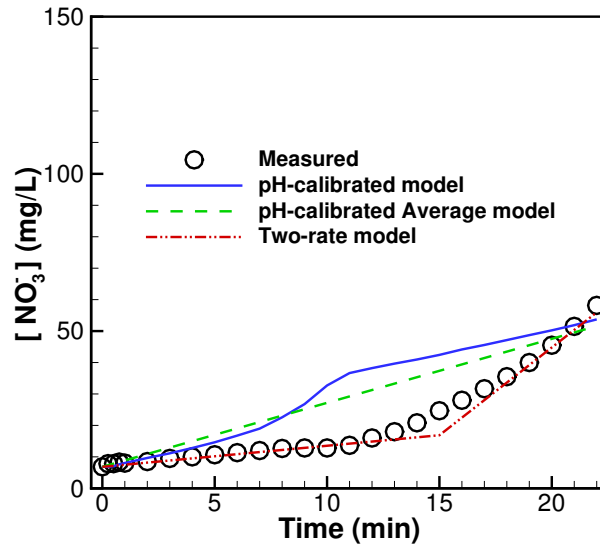


**Figure 3.32:** Comparison of measured and system-level model predictions of  $[NO_3^-]$  variation as a function of treatment time for distilled water with 10 mg of dissolved sodium bicarbonate.

**Table 3.2:** A summary of the pH-calibrated Average  $NO_2$  injection rates and breakeven times for various masses of dissolved sodium bicarbonate.

$NaHCO_3$ mass (mg)	pH-calibrated Average $NO_2$ rate ( $\mu\text{mol}/\text{min}$ )	Breakeven time (min)
0	15.3	0
1	10.49	9
2	9.86	9
5	11.25	9
10	12.31	15
15	14.27	20
20	22.12	> 22
50	2.18	> 22

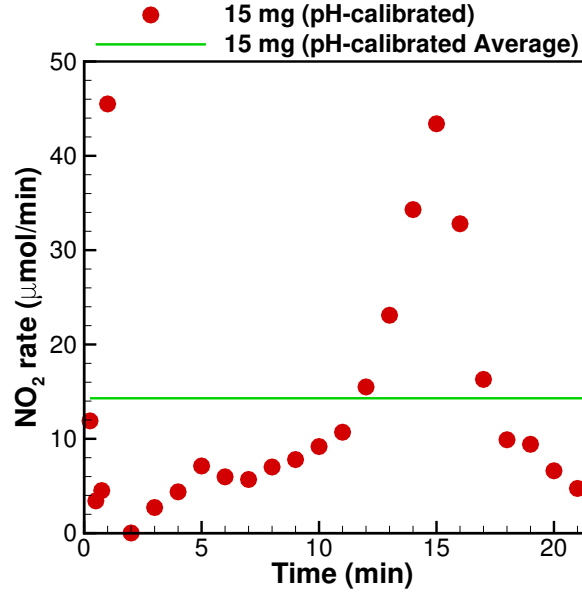


**Figure 3.33:** Comparison of measured and system-level model predictions of  $d(NO_2)/dt$  variation as a function of treatment time for distilled water with 15 mg of dissolved sodium bicarbonate.

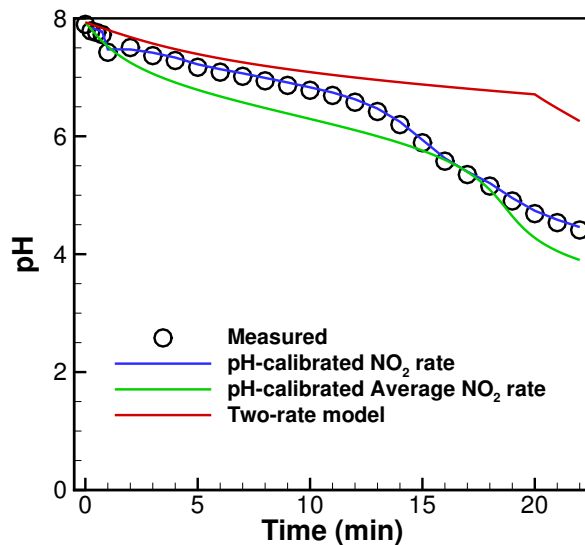


**Figure 3.34:** Comparison of measured and system-level model predictions of pH variation as a function of treatment time for distilled water with 15 mg of dissolved sodium bicarbonate.

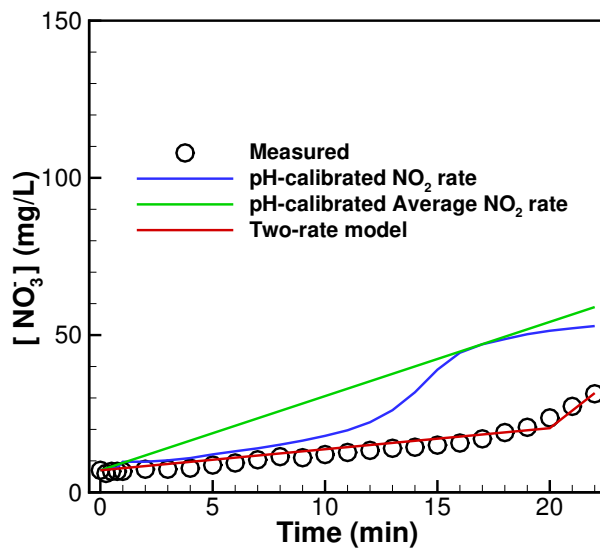


**Figure 3.35:** Comparison of measured and system-level model predictions of  $[NO_3^-]$  variation as a function of treatment time for distilled water with 15 mg of dissolved sodium bicarbonate.



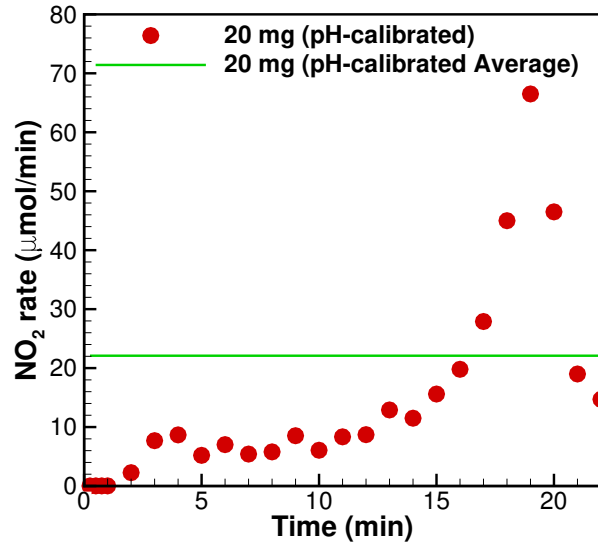


**Figure 3.36:** Comparison of measured and system-level model predictions of  $d(\text{NO}_2)/dt$  variation as a function of treatment time for distilled water with 20 mg of dissolved sodium bicarbonate.

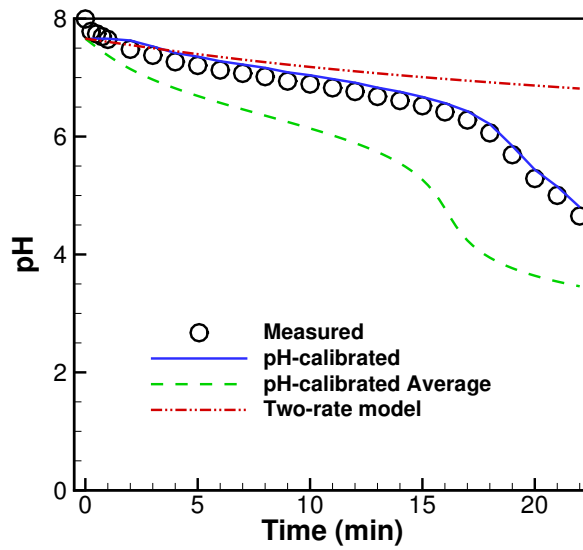


**Figure 3.37:** Comparison of measured and system-level model predictions of pH variation as a function of treatment time for distilled water with 20 mg of dissolved sodium bicarbonate.

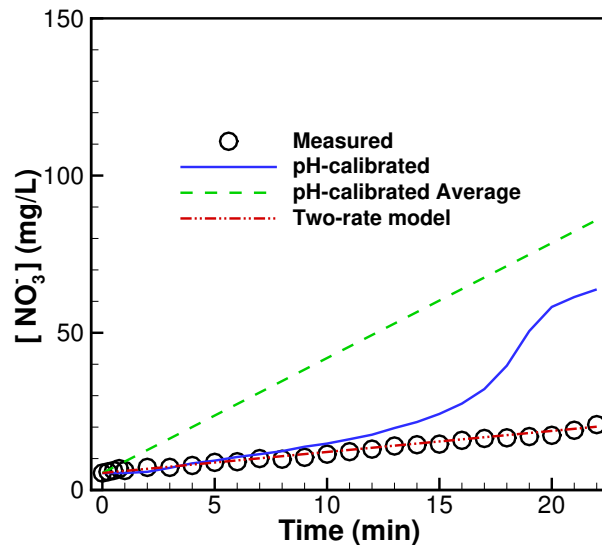


**Figure 3.38:** Comparison of measured and system-level model predictions of  $[NO_3^-]$  variation as a function of treatment time for distilled water with 20 mg of dissolved sodium bicarbonate.

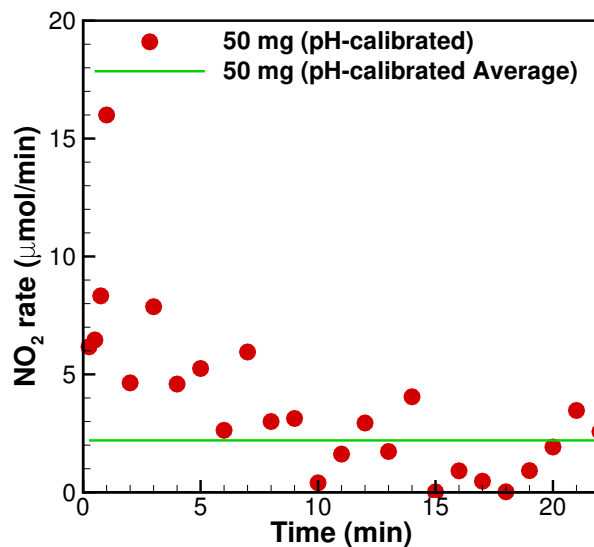


**Figure 3.39:** Comparison of measured and system-level model predictions of  $d(NO_2)/dt$  variation as a function of treatment time for distilled water with 50 mg of dissolved sodium bicarbonate.

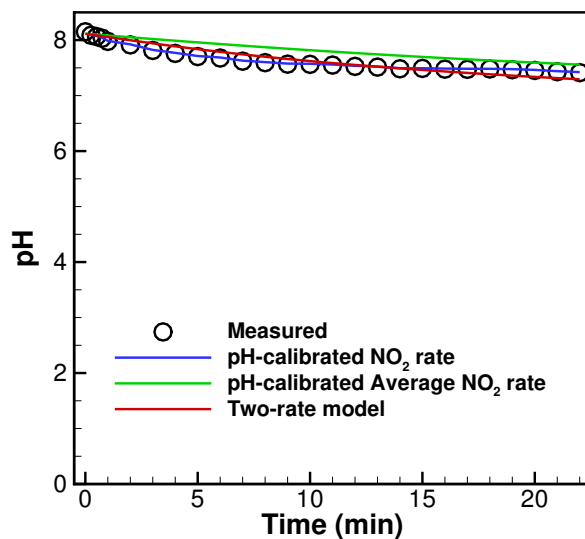


**Figure 3.40:** Comparison of measured and system-level model predictions of pH variation as a function of treatment time for distilled water with 50 mg of dissolved sodium bicarbonate.

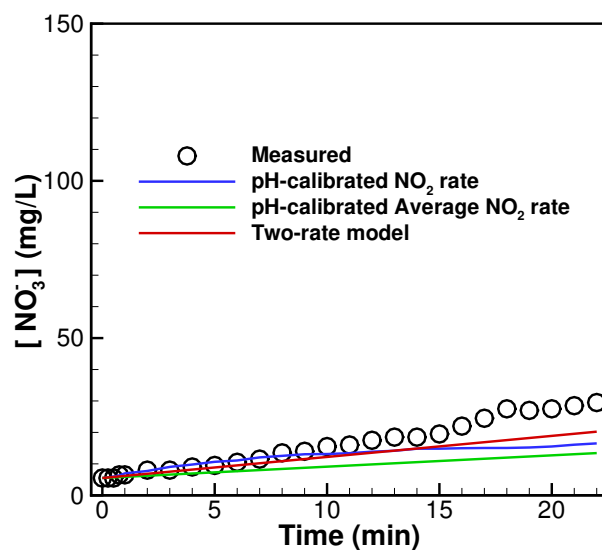


**Figure 3.41:** Comparison of measured and system-level model predictions of  $[NO_3^-]$  variation as a function of treatment time for distilled water with 50 mg of dissolved sodium bicarbonate.

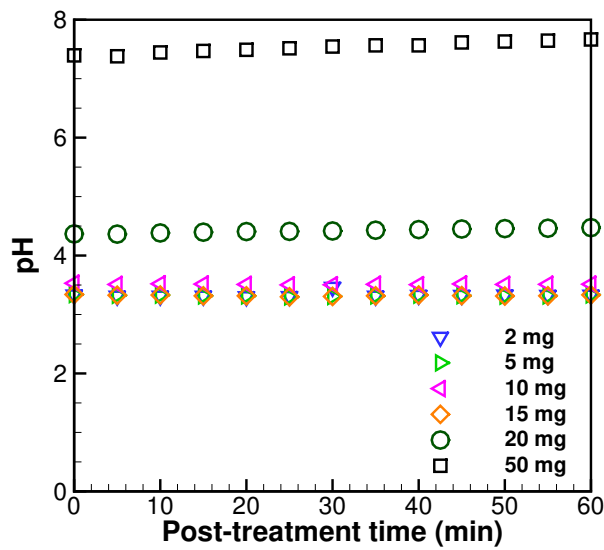


**Figure 3.42:** Measured pH variation with time (up to 60 minutes) after treatment for various masses of dissolved sodium bicarbonate.

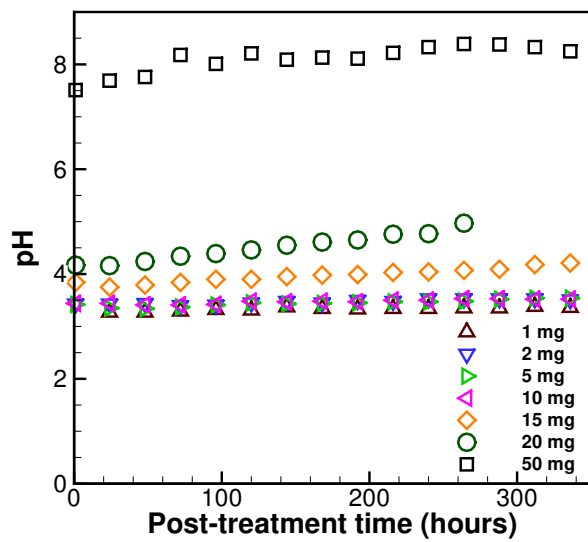


**Figure 3.43:** Measured pH variation with time (up to 14 days) after treatment for various masses of dissolved sodium bicarbonate.

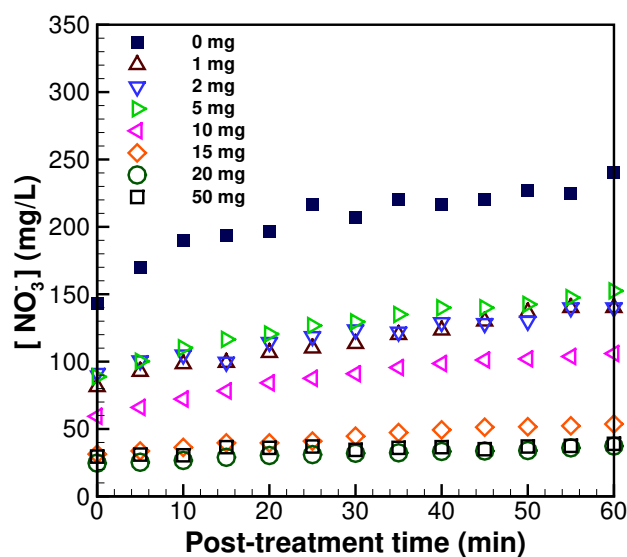


**Figure 3.44:** Measured  $\text{NO}_3^-$  concentration variation with time (up to 60 minutes) after treatment for various masses of dissolved sodium bicarbonate.

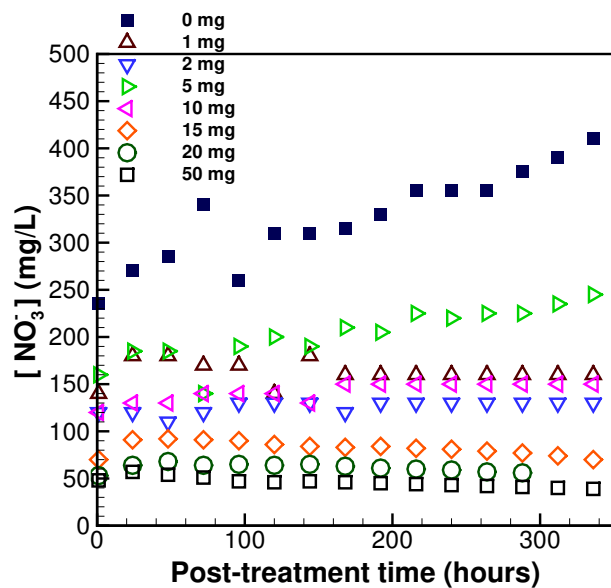


**Figure 3.45:** Measured  $\text{NO}_3^-$  concentration variation with time (up to 14 days) after treatment for various masses of dissolved sodium bicarbonate.

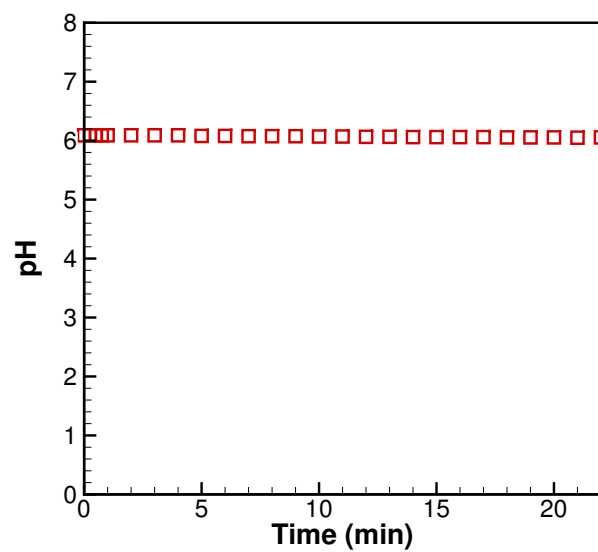


**Figure 3.46:** Baseline pH variation with time (over 22 min).

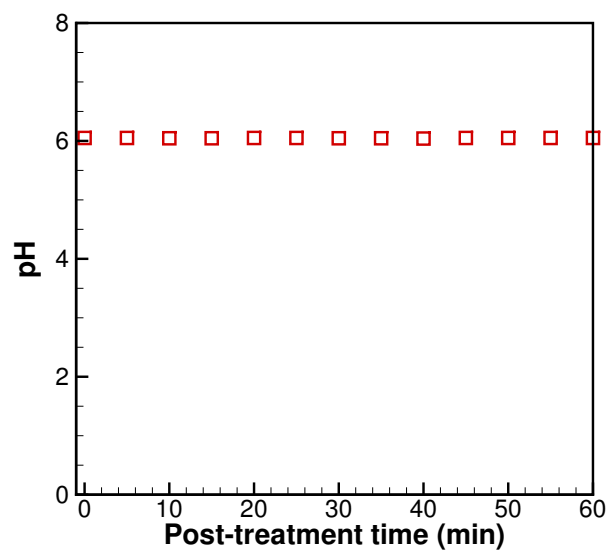


**Figure 3.47:** Baseline pH variation with time (up to 60 mins).

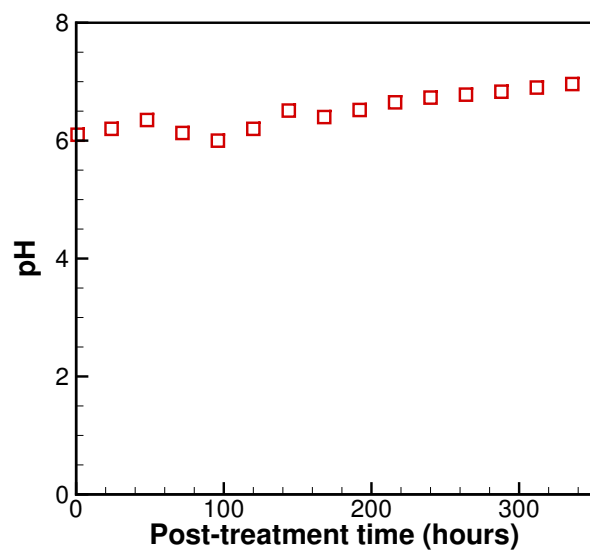


**Figure 3.48:** Baseline pH variation with time (up to 14 days).

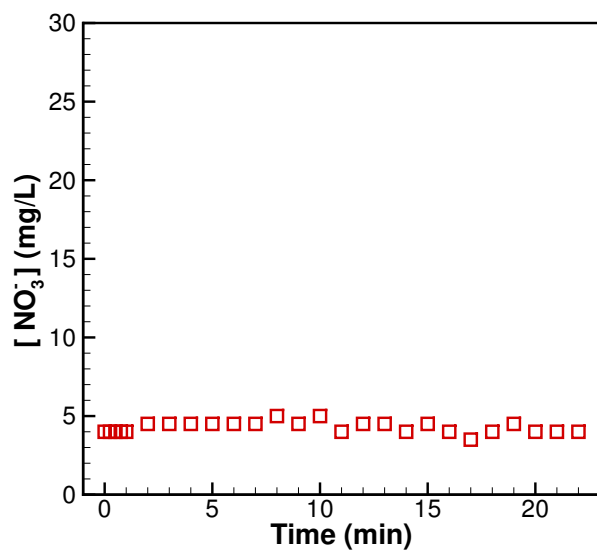


**Figure 3.49:** Baseline  $\text{NO}_3^-$  concentration variation with time (over 22 min).

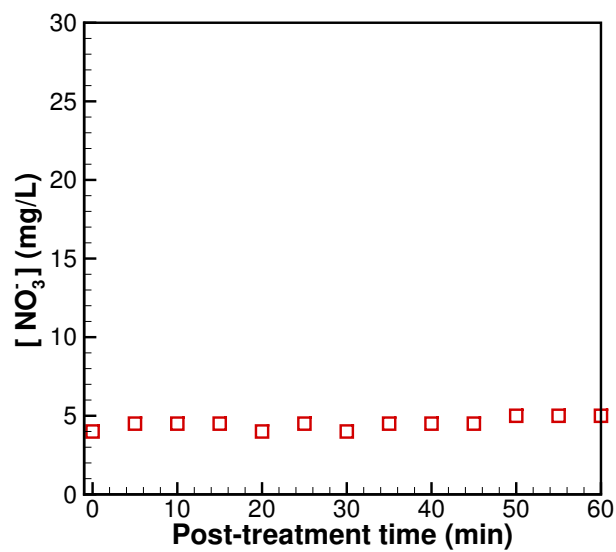


**Figure 3.50:** Baseline  $\text{NO}_3^-$  concentration variation with time (up to 60 mins).

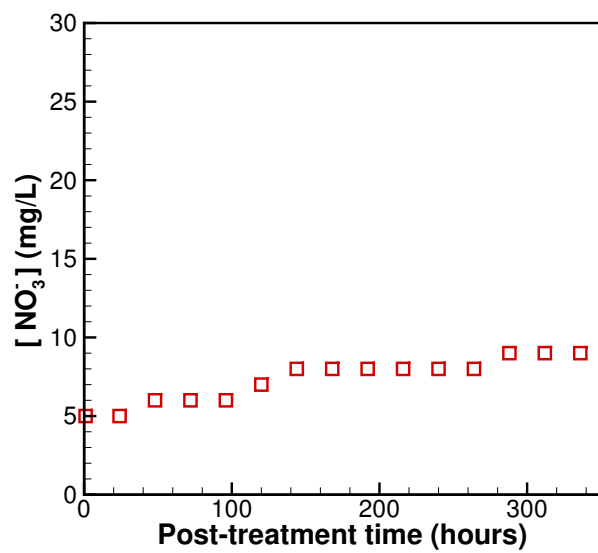


**Figure 3.51:** Baseline  $\text{NO}_3^-$  concentration variation with time (up to 14 days).



## Chapter 4

# METHANE REFORMING USING A DIELECTRIC BARRIER DISCHARGE

This chapter describes the measurements performed using the biogas reforming set-up that was constructed as part of the current thesis. It should be emphasized that the primary focus of the current thesis with regards to the biogas reforming application was restricted to the set-up and demonstrating feasibility of performing measurements through preliminary results. The chapter also presents an overview of the future plan that will be pursued by a future graduate student using this set-up.

### 4.1 Calibration of Gas Chromatograph

Before the experiments were performed, one of the first tasks was to ensure that the gas chromatograph equipment was calibrated using standards for several gases. There were two standards that were used to calibrate the current equipment for detecting various gases including methane, carbon dioxide, carbon monoxide, hydrogen, oxygen, and nitrogen. The low and high standards for in the calibration process for each of the gases is tabulated in Table 4.1. While the carrier gas for the low standard was Argon, the carrier gas for the high standard was Nitrogen. The gas chromatograph equipment is equipped with two detectors including a thermal conductivity detector (TCD) and a flame ionization detector (FID). The TCD uses the difference in thermal conductivity between the detected and carrier gases to determine the concentrations of the trace species. On the other hand, the FID is a more sensitive technique and is typically used for detecting organic compounds that contain a carbon-hydrogen bond. The carbon ions produced during combustion in a hydrogen flame are used to interpret the concentrations of species containing C-H bonds. While an FID cannot usually detect carbon dioxide and carbon monoxide, the GC utilized in the current work is equipped with a methanizer that converts  $CO$  and  $CO_2$  to methane thereby allowing these species to be detected in an FID.

Fig. 4.4 shows the chromatogram of the low standard calibration using the TCD where the various peaks correspond to various species (including hydrogen, oxygen, nitrogen which are some of the prominent species in the current application) included in the standard sample. The residence times of various relevant species are tabulated in Table 4.2 and can be associated with corresponding peaks in Fig. 4.4.

**Table 4.1:** List of all gases and their low and high concentration for standard calibration.

Gas	Low Concentration (ppm)	High Concentration (ppm)
Acetylene	100	4200
Carbon Monoxide	100	4200
Ethane	100	4200
Hydrogen	100	4200
Methane	100	4200
Carbon Dioxide	400	20000
Oxygen	2500	125000
Nitrogen	16900	Balance
Argon	N/A	Balance

**Table 4.2:** List of gases and their residence time.

Gas	Residence Time (min)
Methane	6.778
Carbon Dioxide	8.146
C2s	10.423
Carbon Monoxide	11.452
Hydrogen	2.548
Oxygen	3.626
Nitrogen	4.800

Similarly, Fig. 4.2 shows the chromatogram of the high standard calibration using the TCD with consistent residence times but an enhanced signal as a result of the higher concentration of the various species being detected. Fig. 4.1 and 4.3 show the corresponding chromatograms for the low and high standard calibrations using the FID with a methanizer. The relevant species include methane, carbon dioxide, ethane and ethylene combined into a common C2 species and carbon monoxide. It should be emphasized that carbon dioxide and carbon monoxide are being detected by the FID only due to the presence of a methanizer. It should be noted that the concentrations are linearly extrapolated for voltage values that are not between the minimum and maximum voltage signals corresponding to the low and high standards respectively. The accuracy of the measurements will then depend on the validity of the linearity between output voltage signal and concentration at values outside the calibration range. The instrument can of course be recalibrated using different standards depending on the desired low and high detection limits.

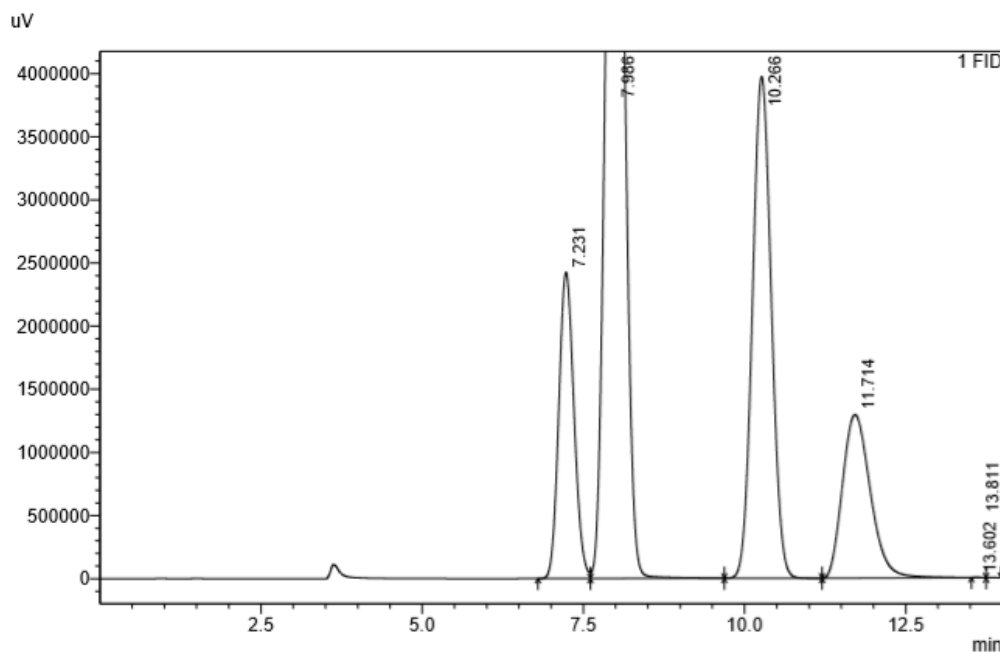


**Figure 4.1:** High standard for GC, FID.

## 4.2 Preliminary Results & Discussion

Once the GC was calibrated using the standards, the next step was to obtain preliminary results demonstrating the feasibility of using the set-up for studying plasma-assisted conversion of biogas. As a first step to studying conversion of biogas,

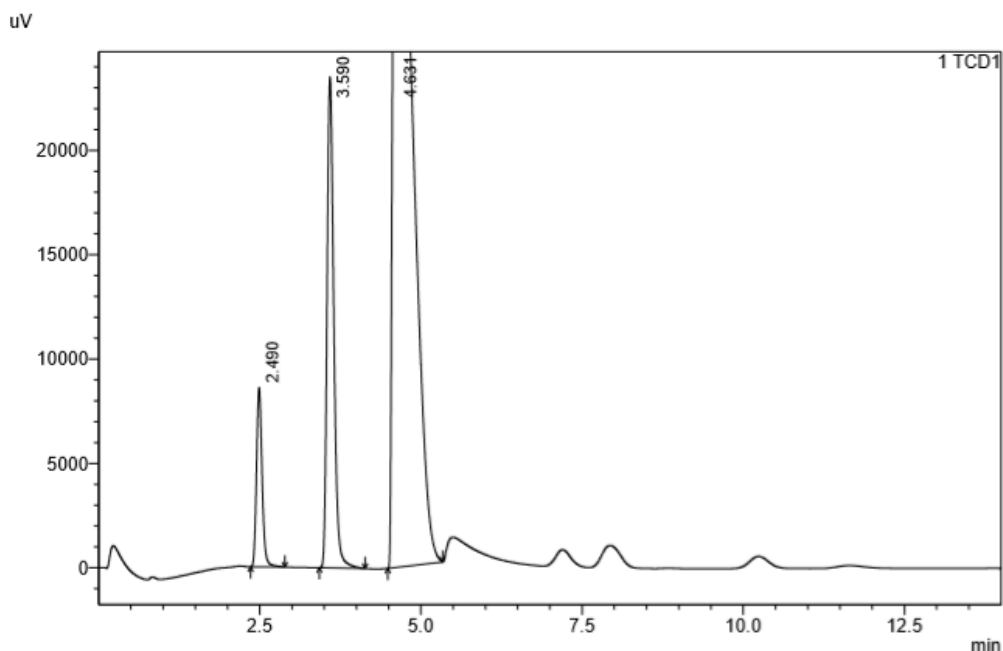


**Figure 4.2:** High standard for GC, FID.

we considered the influence of the DBD on methane. While the overall set-up was described in Chapter 2, there were several modifications introduced as discussed below. The first set of experiments were performed using the 6 in long quartz tube with an outer electrode (powered electrode) that was 3 in wide and wrapped around the quartz tube. The powered outer electrode was located 1 in downstream of the inlet of the quartz tube. The flow rate of methane was varied from 0.025 slm to 1 slm with the chromatogram being used to determine the concentrations of methane and hydrogen after being treated by the DBD plasma. While there are several parameters that affect the conversion, flow rate was the only parameter studied in the current work with the demonstration of the set-up being the primary focus. The DBD plasma was ignited using sinusoidal excitation with a peak voltage around 9 kV at a frequency of around 30 kHz. The plasma with the flowing methane was operated for about three minutes before turning on the GC to ensure that the gas influenced by the plasma is analyzed as opposed to pure methane. Once the GC takes in the required amount of sample (with the opening and closing of the valve), the plasma was turned off. Fig. 4.5 and 4.6 show the chromatograms obtained using the FID and TCD respectively. As can be clearly seen, the FID detects a methane peak with a residence time around 6.8 s with the TCD detecting a hydrogen peak around 2 s. There is also some oxygen and nitrogen detected (possibly from ambient

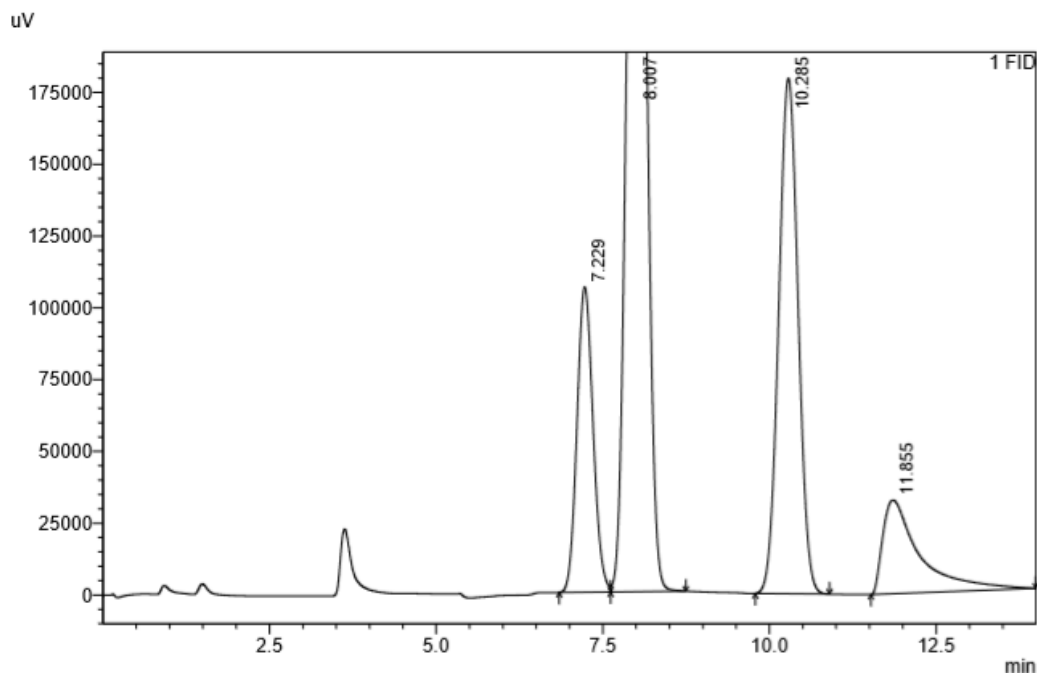


**Figure 4.3:** Low standard for GC, TCD.

air leaking through the connection between the flanges and the quartz tube). The ratio of hydrogen to methane concentrations is used as a measure of the conversion percentage in all results presented in the current work. The measurements were repeated at various flow rates with the results presented in Fig. 4.7. As can be seen, the ratio of hydrogen to methane concentrations measured by the GC is high for some of the measurements performed at low flow rates and is consistently around 10% at higher flow rates. While this may seem to be consistent with the argument that lowering the flow rate increases the residence time of the gas and hence its exposure to the DBD plasma, some of the data may also be inconsistent likely due to the length of the tubing involved between the exit of the quartz tube and the GC. This is one of the deficiencies of the current set-up and should be improved as part of future set-ups.

As part of potential modifications to be considered for the reactor, the 3 in electrode width was split into two electrodes (each of length 1.5 in) with a small gap between them (see Fig. 4.10). One of the reasons for this modification was visual observation of the DBD plasma where the streamers were more intense near the edges (start and end) of the powered electrode (possibly due to electric field concentration at the edge). Having multiple thin electrodes essentially increases

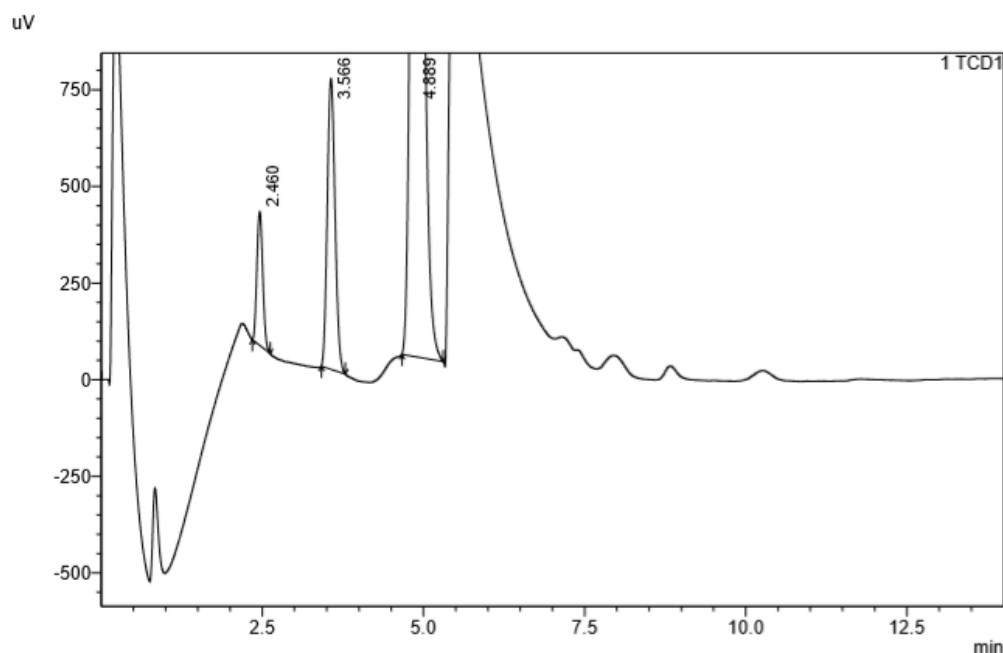


**Figure 4.4:** Low standard for GC, TCD.

the number of edges thereby increasing the overall intensity of the DBD plasma encountered by the flowing gas. Fig. 4.8 shows an image of the modified reactor design with two 1.5 in electrodes. Fig. 4.9 shows the data obtained using the two electrode geometry for various flow rates and spacing between the electrodes. Once again, there is some inconsistency in the data with similar operating parameters leading to a wide range of values for ratio of hydrogen to methane concentration at the outlet of the reactor.

### 4.3 Outlook

While the set-up built as part of the current thesis has been shown to be capable of studying the plasma-assisted conversion of biogas, there are several possible improvements that need to be pursued during the coming year. Some of the possible improvements are outlined here. One of the first things that need to be addressed is the relative lack of reproducibility of conversion data using the current set-up. Even though the plasma dissociates the carbon-hydrogen bond leading to the formation of hydrogen gas, the conversion rates need to be improved significantly to make the technology competitive among other comparable techniques. One of the attractive options to enable us to achieve this is the use of a power supply that can transfer energy more efficiently and selectively to electrons. This can be achieved using a

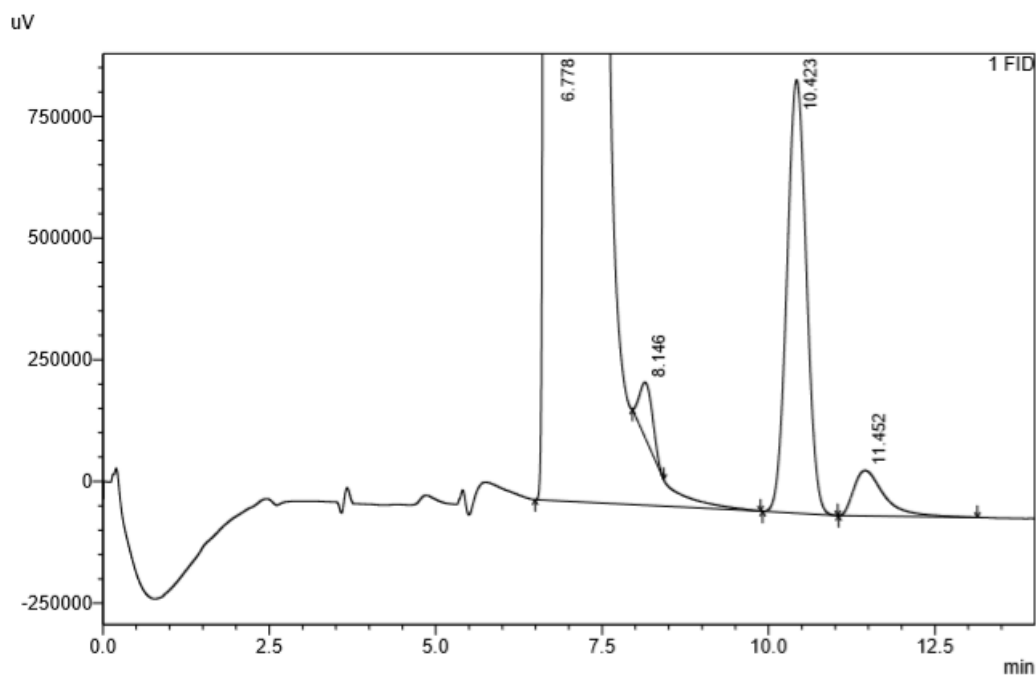


**Figure 4.5:** Typical chromatogram for methane experiment, FID.

power supply that can produce high voltage pulses of short width (nanoseconds) at a given frequency. This would compare favorably with the currently used set-up that utilizes sinusoidal excitation that have a relatively slow rise time (to reach the peak voltage). A faster rise time would allow extremely selective energization of electrons thereby enabling even higher dissociation. Once some of the fundamental deficiencies are addressed, the set-up can be easily used to study conversion of a mixture of methane and carbon dioxide (with all infrastructure to do this already set-up as part of the current thesis). Other parameters that could potentially be varied include the excitation frequency inner electrode cross-section and need to be pursued as part of future work.

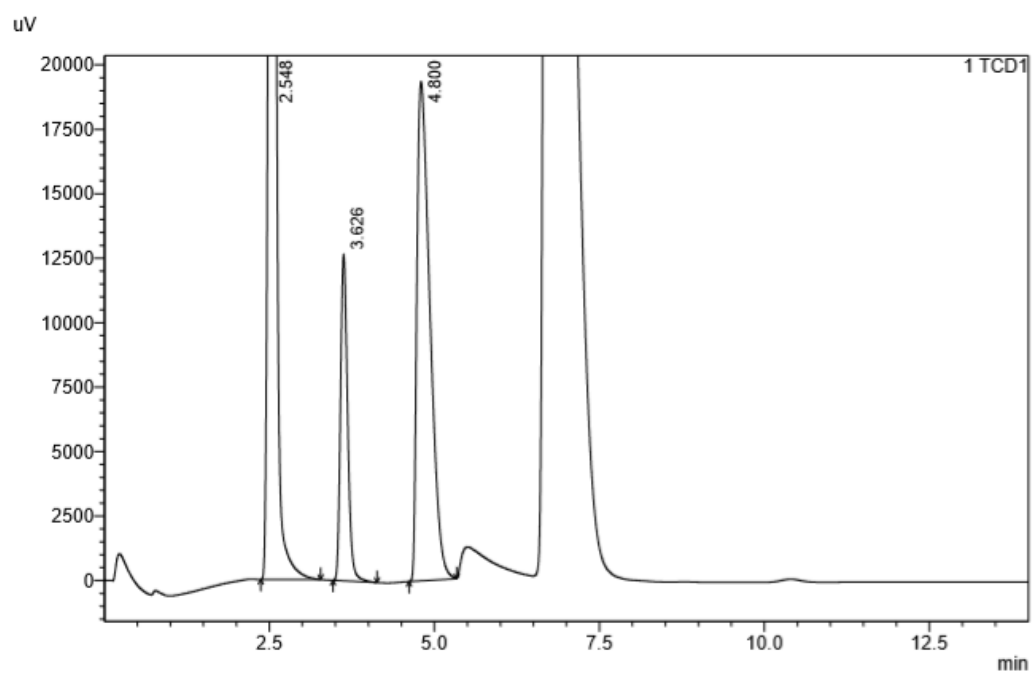


**Figure 4.6:** Typical chromatogram for methane experiment, TCD.



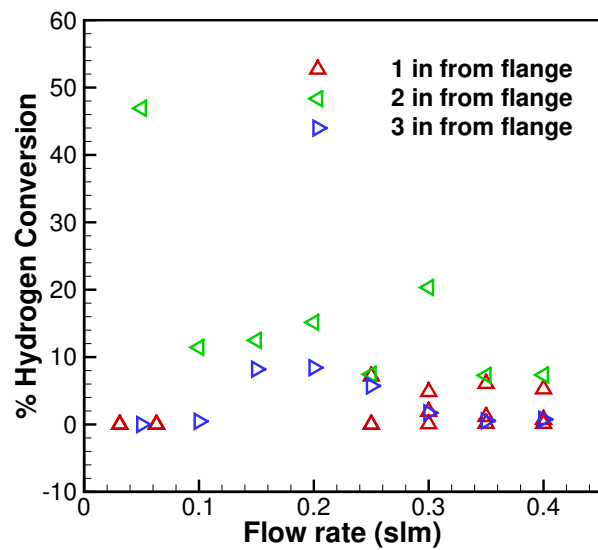


**Figure 4.7:** Methane to hydrogen conversion data done with standard DBD reactor.

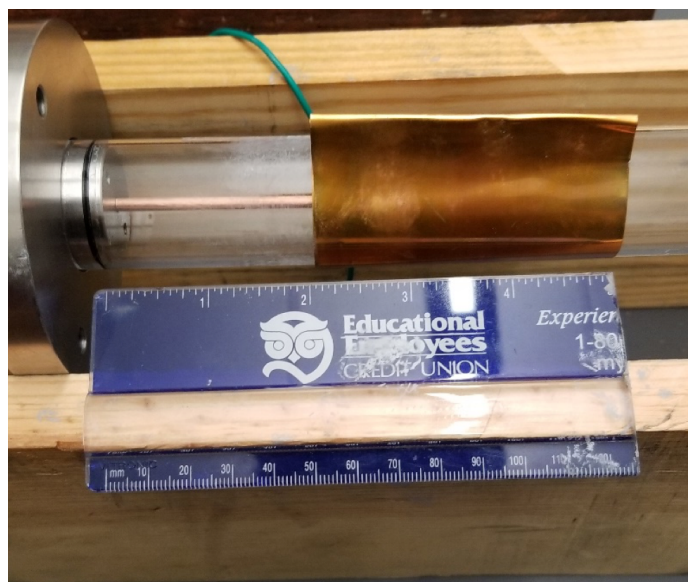


**Figure 4.8:** Standard reactor with changing lengths from end of flange.

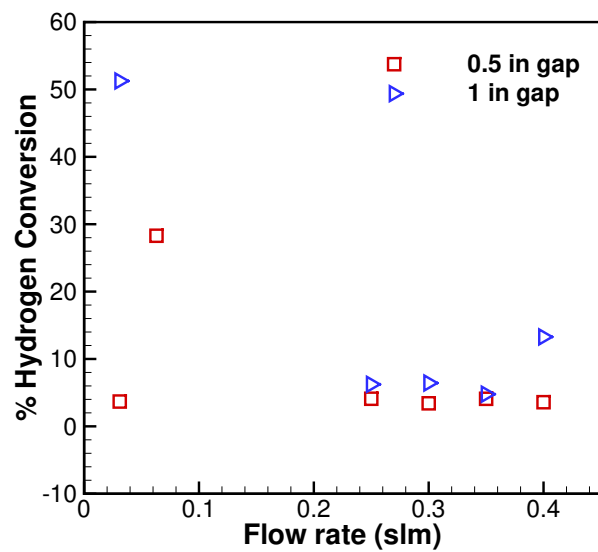


**Figure 4.9:** Methane to hydrogen conversion data done with modified reactor with two electrodes.

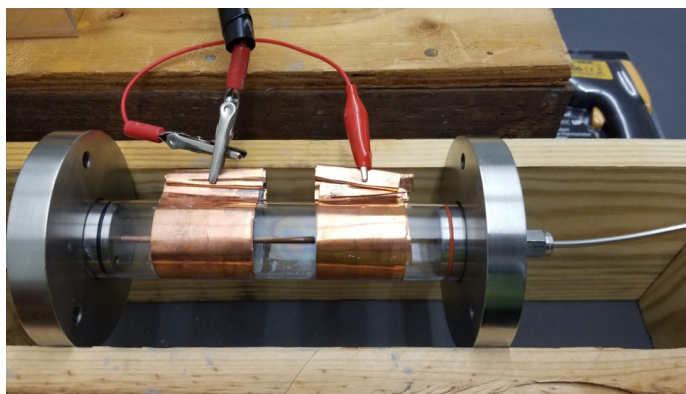


**Figure 4.10:** Modified reactor with two electrodes each of width 1.5 inches.

## Chapter 5

### CONCLUSION & FUTURE RECOMMENDATIONS

The application of atmospheric pressure dielectric barrier discharge on two environmental applications of irrigation water enhancement and biogas conversion were studied. Specifically for the enhancement of irrigation water, the reduction of pH and alkalinity (represented as sodium bicarbonate in this work) and increase in nitrate concentration were the objectives. Environmentally, most crops prefer irrigation water that is in the range of pH 5.5 to 6.5 as well as bicarbonate levels limited to 120 mg/L. The overarching goal of irrigation water enhancement was accomplished through the designing and building of a atmospheric pressure dielectric barrier discharge. Various designs (see Chapter 3) of a DBD reactor were evaluated through the use of pH measurements as a function of time. The final design (see Chapter 2) was shown to have the best pH reduction as a function of time. The discharge was ignited using a capillary tube as powered electrode with the ground electrode wrapped around the beaker filled with solution to be treated. Even though low temperature plasma generates a variety of species, the plasma was represented as the injection of  $NO_2$  so that the study of plasma chemistry within the water could be simplified and possible to model. A system-level model was created to interpret the measurements of pH and  $[NO_3^-]$  concentration. The pH and  $[NO_3^-]$  were measured as a function of treatment time for various masses of dissolved sodium bicarbonate. The pH variation with treatment time had similarities to that of a traditional titration curve of reaction between an acid and base. An initial period of the sodium bicarbonate being consumed resulted in a slow pH variations followed by a saturation of  $HNO_3$  resulting to steep reduction in pH before settling down at values between 3 and 4. Further, the  $[NO_3^-]$  variation with time demonstrates an increase characterized by two different asymptotic slopes corresponding to early and long-term behavior. The early and long-term rates of  $NO_3^-$  were consistent across all cases considered. This consistence verified the two-rate model (one half of the system-level model) as a viable explanation for the  $[NO_3^-]$  measurements. The other half of the system-level model was based on the pH measurements where the  $NO_2$  injection rate was predicted based on the observed pH variation. Finally, the pH and  $NO_3^-$  modifications induced by the plasma were shown to last for at least 14 days with the  $NO_3^-$  concentration increasing post-treatment for limited masses of sodium bicarbonate.

With the development of a system-level model to predicate pH reduction and  $[NO_3^-]$  concentration as a function of treatment time, there is still significant amount of work that can be preformed to improve the system-level model. A future recommendations for the plasma-assisted water treatment is the the improvement in the system-level to take into consideration more chemical reactions created by the plasma. In addition, the use of an open source plasma chemistry solvers, such as OpenFOAM, could greatly improve the pH and  $[NO_3^-]$  predications and can consolidate the system-level model into one unified model.

The other half of this work, plasma-assisted biogas conversion was studied and primary results were demonstrated. As in the plasma-assisted water treatment application, a unique and specific atmospheric pressure DBD was designed and built. The DBD was designed with two stainless steel flanges connected by a quartz tube (dielectric). A copper capillary needle was used as the ground electrode whereas a copper sheet wrapped around the dielectric was used as the power electrode. The DBD went through a few modifications for the purpose of improving the conversion of methane to hydrogen. Conversion of methane to hydrogen was as high as 50 % although some results were as low as 2 %.

There are many recommendations/improvements that can be done for the project of plasma-assisted biogas conversion. One of the first things that needs be addresses is the improvement of repeatable conversion data using the current set-up. Secondly, the conversion rates need to be improved significantly to make the technology competitive with traditional steam reforming and other plasma-assisted dry reforming technologies. A nanosecond pulse power supply could improve the conversion rates through transferring energy more efficiently and selectively to electrons. This would compare favorably with the currently used set-up that utilizes sinusoidal excitation that have a relatively slow rise time (to reach the peak voltage). A faster rise time would allow extremely selective energization of electrons thereby enabling even higher dissociation.

## BIBLIOGRAPHY

- [1] S. Samukawa, M. Hori, S. Rauf, K. Tachibana, P. Bruggeman, G. Kroesen, J. C. Whitehead, A. B. Murphy, A. F. Gutsol, S. Starikovskaia *et al.*, “The 2012 plasma roadmap,” *Journal of Physics D: Applied Physics*, vol. 45, no. 25, p. 253001, 2012.
- [2] Y. Ju and W. Sun, “Plasma assisted combustion: Dynamics and chemistry,” *Progress in Energy and Combustion Science*, vol. 48, pp. 21–83, 2015.
- [3] I. Adamovich, S. D. Baalrud, A. Bogaerts, P. Bruggeman, M. Cappelli, V. Colombo, U. Czarnetzki, U. Ebert, J. Eden, P. Favia *et al.*, “The 2017 plasma roadmap: Low temperature plasma science and technology,” *Journal of Physics D: Applied Physics*, vol. 50, no. 32, p. 323001, 2017.
- [4] A. Fridman, *Plasma chemistry*. Cambridge university press, 2008.
- [5] G. Fridman, G. Friedman, A. Gutsol, A. B. Shekhter, V. N. Vasilets, and A. Fridman, “Applied plasma medicine,” *Plasma Processes and Polymers*, vol. 5, no. 6, pp. 503–533, 2008.
- [6] A. Schmidt-Bleker, J. Winter, A. Bösel, S. Reuter, and K.-D. Weltmann, “On the plasma chemistry of a cold atmospheric argon plasma jet with shielding gas device,” *Plasma Sources Science and Technology*, vol. 25, no. 1, p. 015005, 2015.
- [7] G. Bauer and D. B. Graves, “Mechanisms of selective antitumor action of cold atmospheric plasma-derived reactive oxygen and nitrogen species,” *Plasma Processes and Polymers*, vol. 13, no. 12, pp. 1157–1178, 2016.
- [8] M. G. Kong, G. Kroesen, G. Morfill, T. Nosenko, T. Shimizu, J. Van Dijk, and J. Zimmermann, “Plasma medicine: an introductory review,” *new Journal of Physics*, vol. 11, no. 11, p. 115012, 2009.
- [9] N. Kurake, H. Tanaka, K. Ishikawa, T. Kondo, M. Sekine, K. Nakamura, H. Kajiyama, F. Kikkawa, M. Mizuno, and M. Hori, “Cell survival of glioblastoma grown in medium containing hydrogen peroxide and/or nitrite, or in plasma-activated medium,” *Archives of biochemistry and biophysics*, vol. 605, pp. 102–108, 2016.

- [10] E. Robert, T. Darny, S. Dozias, S. Iseni, and J.-M. Pouvesle, "New insights on the propagation of pulsed atmospheric plasma streams: From single jet to multi jet arrays," *Physics of Plasmas*, vol. 22, no. 12, p. 122007, 2015.
- [11] G. Collet, E. Robert, A. Lenoir, M. Vandamme, T. Darny, S. Dozias, C. Kieda, and J. M. Pouvesle, "Plasma jet-induced tissue oxygenation: potentialities for new therapeutic strategies," *Plasma Sources Science and Technology*, vol. 23, no. 1, p. 012005, 2014.
- [12] E. A. Ratovitski, X. Cheng, D. Yan, J. H. Sherman, J. Canady, B. Trink, and M. Keidar, "Anti-cancer therapies of 21st century: novel approach to treat human cancers using cold atmospheric plasma," *Plasma Processes and Polymers*, vol. 11, no. 12, pp. 1128–1137, 2014.
- [13] V. Miller, A. Lin, and A. Fridman, "Why target immune cells for plasma treatment of cancer," *Plasma Chemistry and Plasma Processing*, vol. 36, no. 1, pp. 259–268, 2016.
- [14] H. W. Lee, S. H. Nam, A.-A. H. Mohamed, G. C. Kim, and J. K. Lee, "Atmospheric pressure plasma jet composed of three electrodes: application to tooth bleaching," *Plasma Processes and Polymers*, vol. 7, no. 3-4, pp. 274–280, 2010.
- [15] L. L. Klein and R. S. Gibbs, "Use of microbial cultures and antibiotics in the prevention of infection-associated preterm birth," *American Journal of Obstetrics & Gynecology*, vol. 190, no. 6, pp. 1493–1502, 2004.
- [16] H. W. Lee, G. J. Kim, J. M. Kim, J. K. Park, J. K. Lee, and G. C. Kim, "Tooth bleaching with nonthermal atmospheric pressure plasma," *Journal of endodontics*, vol. 35, no. 4, pp. 587–591, 2009.
- [17] I. Kieft, J. Broers, V. Caubet-Hilloutou, D. Slaaf, F. Ramaekers, and E. Stoffels, "Electric discharge plasmas influence attachment of cultured cho k1 cells," *Bioelectromagnetics*, vol. 25, no. 5, pp. 362–368, 2004.
- [18] X. Lu, Z. Jiang, Q. Xiong, Z. Tang, X. Hu, and Y. Pan, "An 11 cm long atmospheric pressure cold plasma plume for applications of plasma medicine," *Applied Physics Letters*, vol. 92, no. 8, p. 081502, 2008.
- [19] F. Iza, G. J. Kim, S. M. Lee, J. K. Lee, J. L. Walsh, Y. T. Zhang, and M. G. Kong, "Microplasmas: Sources, particle kinetics, and biomedical applications," *Plasma Processes and Polymers*, vol. 5, no. 4, pp. 322–344, 2008.
- [20] G. Park, H. Lee, G. Kim, and J. K. Lee, "Global model of he/o<sub>2</sub> and ar/o<sub>2</sub> atmospheric pressure glow discharges," *Plasma Processes and Polymers*, vol. 5, no. 6, pp. 569–576, 2008.

- [21] M. A. Bogle, K. A. Arndt, and J. S. Dover, "Evaluation of plasma skin regeneration technology in low-energy full-facial rejuvenation," *Archives of dermatology*, vol. 143, no. 2, pp. 168–174, 2007.
- [22] S. Kilmer, N. Semchyshyn, G. Shah, and R. Fitzpatrick, "A pilot study on the use of a plasma skin regeneration device (portrait® psr3) in full facial rejuvenation procedures," *Lasers in medical science*, vol. 22, no. 2, pp. 101–109, 2007.
- [23] M. L. Elsaie and J. N. Kammer, "Evaluation of plasma skin regeneration technology for cutaneous remodeling," *Journal of cosmetic dermatology*, vol. 7, no. 4, pp. 309–311, 2008.
- [24] K. W. Foster, R. L. Moy, and E. F. Fincher, "Advances in plasma skin regeneration," *Journal of cosmetic dermatology*, vol. 7, no. 3, pp. 169–179, 2008.
- [25] M. Potter, R. Harrison, A. Ramsden, P. Andrews, and D. Gault, "Facial acne and fine lines: Transforming patient outcomes with plasma skin resurfacing," *Lasers in Surgery And Medicine*, vol. 36, p. 23, 2005.
- [26] S. Kilmer, R. Fitzpatrick, E. Bernstein, and D. Brown, "Long term follow-up on the use of plasma skin regeneration (psr) in full facial rejuvenation procedures," *Lasers in Surgery and Medicine*, vol. 36, p. 8, 2005.
- [27] A. Starikovskiy and N. Aleksandrov, "Plasma-assisted ignition and combustion," *Progress in Energy and Combustion Science*, vol. 39, no. 1, pp. 61–110, 2013.
- [28] Y. Ju, W. Sun *et al.*, "Plasma assisted combustion: Progress, challenges, and opportunities," *Combustion and Flame*, vol. 162, no. 3, pp. 529–532, 2015.
- [29] S. Chu and A. Majumdar, "Opportunities and challenges for a sustainable energy future," *nature*, vol. 488, no. 7411, p. 294, 2012.
- [30] M. Christensen, A. Hultqvist, and B. Johansson, "Demonstrating the multi fuel capability of a homogeneous charge compression ignition engine with variable compression ratio," SAE Technical Paper, Tech. Rep., 1999.
- [31] X. Lu, D. Han, and Z. Huang, "Fuel design and management for the control of advanced compression-ignition combustion modes," *Progress in Energy and Combustion Science*, vol. 37, no. 6, pp. 741–783, 2011.
- [32] V. Manente, B. Johansson, and W. Cannella, "Gasoline partially premixed combustion, the future of internal combustion engines?" *International Journal of Engine Research*, vol. 12, no. 3, pp. 194–208, 2011.

- [33] R. D. Reitz, "Directions in internal combustion engine research," *Combustion and Flame*, vol. 1, no. 160, pp. 1–8, 2013.
- [34] W. Sun and Y. Ju, "Nonequilibrium plasma-assisted combustion: a review of recent progress," *J. Plasma Fusion Res*, vol. 89, no. 4, pp. 208–219, 2013.
- [35] T. C. Lieuwen and V. Yang, *Gas turbine emissions*. Cambridge university press, 2013, vol. 38.
- [36] A. H. Lefebvre and D. R. Ballal, *Gas turbine combustion: alternative fuels and emissions*. CRC press, 2010.
- [37] R. Tacina, C. Mao, and C. Wey, "Experimental investigation of a multiplex fuel injector module for low emission combustors. aiaa paper 2003-0827," 2003.
- [38] K.-Y. Hsu, L. Goss, and W. Roquemore, "Characteristics of a trapped-vortex combustor," *Journal of Propulsion and Power*, vol. 14, no. 1, pp. 57–65, 1998.
- [39] D. Schwer and K. Kailasanath, "Numerical investigation of the physics of rotating-detonation-engines," *Proceedings of the Combustion Institute*, vol. 33, no. 2, pp. 2195–2202, 2011.
- [40] I. Esakov, L. Grachev, K. Khodataev, and D. Van Wie, "Experiments on propane ignition in high-speed airflow using a deeply undercritical microwave discharge," in *42nd AIAA Aerospace Sciences Meeting and Exhibit*, 2004, p. 840.
- [41] S. Williams, S. Popovic, L. Vuskovic, C. Carter, L. Jacobson, S. Kuo, D. Bivolaru, S. Corera, M. Kahandawala, and S. Sidhu, "Model and igniter development for plasma assisted combustion," in *42nd AIAA Aerospace Sciences Meeting and Exhibit*, 2004, p. 1012.
- [42] A. Klimov, V. Bityurin, A. Kuznetsov, B. Tolkunov, N. Vystavkin, and M. Vasiliev, "External and internal plasma-assisted combustion," in *42nd AIAA Aerospace Sciences Meeting and Exhibit*, 2004, p. 1014.
- [43] V. Shibkov, V. Chernikov, A. Ershov, R. Konstantinovskij, L. Shibkova, and V. Zlobin, "Propane-butane-air mixture ignition and combustion in the aerodynamic channel with the stagnant zone," in *42nd AIAA Aerospace Sciences Meeting and Exhibit*, 2004, p. 838.
- [44] H. Do, S.-k. Im, M. A. Cappelli, and M. G. Mungal, "Plasma assisted flame ignition of supersonic flows over a flat wall," *Combustion and Flame*, vol. 157, no. 12, pp. 2298–2305, 2010.



- [45] I. Kimura, H. Aoki, and M. Kato, "The use of a plasma jet for flame stabilization and promotion of combustion in supersonic air flows," *Combustion and Flame*, vol. 42, pp. 297–305, 1981.
- [46] A. E. Rakitin and A. Y. Starikovskii, "Mechanisms of deflagration-to-detonation transition under initiation by high-voltage nanosecond discharges," *Combustion and Flame*, vol. 155, no. 1-2, pp. 343–355, 2008.
- [47] A. Starikovskiy, N. Aleksandrov, and A. Rakitin, "Plasma-assisted ignition and deflagration-to-detonation transition," *Phil. Trans. R. Soc. A*, vol. 370, no. 1960, pp. 740–773, 2012.
- [48] A.-M. Warris and F. Weinberg, "Ignition and flame stabilization by plasma jets in fast gas streams," in *Symposium (International) on Combustion*, vol. 20, no. 1. Elsevier, 1985, pp. 1825–1831.
- [49] I. Matveev, S. Matveeva, and A. Gutsol, "Non-equilibrium plasma igniters and pilots for aerospace application," in *43rd AIAA Aerospace Sciences Meeting and Exhibit*, 2005, p. 1191.
- [50] B. Ganguly, "Hydrocarbon combustion enhancement by applied electric field and plasma kinetics," *Plasma Physics and Controlled Fusion*, vol. 49, no. 12B, p. B239, 2007.
- [51] G. Pilla, D. Galley, D. A. Lacoste, F. Lacas, D. Veynante, and C. O. Laux, "Stabilization of a turbulent premixed flame using a nanosecond repetitively pulsed plasma," *IEEE Transactions on Plasma Science*, vol. 34, no. 6, pp. 2471–2477, 2006.
- [52] F. Wang, J. Liu, J. Sinibaldi, C. Brophy, A. Kuthi, C. Jiang, P. Ronney, and M. A. Gundersen, "Transient plasma ignition of quiescent and flowing air/fuel mixtures," *IEEE Transactions on Plasma Science*, vol. 33, no. 2, pp. 844–849, 2005.
- [53] B. Wolk, A. DeFilippo, J.-Y. Chen, R. Dibble, A. Nishiyama, and Y. Ikeda, "Enhancement of flame development by microwave-assisted spark ignition in constant volume combustion chamber," *Combustion and flame*, vol. 160, no. 7, pp. 1225–1234, 2013.
- [54] L. F. Spencer and A. D. Gallimore, "Efficiency of co 2 dissociation in a radio-frequency discharge," *Plasma Chemistry and Plasma Processing*, vol. 31, no. 1, pp. 79–89, 2011.
- [55] A. Czernichowski, "Gliding arc: applications to engineering and environment control," *Pure and Applied Chemistry*, vol. 66, no. 6, pp. 1301–1310, 1994.

- [56] H. F. BEHBAHANI, A.-M. WARRIS, and F. J. WEINBERG, "The destruction of nitric oxide by nitrogen atoms from plasma jets: designing for thermal stratification," *Combustion Science and Technology*, vol. 30, no. 1-6, pp. 289–302, 1983.
- [57] J. Niu, X. Yang, A. Zhu, L. Shi, Q. Sun, Y. Xu, and C. Shi, "Plasma-assisted selective catalytic reduction of nox by c2h2 over co-hzsm-5 catalyst," *Catalysis Communications*, vol. 7, no. 5, pp. 297–301, 2006.
- [58] A. Khacef, J. M. Cormier, and J. M. Pouvesle, "Nox remediation in oxygen-rich exhaust gas using atmospheric pressure non-thermal plasma generated by a pulsed nanosecond dielectric barrier discharge," *Journal of Physics D: Applied Physics*, vol. 35, no. 13, p. 1491, 2002.
- [59] S. Brethes-Dupouey, R. Peyrous, and B. Held, "Removal of h<sub>2</sub>s in air by using gliding discharges," *The European Physical Journal-Applied Physics*, vol. 11, no. 1, pp. 43–58, 2000.
- [60] L. Yu, X. Tu, X. Li, Y. Wang, Y. Chi, and J. Yan, "Destruction of acenaphthene, fluorene, anthracene and pyrene by a dc gliding arc plasma reactor," *Journal of Hazardous Materials*, vol. 180, no. 1-3, pp. 449–455, 2010.
- [61] M. Cha, S. Lee, K. Kim, and S. Chung, "Soot suppression by nonthermal plasma in coflow jet diffusion flames using a dielectric barrier discharge," *Combustion and flame*, vol. 141, no. 4, pp. 438–447, 2005.
- [62] N. R. Council, P. S. Committee, P. . Committee *et al.*, *Plasma science: advancing knowledge in the national interest*. National Academies Press, 2008, vol. 3.
- [63] P. K. Chu, S. Qin, C. Chan, N. W. Cheung, and L. A. Larson, "Plasma immersion ion implantation? a fledgling technique for semiconductor processing," *Materials Science and Engineering: R: Reports*, vol. 17, no. 6-7, pp. 207–280, 1996.
- [64] N. Cheung, "Plasma immersion ion implantation for semiconductor processing," *Materials chemistry and physics*, vol. 46, no. 2-3, pp. 132–139, 1996.
- [65] J. W. Coburn and H. F. Winters, "Plasma etching? a discussion of mechanisms," *Journal of vacuum Science and Technology*, vol. 16, no. 2, pp. 391–403, 1979.
- [66] C. Mogab, A. Adams, and D. L. Flamm, "Plasma etching of si and sio<sub>2</sub>? the effect of oxygen additions to cf<sub>4</sub> plasmas," *Journal of applied physics*, vol. 49, no. 7, pp. 3796–3803, 1978.

- [67] S. Tachi, K. Tsujimoto, and S. Okudaira, “Low-temperature reactive ion etching and microwave plasma etching of silicon,” *Applied physics letters*, vol. 52, no. 8, pp. 616–618, 1988.
- [68] C. Cardinaud, M.-C. Peignon, and P.-Y. Tessier, “Plasma etching: principles, mechanisms, application to micro-and nano-technologies,” *Applied Surface Science*, vol. 164, no. 1-4, pp. 72–83, 2000.
- [69] M. A. Lieberman and A. J. Lichtenberg, *Principles of plasma discharges and materials processing*. John Wiley & Sons, 2005.
- [70] H. Abe, M. Yoneda, and N. Fujiwara, “Developments of plasma etching technology for fabricating semiconductor devices,” *Japanese Journal of Applied Physics*, vol. 47, no. 3R, p. 1435, 2008.
- [71] Y. Wu, P. Qiao, T. Chong, and Z. Shen, “Carbon nanowalls grown by microwave plasma enhanced chemical vapor deposition,” *Advanced materials*, vol. 14, no. 1, pp. 64–67, 2002.
- [72] S. Hofmann, C. Ducati, J. Robertson, and B. Kleinsorge, “Low-temperature growth of carbon nanotubes by plasma-enhanced chemical vapor deposition,” *Applied Physics Letters*, vol. 83, no. 1, pp. 135–137, 2003.
- [73] T.-o. Terasawa and K. Saiki, “Growth of graphene on cu by plasma enhanced chemical vapor deposition,” *Carbon*, vol. 50, no. 3, pp. 869–874, 2012.
- [74] A. Agarwal and M. J. Kushner, “Plasma atomic layer etching using conventional plasma equipment,” *Journal of Vacuum Science & Technology A: Vacuum, Surfaces, and Films*, vol. 27, no. 1, pp. 37–50, 2009.
- [75] D. Metzler, R. L. Bruce, S. Engelmann, E. A. Joseph, and G. S. Oehrlein, “Fluorocarbon assisted atomic layer etching of sio<sub>2</sub> using cyclic ar/c<sub>4</sub>f<sub>8</sub> plasma,” *Journal of Vacuum Science & Technology A: Vacuum, Surfaces, and Films*, vol. 32, no. 2, p. 020603, 2014.
- [76] F. D. Egitto and L. J. Matienzo, “Plasma modification of polymer surfaces for adhesion improvement,” *IBM Journal of Research and Development*, vol. 38, no. 4, pp. 423–439, 1994.
- [77] G. Borcia, C. Anderson, and N. Brown, “Dielectric barrier discharge for surface treatment: application to selected polymers in film and fibre form,” *Plasma Sources Science and Technology*, vol. 12, no. 3, p. 335, 2003.

- [78] M. Shenton, M. Lovell-Hoare, and G. Stevens, "Adhesion enhancement of polymer surfaces by atmospheric plasma treatment," *Journal of Physics D: Applied Physics*, vol. 34, no. 18, p. 2754, 2001.
- [79] E. Liston, L. Martinu, and M. Wertheimer, "Plasma surface modification of polymers for improved adhesion: a critical review," *Journal of adhesion science and technology*, vol. 7, no. 10, pp. 1091–1127, 1993.
- [80] S. Guruvenket, G. M. Rao, M. Komath, and A. M. Raichur, "Plasma surface modification of polystyrene and polyethylene," *Applied Surface Science*, vol. 236, no. 1-4, pp. 278–284, 2004.
- [81] G. Wu, P. Li, H. Feng, X. Zhang, and P. K. Chu, "Engineering and functionalization of biomaterials via surface modification," *Journal of Materials Chemistry B*, vol. 3, no. 10, pp. 2024–2042, 2015.
- [82] D. S. Syromotina, R. A. Surmenev, M. A. Surmeneva, A. Boyandin, E. Nikolaeva, O. Prymak, M. Epple, M. Ulbricht, C. Oehr, and T. Volova, "Surface wettability and energy effects on the biological performance of poly-3-hydroxybutyrate films treated with rf plasma," *Materials Science and Engineering: C*, vol. 62, pp. 450–457, 2016.
- [83] N. Inagaki, *Plasma surface modification and plasma polymerization*. CRC Press, 2014.
- [84] T. Zhou, Y. Zhu, X. Li, X. Liu, K. W. Yeung, S. Wu, X. Wang, Z. Cui, X. Yang, and P. K. Chu, "Surface functionalization of biomaterials by radical polymerization," *Progress in Materials Science*, vol. 83, pp. 191–235, 2016.
- [85] M. Lorenzetti, I. Doga, T. Stoicki, D. Stopar, M. Kalin, S. Kobe, and S. Novak, "The influence of surface modification on bacterial adhesion to titanium-based substrates," *ACS applied materials & interfaces*, vol. 7, no. 3, pp. 1644–1651, 2015.
- [86] K. Bazaka, M. Jacob, W. Chrzanowski, and K. Ostrikov, "Anti-bacterial surfaces: natural agents, mechanisms of action, and plasma surface modification," *Rsc Advances*, vol. 5, no. 60, pp. 48 739–48 759, 2015.
- [87] V. Kochkodan and N. Hilal, "A comprehensive review on surface modified polymer membranes for biofouling mitigation," *Desalination*, vol. 356, pp. 187–207, 2015.
- [88] C. Oehr, "Plasma surface modification of polymers for biomedical use," *Nuclear Instruments and Methods in Physics Research Section B: Beam Interactions with Materials and Atoms*, vol. 208, pp. 40–47, 2003.

- [89] X. Ren, Y. Feng, J. Guo, H. Wang, Q. Li, J. Yang, X. Hao, J. Lv, N. Ma, and W. Li, "Surface modification and endothelialization of biomaterials as potential scaffolds for vascular tissue engineering applications," *Chemical Society Reviews*, vol. 44, no. 15, pp. 5680–5742, 2015.
- [90] S. Surucu, K. Masur, H. T. Sasmazel, T. Von Woedtke, and K. D. Weltmann, "Atmospheric plasma surface modifications of electrospun pcl/chitosan/pcl hybrid scaffolds by nozzle type plasma jets for usage of cell cultivation," *Applied Surface Science*, vol. 385, pp. 400–409, 2016.
- [91] R. D. Ambashta and M. Sillanpää, "Water purification using magnetic assistance: a review," *Journal of hazardous materials*, vol. 180, no. 1-3, pp. 38–49, 2010.
- [92] G. M. Geise, H.-S. Lee, D. J. Miller, B. D. Freeman, J. E. McGrath, and D. R. Paul, "Water purification by membranes: the role of polymer science," *Journal of Polymer Science Part B: Polymer Physics*, vol. 48, no. 15, pp. 1685–1718, 2010.
- [93] N. Savage and M. S. Diallo, "Nanomaterials and water purification: opportunities and challenges," *Journal of Nanoparticle research*, vol. 7, no. 4-5, pp. 331–342, 2005.
- [94] A. Mills, R. H. Davies, and D. Worsley, "Water purification by semiconductor photocatalysis," *Chemical Society Reviews*, vol. 22, no. 6, pp. 417–425, 1993.
- [95] J. Foster, B. S. Sommers, S. N. Gucker, I. M. Blankson, and G. Adamovsky, "Perspectives on the interaction of plasmas with liquid water for water purification," *IEEE Transactions on Plasma Science*, vol. 40, no. 5, pp. 1311–1323, 2012.
- [96] W. H. Glaze, J.-W. Kang, and D. H. Chapin, "The chemistry of water treatment processes involving ozone, hydrogen peroxide and ultraviolet radiation," *Ozone: Science & Engineering*, 1987.
- [97] R. Munter, "Advanced oxidation processes—current status and prospects," *Proc. Estonian Acad. Sci. Chem*, vol. 50, no. 2, pp. 59–80, 2001.
- [98] A. Stasinakis, "Use of selected advanced oxidation processes (aops) for wastewater treatment? a mini review," *Global NEST journal*, vol. 10, no. 3, pp. 376–385, 2008.
- [99] S. Parsons, *Advanced oxidation processes for water and wastewater treatment*. IWA publishing, 2004.

- [100] P. Gerland, A. E. Raftery, H. Ševčíková, N. Li, D. Gu, T. Spoorenberg, L. Alkema, B. K. Fosdick, J. Chunn, N. Lalic *et al.*, “World population stabilization unlikely this century,” *Science*, vol. 346, no. 6206, pp. 234–237, 2014.
- [101] L. A. Valdez-Aguilar and D. W. Reed, “Response of selected greenhouse ornamental plants to alkalinity in irrigation water,” *Journal of plant nutrition*, vol. 30, no. 3, pp. 441–452, 2007.
- [102] C. Simsek and O. Gunduz, “Iwq index: a gis-integrated technique to assess irrigation water quality,” *Environmental Monitoring and Assessment*, vol. 128, no. 1-3, pp. 277–300, 2007.
- [103] B. J. Zebarth, T. A. Forge, C. Goyer, and L. D. Brin, “Effect of soil acidification on nitrification in soil,” *Canadian Journal of Soil Science*, vol. 95, no. 4, pp. 359–363, 2015.
- [104] H. Enoch and J. M. Olesen, “Plant response to irrigation with water enriched with carbon dioxide,” *New Phytologist*, vol. 125, no. 2, pp. 249–258, 1993.
- [105] J. Bogatin, N. P. Bondarenko, E. Z. Gak, E. E. Rokhinson, and I. P. Ananyev, “Magnetic treatment of irrigation water: experimental results and application conditions,” *Environmental science & technology*, vol. 33, no. 8, pp. 1280–1285, 1999.
- [106] B. L. Maheshwari and H. S. Grewal, “Magnetic treatment of irrigation water: Its effects on vegetable crop yield and water productivity,” *Agricultural water management*, vol. 96, no. 8, pp. 1229–1236, 2009.
- [107] N. Misra, O. Schlüter, and P. J. Cullen, *Cold plasma in food and agriculture: fundamentals and applications*. Academic Press, 2016.
- [108] M. Ito, T. Ohta, and M. Hori, “Plasma agriculture,” *Journal of the Korean Physical Society*, vol. 60, no. 6, pp. 937–943, 2012.
- [109] J. C. Volin, F. S. Denes, R. A. Young, and S. M. Park, “Modification of seed germination performance through cold plasma chemistry technology,” *Crop Science*, vol. 40, no. 6, pp. 1706–1718, 2000.
- [110] H. Hashizume, T. Ohta, J. Fengdong, K. Takeda, K. Ishikawa, M. Hori, and M. Ito, “Inactivation effects of neutral reactive-oxygen species on penicillium digitatum spores using non-equilibrium atmospheric-pressure oxygen radical source,” *Applied Physics Letters*, vol. 103, no. 15, p. 153708, 2013.

- [111] S. C. Min, S. H. Roh, B. A. Niemira, J. E. Sites, G. Boyd, and A. Lacombe, "Dielectric barrier discharge atmospheric cold plasma inhibits escherichia coli o157: H7, salmonella, listeria monocytogenes, and tulane virus in romaine lettuce," *International journal of food microbiology*, vol. 237, pp. 114–120, 2016.
- [112] S. Kitazaki, K. Koga, M. Shiratani, and N. Hayashi, "Growth enhancement of radish sprouts induced by low pressure o2 radio frequency discharge plasma irradiation," *Japanese Journal of Applied Physics*, vol. 51, no. 1S, p. 01AE01, 2012.
- [113] S. Sasaki, M. Kanzaki, and T. Kaneko, "Highly efficient and minimally invasive transfection using time-controlled irradiation of atmospheric-pressure plasma," *Applied Physics Express*, vol. 7, no. 2, p. 026202, 2014.
- [114] B. Locke, M. Sato, P. Sunka, M. Hoffmann, and J.-S. Chang, "Electrohydraulic discharge and nonthermal plasma for water treatment," *Industrial & engineering chemistry research*, vol. 45, no. 3, pp. 882–905, 2006.
- [115] Y. Yang, H. Kim, A. Starikovskiy, A. Fridman, and Y. I. Cho, "Application of pulsed spark discharge for calcium carbonate precipitation in hard water," *Water research*, vol. 44, no. 12, pp. 3659–3668, 2010.
- [116] X. Wang, M. Zhou, and X. Jin, "Application of glow discharge plasma for wastewater treatment," *Electrochimica Acta*, vol. 83, pp. 501–512, 2012.
- [117] S. N. Gucker, J. E. Foster, and M. C. Garcia, "An investigation of an underwater steam plasma discharge as alternative to air plasmas for water purification," *Plasma Sources Science and Technology*, vol. 24, no. 5, p. 055005, 2015.
- [118] J. E. Foster, B. Weatherford, E. Gillman, and B. Yee, "Underwater operation of a dbd plasma jet," *Plasma Sources Science and Technology*, vol. 19, no. 2, p. 025001, 2010.
- [119] B. Sommers and J. Foster, "Plasma formation in underwater gas bubbles," *Plasma Sources Science and Technology*, vol. 23, no. 1, p. 015020, 2014.
- [120] P. Bruggeman, M. J. Kushner, B. R. Locke, J. G. Gardeniers, W. Graham, D. B. Graves, R. Hofman-Caris, D. Maric, J. P. Reid, E. Ceriani *et al.*, "Plasma–liquid interactions: a review and roadmap," *Plasma sources science and technology*, vol. 25, no. 5, p. 053002, 2016.

- [121] B. Eliasson and U. Kogelschatz, "Modeling and applications of silent discharge plasmas," *IEEE transactions on plasma science*, vol. 19, no. 2, pp. 309–323, 1991.
- [122] J.-S. Chang, P. A. Lawless, and T. Yamamoto, "Corona discharge processes," *IEEE Transactions on plasma science*, vol. 19, no. 6, pp. 1152–1166, 1991.
- [123] U. Pschl and M. Shiraiwa, "Multiphase chemistry at the atmosphere–biosphere interface influencing climate and public health in the anthropocene," *Chemical reviews*, vol. 115, no. 10, pp. 4440–4475, 2015.
- [124] J. H. Seinfeld and S. N. Pandis, *Atmospheric chemistry and physics: from air pollution to climate change*. John Wiley & Sons, 2016.
- [125] A. W. Adamson, A. P. Gast *et al.*, *Physical chemistry of surfaces*. Interscience publishers New York, 1967.
- [126] V. P. Carey, "Liquid–vapor phase-change phenomena: An introduction to the thermodynamics of vaporization and condensation processes in heat transfer equipments," 1992.
- [127] J. M. Prausnitz, R. N. Lichtenthaler, and E. G. de Azevedo, *Molecular thermodynamics of fluid-phase equilibria*. Pearson Education, 1998.
- [128] W. M. Deen, *Analysis of transport phenomena*. Oxford University Press New York, 1998.
- [129] S. R. De Groot and P. Mazur, *Non-equilibrium thermodynamics*. Courier Corporation, 2013.
- [130] B. C. Garrett, G. K. Schenter, and A. Morita, "Molecular simulations of the transport of molecules across the liquid/vapor interface of water," *Chemical reviews*, vol. 106, no. 4, pp. 1355–1374, 2006.
- [131] K. Scherzer, "Introduction to molecular dynamics and chemical kinetics," *Zeitschrift für Physikalische Chemie*, vol. 203, no. 1-2, pp. 247–247, 1998.
- [132] V. I. Parvulescu, *Catalysts Used in Plasma-Assisted Catalytic Processes: Preparation, Activation, and Regeneration*. Wiley Online Library, 2012.
- [133] F. Aziz and M. Rodgers, *Radiation chemistry; principles and applications*. Atomic Energy Organization of Iran, 1994.
- [134] G. Hagelaar and L. Pitchford, "Solving the boltzmann equation to obtain electron transport coefficients and rate coefficients for fluid models," *Plasma Sources Science and Technology*, vol. 14, no. 4, p. 722, 2005.



- [135] B. R. Locke and S. M. Thagard, “Analysis and review of chemical reactions and transport processes in pulsed electrical discharge plasma formed directly in liquid water,” *Plasma Chemistry and Plasma Processing*, vol. 32, no. 5, pp. 875–917, 2012.
- [136] J. Gao, X. Wang, Z. Hu, H. Deng, J. Hou, X. Lu, and J. Kang, “Plasma degradation of dyes in water with contact glow discharge electrolysis,” *Water research*, vol. 37, no. 2, pp. 267–272, 2003.
- [137] A. Günther, S. A. Khan, M. Thalmann, F. Trachsel, and K. F. Jensen, “Transport and reaction in microscale segmented gas–liquid flow,” *Lab on a Chip*, vol. 4, no. 4, pp. 278–286, 2004.
- [138] S. A. Norberg, W. Tian, E. Johnsen, and M. J. Kushner, “Atmospheric pressure plasma jets interacting with liquid covered tissue: touching and not-touching the liquid,” *Journal of Physics D: Applied Physics*, vol. 47, no. 47, p. 475203, 2014.
- [139] W. Tian and M. J. Kushner, “Atmospheric pressure dielectric barrier discharges interacting with liquid covered tissue,” *Journal of Physics D: Applied Physics*, vol. 47, no. 16, p. 165201, 2014.
- [140] C. Chen, D. Liu, Z. Liu, A. Yang, H. Chen, G. Shama, and M. Kong, “A model of plasma-biofilm and plasma-tissue interactions at ambient pressure,” *Plasma Chemistry and Plasma Processing*, vol. 34, no. 3, pp. 403–441, 2014.
- [141] A. Lindsay, C. Anderson, E. Slikboer, S. Shannon, and D. Graves, “Momentum, heat, and neutral mass transport in convective atmospheric pressure plasma-liquid systems and implications for aqueous targets,” *Journal of Physics D: Applied Physics*, vol. 48, no. 42, p. 424007, 2015.
- [142] D. Iya-Sou, S. Laminsi, S. Cavadias, and S. Ognier, “Removal of model pollutants in aqueous solution by gliding arc discharge: determination of removal mechanisms. part i: experimental study,” *Plasma Chemistry and Plasma Processing*, vol. 33, no. 1, pp. 97–113, 2013.
- [143] I.-S. Djakaou, R. M. Ghezzar, M. E.-M. Zekri, F. Abdelmalek, S. Cavadias, and S. Ognier, “Removal of model pollutants in aqueous solution by gliding arc discharge. part ii: modeling and simulation study,” *Plasma Chemistry and Plasma Processing*, vol. 35, no. 1, pp. 143–157, 2015.
- [144] L. L. Alves, A. Bogaerts, V. Guerra, and M. M. Turner, “Foundations of modelling of nonequilibrium low-temperature plasmas,” *Plasma Sources Science and Technology*, 2018.

- [145] D. Levko, A. Sharma, and L. L. Raja, “Kinetic modeling of streamer penetration into de-ionized water,” *Physics of Plasmas*, vol. 25, no. 3, p. 033515, 2018.
- [146] A. Haryanto, S. Fernando, N. Murali, and S. Adhikari, “Current status of hydrogen production techniques by steam reforming of ethanol: a review,” *Energy & Fuels*, vol. 19, no. 5, pp. 2098–2106, 2005.
- [147] L. Barelli, G. Bidini, F. Gallorini, and S. Servili, “Hydrogen production through sorption-enhanced steam methane reforming and membrane technology: a review,” *Energy*, vol. 33, no. 4, pp. 554–570, 2008.
- [148] J. R. Rostrup-Nielsen, “Catalytic steam reforming,” in *Catalysis*. Springer, 1984, pp. 1–117.
- [149] J. Sehested, “Four challenges for nickel steam-reforming catalysts,” *Catalysis Today*, vol. 111, no. 1-2, pp. 103–110, 2006.
- [150] F. Besenbacher, I. Chorkendorff, B. Clausen, B. Hammer, A. Molenbroek, J. K. Nørskov, and I. Stensgaard, “Design of a surface alloy catalyst for steam reforming,” *Science*, vol. 279, no. 5358, pp. 1913–1915, 1998.
- [151] J. M. Ogden, “Prospects for building a hydrogen energy infrastructure,” *Annual Review of Energy and the Environment*, vol. 24, no. 1, pp. 227–279, 1999.
- [152] P. L. Spath and M. K. Mann, “Life cycle assessment of hydrogen production via natural gas steam reforming,” National Renewable Energy Lab., Golden, CO (US), Tech. Rep., 2000.
- [153] H. F. Sheet, “Hydrogen production—steam methane reforming (smr),” *New York State Energy Research and Development Authority*, New York, 2005.
- [154] Q. Wang, B.-H. Yan, Y. Jin, and Y. Cheng, “Dry reforming of methane in a dielectric barrier discharge reactor with ni/al<sub>2</sub>o<sub>3</sub> catalyst: interaction of catalyst and plasma,” *Energy & Fuels*, vol. 23, no. 8, pp. 4196–4201, 2009.
- [155] Y.-p. Zhang, Y. Li, Y. Wang, C.-j. Liu, and B. Eliasson, “Plasma methane conversion in the presence of carbon dioxide using dielectric-barrier discharges,” *Fuel Processing Technology*, vol. 83, no. 1-3, pp. 101–109, 2003.
- [156] C.-J. Liu, B. Xue, B. Eliasson, F. He, Y. Li, and G.-H. Xu, “Methane conversion to higher hydrocarbons in the presence of carbon dioxide using dielectric-barrier discharge plasmas,” *Plasma Chemistry and Plasma Processing*, vol. 21, no. 3, pp. 301–310, 2001.

- [157] D. Czyłkowski, B. Hrycak, M. Jasiński, M. Dors, and J. Mizeraczyk, "Microwave plasma-based method of hydrogen production via combined steam reforming of methane," *Energy*, vol. 113, pp. 653–661, 2016.
- [158] C.-H. Tsai, T.-H. Hsieh, M. Shih, Y.-J. Huang, and T.-C. Wei, "Partial oxidation of methane to synthesis gas by a microwave plasma torch," *AIChE journal*, vol. 51, no. 10, pp. 2853–2858, 2005.
- [159] Y.-F. Wang, C.-H. Tsai, W.-Y. Chang, and Y.-M. Kuo, "Methane steam reforming for producing hydrogen in an atmospheric-pressure microwave plasma reactor," *international journal of hydrogen energy*, vol. 35, no. 1, pp. 135–140, 2010.
- [160] Y. N. Chun, Y. C. Yang, and K. Yoshikawa, "Hydrogen generation from biogas reforming using a gliding arc plasma-catalyst reformer," *Catalysis today*, vol. 148, no. 3-4, pp. 283–289, 2009.
- [161] X. Tu and J. C. Whitehead, "Plasma dry reforming of methane in an atmospheric pressure ac gliding arc discharge: Co-generation of syngas and carbon nanomaterials," *international journal of hydrogen energy*, vol. 39, no. 18, pp. 9658–9669, 2014.
- [162] N. Rueangjitt, T. Sreethawong, S. Chavadej, and H. Sekiguchi, "Plasma-catalytic reforming of methane in ac microsized gliding arc discharge: effects of input power, reactor thickness, and catalyst existence," *Chemical Engineering Journal*, vol. 155, no. 3, pp. 874–880, 2009.
- [163] C. De Bie, T. Martens, J. van Dijk, S. Paulussen, B. Verheyde, S. Corthals, and A. Bogaerts, "Dielectric barrier discharges used for the conversion of greenhouse gases: modeling the plasma chemistry by fluid simulations," *Plasma Sources Science and Technology*, vol. 20, no. 2, p. 024008, 2011.
- [164] X. Tu and J. Whitehead, "Plasma-catalytic dry reforming of methane in an atmospheric dielectric barrier discharge: Understanding the synergistic effect at low temperature," *Applied Catalysis B: Environmental*, vol. 125, pp. 439–448, 2012.
- [165] X. Tu, H. J. Gallon, M. V. Twigg, P. A. Gorry, and J. C. Whitehead, "Dry reforming of methane over a ni/al<sub>2</sub>o<sub>3</sub> catalyst in a coaxial dielectric barrier discharge reactor," *Journal of Physics D: Applied Physics*, vol. 44, no. 27, p. 274007, 2011.
- [166] T. Nunnally, K. Gutsol, A. Rabinovich, A. Fridman, A. Gutsol, and A. Kermoun, "Dissociation of co<sub>2</sub> in a low current gliding arc plasmatron," *Journal of Physics D: Applied Physics*, vol. 44, no. 27, p. 274009, 2011.

- [167] A. Indarto, D. R. Yang, J.-W. Choi, H. Lee, and H. K. Song, "Gliding arc plasma processing of co2 conversion," *Journal of hazardous materials*, vol. 146, no. 1-2, pp. 309–315, 2007.
- [168] Y.-C. Yang, B.-J. Lee, and Y.-N. Chun, "Characteristics of methane reforming using gliding arc reactor," *Energy*, vol. 34, no. 2, pp. 172–177, 2009.
- [169] R. Asisov, A. Vakar, A. Gutsol, V. Givotov, E. Krashenninnikov, M. Krotov, V. Rusanov, A. Fridman, and G. Sholin, "Plasmachemical methods of energy carrier production," *International journal of hydrogen energy*, vol. 10, no. 7-8, pp. 475–477, 1985.
- [170] S. Sun, H. Wang, D. Mei, X. Tu, and A. Bogaerts, "Co2 conversion in a gliding arc plasma: Performance improvement based on chemical reaction modeling," *Journal of CO2 Utilization*, vol. 17, pp. 220–234, 2017.
- [171] A. P. Goede, W. A. Bongers, M. F. Graswinckel, R. M. van de Sanden, M. Leins, J. Kopecki, A. Schulz, and M. Walker, "Production of solar fuels by co2 plasmolysis," in *EPJ Web of Conferences*, vol. 79. EDP Sciences, 2014, p. 01005.
- [172] H. L. Chen, H. M. Lee, S. H. Chen, Y. Chao, and M. B. Chang, "Review of plasma catalysis on hydrocarbon reforming for hydrogen production?interaction, integration, and prospects," *Applied Catalysis B: Environmental*, vol. 85, no. 1-2, pp. 1–9, 2008.
- [173] R. Aerts, W. Somers, and A. Bogaerts, "Carbon dioxide splitting in a dielectric barrier discharge plasma: a combined experimental and computational study," *ChemSusChem*, vol. 8, no. 4, pp. 702–716, 2015.
- [174] X.-J. Shao, N. Jiang, G.-J. Zhang, and Z.-x. Cao, "Comparative study on the atmospheric pressure plasma jets of helium and argon," *Applied Physics Letters*, vol. 101, no. 25, p. 253509, 2012.
- [175] Y. S. Seo, A.-A. H. Mohamed, K. C. Woo, H. W. Lee, J. K. Lee, and K. T. Kim, "Comparative studies of atmospheric pressure plasma characteristics between he and ar working gases for sterilization," *IEEE transactions on plasma science*, vol. 38, no. 10, pp. 2954–2962, 2010.

## APPENDIX A

### MATLAB CODES

## A.1 Primary Codes

```
1 %% pH vs Va
2
3
4 clc
5 clear
6 close all
7
8
9 C_HNO3 = [.5*10^-3 2.1462e-05];%8.12831E-05; % HNO3 ...
    Concentration[Moles/Liters]
10 Va = 0:.025:.250; % [Liters]
11
12 Mass_NaHCO3 = [10.0 0.0]/1000;
13 MM = 84.007; % Molar Mass of NaHCO3
14 C_NaHCO3 = Mass_NaHCO3./MM;
15
16 pH = zeros(1,length(Va));
17 i = 0;
18 j = 0;
19 for j = 1:length(C_HNO3)
20     for i = 1:length(Va)
21
22         pH(j,i) = pH_curves(C_HNO3(j),Va(i));
23
24     end
25 end
26
27 Va_1 = 0:0.025:0.125;
28 Va_2 = 0:0.025:0.125;
29 Va_3 = 0:0.025:0.250; % [Liters]
30 Va_4 = 0:0.025:0.150;
31 Va_5 = 0:0.025:0.100;
32 Va_6 = 0:0.025:0.250;
33 %
34 pH_24 = [8.16 8.25 8.16 8.05 7.95 7.89];
35 pH_26 = [8.28 8.27 8.18 8.11 8 7.93];
36 pH_29 = [8.33 8.38 8.4 8.41 8.41 8.4 8.37 8.37 8.36 8.35 8.32];
37 pH_30 = [7.62 7.62 7.59 7.57 7.54 7.52 7.5];
38 pH_31 = [7.59 7.59 7.56 7.53 7.5]; % FIJI water
39 pH_33 = [8.188333333 8.073333333 8.016666667 7.941666667 7.875 ...
    7.803333333 7.74 7.686666667 7.636666667 7.596666667 7.53];
40
41
42
43 % plot (Va,pH)
44 hold on
45 %plot (Va_1,pH_24)
46 %plot (Va_2,pH_26)
47 %plot (Va_3,pH_29)
48 %plot (Va_4,pH_30)
49 %plot (Va_5,pH_31)
50 plot (Va_6,pH_33)
51 for i = 1:length(C_HNO3)
```

```

52 hold on
53 plot(Va,pH(i,:))
54 end
55 xlabel('Va (Liters)')
56 ylabel('pH')

```

```

1 function [ pH ] = pH_curves(C_HNO3,Va)
2 %UNTITLED3 Summary of this function goes here
3 % NaHCO3 + HNO3 Reaction, Finding [H+]
4
5 Kw = 1*10^-14;
6 Ka1 = 4.46*10^-7; % [HCO3-][H+]/[H2CO3]
7 Ka2 = 4.69*10^-11; % [CO32-][H+]/[HCO3]
8 Ka = 27.29; % [NO3-][H+]/[HNO3]
9
10 Vb = 0.250; % [Liters]
11 % M_NaHCO3 = 1; [grams]
12
13 C_HCO3 = 10^-3; % NAHCO3 Concentration [Moles/Liters]
14
15
16 V_t = Va + Vb;
17 C1 = C_HCO3 * Vb/V_t;
18 C2 = C_HNO3 * Va/V_t;
19
20
21 F_1 = @(x) 1e14*((10.^(-x)).^2 - ...
    ((C1.*Ka1.*((10.^(-x)).^2))./((10.^(-x)).^2) + ...
    Ka1.*(10.^(-x)) + Ka1.*Ka2)).*(1+2.*Ka2./(10.^(-x)))) - ...
    (10.^(-x)).*(C2-C1) - Kw);
22
23 x0 = 1.0e-3;
24
25 options = optimset('Display', ...
    'iter','MaxFunEvals',100000,'MaxIter',15000);
26 pH = fsolve(F_1, x0, options);
27
28
29 end

```

```

1 %% pH vs Va
2
3
4 clc
5 clear
6 close all
7
8 MM = 84.007; % Molar Mass of NaHCO3
9 Mass_NaHCO3 = [10]/1000; % HNO3 Concentration[Moles]
10 C_NaHCO3_mol = Mass_NaHCO3./MM;
11 pH_in_HNO3 = [4.668333333];
12 % pH_in_HNO3 = [4.46 4.44 4.92 6.55 4.84 4.92 4.43];
13 C_HNO3 = 10.^(-pH_in_HNO3);

```

```

14 pH_in_H2O = [6.928333333];
15 % pH_in_H2O = [7.11 6.95 7.01 6.83 7.06 7.30 6.14];
16 Kw = (10.^(-pH_in_H2O)).^2;
17 Ka1 = 4.46*10^-7; % [HCO3-][H+]/[H2CO3]
18 Ka2 = 4.69*10^-11; % [CO32-][H+]/[HCO3]
19
20 %Vb = [125 125 250 250 100 25]/1000;
21 Vb = [250]/1000;
22 C_NaHCO3 = C_NaHCO3_mol./Vb;
23
24 Va = 0:0.025:0.250;
25 % Va_1 = 0:0.025:0.125;
26 % Va_2 = 0:0.025:0.125;
27 Va_3 = 0:0.0025:0.250; % [Liters]
28 % Va_4 = 0:0.025:0.250;
29 % Va_5 = 0:0.025:0.100;
30 % Va_6 = 0:0.025:0.250;
31
32
33
34 % pH_1 = zeros(length(C_NaHCO3),length(Va_1));
35 % pH_2 = zeros(length(C_NaHCO3),length(Va_2));
36 pH_3 = zeros(length(C_NaHCO3),length(Va_3));
37 Alk = zeros(length(C_NaHCO3),length(Va_3));
38 % pH_4 = zeros(length(C_NaHCO3),length(Va_4));
39 % pH_5 = zeros(length(C_NaHCO3),length(Va_5));
40 % pH_6 = zeros(length(C_NaHCO3),length(Va_6));
41
42 i = 0;
43 j = 0;
44 for j = 1:length(C_NaHCO3)
45     for i = 1:length(Va_3)
46
47         pH_3(j,i) = ...
            pH_curve_fit(C_NaHCO3(j),C_HNO3(j),Va_3(i),Vb(j),Kw(j));
48 %         H_plus = 10.^(-pH_3(j,i));
49 %         HCO3 = ...
            C_NaHCO3(j)*((H_plus*Ka1)/(H_plus^2+H_plus*Ka1+Ka1*Ka2));
50 %         CO3 = (HCO3*Ka2)/H_plus;
51 %         OH = Kw(j)/H_plus;
52 %         Alk(j,i) = HCO3 + 2*CO3 + OH + H_plus;
53     end
54 end
55
56 pH = [8.188333333 8.073333333 8.016666667 7.941666667 7.875 ...
        7.803333333 7.74 7.686666667 7.636666667 7.596666667 7.53];
57
58 % pH_35 = [8.12 7.97 7.91 7.83 7.77 7.7 7.64 7.57 7.52 7.48 7.42];
59 % H_35 = 10.^(-pH_35);
60 % HCO3_35 = C_NaHCO3(1).*((H_35.*Ka1)/(H_35.^2+H_35.*Ka1+Ka1*Ka2));
61 % CO3_35 = (HCO3_35.*Ka2)./H_35;
62 % OH_35 = Kw(1)./H_35;
63 % Alk_35 = HCO3_35 + 2*CO3_35 + OH_35 + H_35;
64 %
65 % pH_37 = [8.18 8.27 8.23 8.19 8.15 8.09 8.05 8.01 7.97 7.94 7.88];
66 % H_37 = 10.^(-pH_37);

```



```

67 % HCO3_37 = C_NaHCO3(2).*((H_37.*Ka1)./(H_37.^2+H_37.*Ka1+Ka1*Ka2));
68 % CO3_37 = (HCO3_37.*Ka2)./H_37;
69 % OH_37 = Kw(2)./H_37;
70 % Alk_37 = HCO3_37 + 2*CO3_37 + OH_37 + H_37;
71 %
72 % pH_39 = [8.25 8.24 8.18 8.10 8.04 7.96 7.90 7.86 7.81 7.78 7.69];
73 % H_39 = 10.^(-pH_39);
74 % HCO3_39 = C_NaHCO3(3).*((H_39.*Ka1)./(H_39.^2+H_39.*Ka1+Ka1*Ka2));
75 % CO3_39 = (HCO3_39.*Ka2)./H_39;
76 % OH_39 = Kw(3)./H_39;
77 % Alk_39 = HCO3_39 + 2*CO3_39 + OH_39 + H_39;
78 %
79 % pH_41 = [8.17 8.18 8.15 8.12 8.11 8.08 8.06 8.03 8.02 8.01 ...
7.99]; % Just Water
80 % H_41 = 10.^(-pH_41);
81 % HCO3_41 = C_NaHCO3(4).*((H_41.*Ka1)./(H_41.^2+H_41.*Ka1+Ka1*Ka2));
82 % CO3_41 = (HCO3_41.*Ka2)./H_41;
83 % OH_41 = Kw(4)./H_41;
84 % Alk_41 = HCO3_41 + 2*CO3_41 + OH_41 + H_41;
85 %
86 % pH_43 = [8.48 8.19 8.19 8.13 8.07 8.00 7.95 7.91 7.86 7.82 7.76];
87 % H_43 = 10.^(-pH_43);
88 % HCO3_43 = C_NaHCO3(5).*((H_43.*Ka1)./(H_43.^2+H_43.*Ka1+Ka1*Ka2));
89 % CO3_43 = (HCO3_43.*Ka2)./H_43;
90 % OH_43 = Kw(5)./H_43;
91 % Alk_43 = HCO3_43 + 2*CO3_43 + OH_43 + H_43;
92 %
93 % pH_45 = [8.11 8.04 7.91 7.8 7.7 7.61 7.53 7.47 7.42 7.37 7.31];
94 % H_45 = 10.^(-pH_45);
95 % HCO3_45 = C_NaHCO3(6).*((H_45.*Ka1)./(H_45.^2+H_45.*Ka1+Ka1*Ka2));
96 % CO3_45 = (HCO3_45.*Ka2)./H_45;
97 % OH_45 = Kw(6)./H_45;
98 % Alk_45 = HCO3_45 + 2*CO3_45 + OH_45 + H_45;
99 %
100 % pH_47 = [7.99 7.73 7.68 7.6 7.52 7.46 7.37 7.3 7.24 7.19 7.12];
101 % H_47 = 10.^(-pH_47);
102 % HCO3_47 = C_NaHCO3(7).*((H_47.*Ka1)./(H_47.^2+H_47.*Ka1+Ka1*Ka2));
103 % CO3_47 = (HCO3_47.*Ka2)./H_47;
104 % OH_47 = Kw(7)./H_47;
105 % Alk_47 = HCO3_47 + 2*CO3_47 + OH_47 + H_47;
106
107 % pH_24 = [8.16 8.25 8.16 8.05 7.95 7.89];
108 % pH_26 = [8.28 8.27 8.18 8.11 8 7.93];
109 % pH_29 = [8.33 8.38 8.4 8.41 8.41 8.4 8.37 8.37 8.36 8.35 8.32];
110 % pH_30 = [7.62 7.62 7.59 7.57 7.54 7.52 7.5]; %FIJI Water SKIP
111 % pH_31 = [7.59 7.59 7.56 7.53 7.5]; %FIJI Water SKIP
112 % pH_33 = [8.94 8.97 8.92 8.84 8.73 8.64 8.51 8.41 8.38 8.22 8.17];
113
114
115
116 figure (1)
117 hold on
118 %plot(Va_3,pH_24)
119 %plot(Va_3,pH_25)
120 scatter(Va, pH, '*')
121 % scatter(Va_4,pH_35,'r', 'filled', 'DisplayName','Exp. 35')

```

```

122 % scatter(Va_4,pH_37,'b', 'd', 'DisplayName','Exp. 37')
123 % scatter(Va_4,pH_39,'m', '+', 'DisplayName','Exp. 39')
124 % scatter(Va_4,pH_41, '*', 'DisplayName','Exp. 41')
125 % scatter(Va_4,pH_43, 'x', 'DisplayName','Exp. 43')
126 % scatter(Va_4,pH_45, '^', 'DisplayName','Exp. 45')
127 % scatter(Va_4,pH_47, 's', 'DisplayName','Exp. 47')
128 % scatter(Va_6,pH_33,'g', 'h')
129 for i = 1:length(C_NaHCO3)
130     plot(Va_3,pH_3(i,:), 'DisplayName','cats')
131 end
132 xlabel('Va (Liters)')
133 ylabel('pH')
134 legend('show')
135 hold off
136
137 % figure (2)
138 % hold on
139 % for i = 1:length(C_NaHCO3)
140 %     plot(Va_3,Alk(i,:)*1000)
141 % end
142 % xlabel('Volume (L)')
143 % ylabel('Alkalinity (mg/L)')
144 %
145 % scatter(Va_4, Alk_35*1000)
146 % scatter(Va_4, Alk_37*1000)
147 % scatter(Va_4, Alk_39*1000)
148 % scatter(Va_4, Alk_41*1000)
149 % scatter(Va_4, Alk_43*1000)
150 % scatter(Va_4, Alk_45*1000)
151 % scatter(Va_4, Alk_47*1000)
152 % hold off
153
154 % [8.188333333 8.073333333 8.016666667 7.941666667 7.875 ...
      7.803333333 7.74 7.686666667 7.636666667 7.596666667 7.53]

```

```

1 function [ pH ] = pH_curve_fit(C_NaHCO3,C_HNO3,Va,Vb,Kw)
2 %UNTITLED3 Summary of this function goes here
3 %     NaHCO3 + HNO3 Reaction, Finding [H+]
4
5 %Kw = 1*10^-14;
6 Ka1 = 4.46*10^-7; % [HCO3-][H+]/[H2CO3]
7 Ka2 = 4.69*10^-11; % [CO32-][H+]/[HCO3]
8 Ka = 27.29; % [NO3-][H+]/[HNO3]
9
10
11 % M_NaHCO3 = 1; [grams]
12
13 % C_HCO3 = 10^-3; % NAHCO3 Concentration [Moles/Liters]
14
15
16 V_t = Va + Vb;
17 C1 = C_NaHCO3 * Vb/V_t;
18 C2 = C_HNO3 * Va/V_t;
19
20

```

```

21 F_1 = @(x) (1/Kw)*((10.^(-x)).^2 - ...
    ((C1.*Ka1.*((10.^(-x)).^2))./((10.^(-x).^2) + ...
    Ka1.*(10.^(-x)) + Ka1.*Ka2)).*(1+2.*Ka2./(10.^(-x)))) - ...
    (10.^(-x)).*(C2-C1) - Kw);
22
23 x0 = 1e-3;
24
25 options = optimset('Display', ...
    'iter','MaxFunEvals',100000,'MaxIter',15000);
26 pH = fsolve(F_1, x0, options);
27
28
29 end

```

## A.2 System-Level Model Codes

```

1 %%
2 clc
3 clear
4 close all
5
6 %%%%%%%%% INPUT %%%%%%%%%
7 NO2_rate = .1E-7; % Moles/min
8 %%%%%%%%% INPUT %%%%%%%%%
9 pH_in_H2O = [7.34];
10 %%%%%%%%% INPUT %%%%%%%%%
11 Mass_NaHCO3 = 0.0/1000; % HNO3 Concentration[Moles/Liters] % ...
    might have to divide by volume
12 t1 = 0:15/60:1;
13 t2 = 2:1:15;
14 time = [t1 t2 22];
15
16 pH_m = [7.34 6.335 6.03 5.65 5.52 5.175 4.975 4.86 4.655 4.6 ...
    4.535 4.455 4.42 4.39 4.29 4.28 4.215 4.2 4.19 4.15];
17 %pH = zeros(1,length(pH_m));
18 pH = 0;
19 i = 2;
20 j = 1;
21 NO2_s = zeros(1,length(pH_m)-1);
22 NO2 = zeros(1,length(pH_m)-1);
23 NO2_s(j) = 0;
24 t = 0.005;
25 % options = optimset('Display', ...
    'iter','MaxFunEvals',100000,'MaxIter',15000);
26 % pH = fsolve(Find_NO2_rate(NO2_rate,pH_in_H2O,Mass_NaHCO3), ...
    NO2_rate, options);
27 while abs(pH-pH_m(i)) >= 0.0001
28     [pH,NO2_t] = ...
        Find_NO2_rate(NO2_rate,pH_in_H2O,Mass_NaHCO3,time,NO2,i);
29     if abs(pH-pH_m(i)) <= t
30         %if abs(10^-pH-10^-pH_m(i)) <= t
31             NO2_s(j) = NO2_rate;
32             pH_T(j) = pH;
33             NO2(j) = NO2_t; %moles

```

```

34         j = j + 1;
35         i = i + 1;
36 %         if i == 24
37 %             t = 10^-7;
38 %         end
39         if i > length(pH_m)
40             break;
41         end
42         NO2_rate = .1E-7;
43     end
44     if NO2_rate ≥ 1E-3
45         NO2_rate = NO2_rate + .1E-4
46     elseif NO2_rate ≥ 1E-4
47         NO2_rate = NO2_rate + .1E-5
48     elseif NO2_rate ≥ 1E-5
49         NO2_rate = NO2_rate + .1E-6
50     else
51         NO2_rate = NO2_rate + .1E-7
52     end
53     if i > length(pH_m)
54         break;
55     end
56 end
57 pH
58 NO2_rate
59
60 t3 = 15/60:15/60:1;
61 time_s = [t3 t2 22];
62
63 average = mean(NO2_s);
64 waverage = sum(NO2_s.*time_s)./sum(time_s);
65 NO2_z = zeros(1,length(pH_m)-1);
66 for k = 1:length(NO2)
67     NO2_z(k) = NO2(k)/(time(k+1)-time(k));
68     aver(k) = average;
69     waver(k) = waverage;
70 end
71 Vb = 250/1000; %liter
72 NO3_minus = NO2./Vb .* 2/3 * 62.0049 * 1000; % ppm (NO3-)
73
74 NO3_ave = [6 7.333333333 6.666666667 6.5 7.666666667 8.333333333 ...
8.666666667 9.333333333 12 15 16.33333333 19 21.66666667 ...
25.33333333 27.66666667 31.33333333 33.66666667 39.33333333 ...
43.66666667 48.66666667 52.5 61.66666667 69.33333333 ...
74.33333333 81.66666667 91.33333333];
75
76 NO2_a(1) = time(1)*NO2_s(1)+3/2*NO3_ave(1)/62.0049/1000*Vb(1);
77 for i = 2:length(time)
78     NO2_a(i) = NO2_a(i-1) + NO2_s(i-1)*(time(i)-time(i-1));
79 end
80
81 C_NO2 = NO2_a/Vb(1); % moles/Liter
82 C_NO3 = 2/3 .* C_NO2 * 62.0049 * 1000 ; %ppm
83
84 figure (1)
85 hold on

```

```

86 scatter(time_s,NO2_s,'*')
87 scatter(time_s,NO2_z)
88 plot(time_s,aver)
89 hold off
90 figure (2)
91 hold on
92 scatter(time, pH_m)
93 scatter(time_s,pH_T)
94 hold off
95 figure (3)
96 hold on
97 scatter(time_s,NO2_s,'*')
98 plot(time_s,NO2_s)
99 plot(time_s,aver)
100 plot(time_s,waver)
101 hold off
102 figure (4)
103 hold on
104 scatter(time,NO3_ave)
105 scatter(time_s,NO3_minus)
106 scatter(time,C_NO3,'*')
107 hold off
108
109 percent_error = (abs(pH_m - [0 pH_T]))./pH_m*100
110 [NO2_s(:) NO2_z(:) NO2(:)]
111 %R5 0-22 [6.28 5.77 4.99 4.64 4.49 4.11 3.93 3.83 3.73 3.67 3.6 ...
           3.55 3.5 3.45 3.42 3.39 3.35 3.31 3.28 3.25 3.23 3.2 3.17 ...
           3.14 3.11 3.09]
112 %R5 0-22 [6.14 5.68 4.65 4.44 4.3 4.06 3.95 3.86 3.74 3.69 3.6 ...
           3.57 3.57 3.51 3.45 3.4 3.37 3.34 3.3 3.28 3.25 3.22 3.18 ...
           3.17 3.14 3.13]
113 %R5 0-22 [5.36 5.35 4.88 4.45 4.17 4.01 3.85 3.81 3.76 3.7 3.65 ...
           3.61 3.55 3.52 3.48 3.45 3.41 3.36 3.35 3.31 3.29 3.26 3.25 ...
           3.23 3.21 3.18]
114 %R3 0-15,22 [7.1 6.09 5.9 5.5 5.31 5.04 4.86 4.79 4.56 4.52 4.41 ...
              4.33 4.28 4.26 4.23 4.17 4.16 4.14 4.14 4.09]
115 %R3 0-15,22 [7.58 6.58 6.16 5.8 5.73 5.31 5.09 4.93 4.75 4.68 ...
              4.66 4.58 4.56 4.52 4.35 4.39 4.27 4.26 4.24 4.21]
116 %R5 0-22 [6.98 5.11 4.3 4.18 4.09 3.81 3.77 3.7 3.63 3.59 3.53 ...
              3.49 3.46 3.4 3.36 3.36 3.32 3.29 3.27 3.24 3.23 3.21 3.2 ...
              3.18 3.14 3.13]
117 %R5 0-17 [7.12 6.12 5.65 5.39 5.26 4.89 4.69 4.6 4.49 4.41 4.37 ...
              4.3 4.27 4.24 4.19 4.18 4.14 4.1 4.08 4.03 4.04]
118 %R3-ave 0-15,22 [7.34 6.335 6.03 5.65 5.52 5.175 4.975 4.86 ...
                   4.655 4.6 4.535 4.455 4.42 4.39 4.29 4.28 4.215 4.2 4.19 4.15]
119
120 % 0mg [5.902857143 5.274285714 4.707142857 4.447142857 ...
         4.292857143 4.02 3.868571429 3.775714286 3.682857143 ...
         3.618571429 3.557142857 3.511428571 3.475714286 3.425714286 ...
         3.388571429 3.35 3.32 3.281428571 3.248571429 3.217142857 ...
         3.19 3.165714286 3.141428571 3.118571429 3.085714286 3.06]
121 % 1mg [6.8425 6.7825 6.62 6.4325 6.26 5.5775 4.6575 4.26 4.0625 ...
         3.9625 3.86 3.8 3.725 3.665 3.61 3.57 3.5375 3.5025 3.4775 ...
         3.4425 3.4075 3.3775 3.3525 3.325 3.3025 3.2575]

```

```

122 % 2mg [7.205 6.95 6.8875 6.823333333 6.7 6.32 6.0775 5.27 4.9075 ...
        4.5575 4.2725 4.075 3.945 3.865 3.7975 3.7425 3.685 3.6425 ...
        3.595 3.56 3.52 3.475 3.4375 3.4 3.375 3.3375]
123 % 5mg [7.425 7.303333333 7.238333333 7.138333333 7.053333333 ...
        6.741666667 6.456666667 6.123333333 5.545 4.95 4.556666667 ...
        4.268333333 4.07 3.955 3.868333333 3.783333333 3.718333333 ...
        3.661666667 3.601666667 3.556666667 3.511666667 3.475 ...
        3.433333333 3.401666667 3.363333333 3.333333333]
124 % 10mg [7.728333333 7.538333333 7.48 7.405 7.355 7.175 7.03 ...
        6.886666667 6.751666667 6.611666667 6.476666667 6.268333333 ...
        6.013333333 5.505 4.756666667 4.425 4.225 4.093333333 3.98 ...
        3.875 3.803333333 3.736666667 3.678333333 3.628333333 3.58 ...
        3.531666667]
125 % 15mg [7.9 7.753333333 7.72 7.693333333 7.33 7.503333333 ...
        7.363333333 7.283333333 7.17 7.086666667 7.016666667 6.93 ...
        6.846666667 6.756666667 6.653333333 6.513333333 6.323333333 ...
        6.036666667 5.65 5.253333333 4.98 4.743333333 4.443333333 ...
        4.203333333 4.06 3.966666667]
126 % 20mg [7.994 7.784 7.742 7.696 7.648 7.48 7.378 7.268 7.206 ...
        7.128 7.072 7.016 6.94 6.89 6.826 6.764 6.68 6.61 6.522 ...
        6.418 6.28 6.062 5.692 5.288 5.002 4.652]
127 % 50mg [8.15 8.086666667 8.063333333 8.033333333 7.976666667 ...
        7.913333333 7.813333333 7.76 7.703333333 7.676666667 7.62 ...
        7.593333333 7.566666667 7.563333333 7.55 7.526666667 ...
        7.513333333 7.483333333 7.49 7.476666667 7.473333333 7.48 ...
        7.466666667 7.453333333 7.43 7.413333333]
128
129 % 1mg [6.923333333 6.85 6.693333333 6.593333333 6.406666667 5.77 ...
        4.776666667 4.316666667 4.103333333 3.996666667 3.883333333 ...
        3.826666667 3.74 3.68 3.616666667 3.573333333 3.543333333 ...
        3.506666667 3.48 3.44 3.4 3.366666667 3.336666667 3.31 ...
        3.286666667 3.236666667]
130 % 15mg [7.8975 7.7875 7.76 7.725 7.425 7.505 7.3675 7.285 7.17 ...
        7.0875 7.0175 6.94 6.8625 6.78 6.6925 6.5775 6.42 6.1975 ...
        5.89 5.5775 5.35 5.155 4.9025 4.6875 4.535 4.41]
131 % 20mg [7.965 7.8425 7.79 7.7375 7.6825 7.4925 7.385 7.265 7.2 ...
        7.1125 7.0575 6.9975 6.9125 6.86 6.785 6.725 6.6325 6.5625 ...
        6.4675 6.3525 6.195 5.9475 5.5025 5.0325 4.6525 4.3525]
132 % 50mg [8.23 8.15 8.13 8.105 8.025 7.955 7.835 7.79 7.725 7.71 ...
        7.64 7.62 7.595 7.585 7.57 7.535 7.525 7.485 7.495 7.48 ...
        7.475 7.485 7.465 7.455 7.42 7.395]
133
134 % Reactor (3)
135 % 0mg [7.34 6.335 6.03 5.65 5.52 5.175 4.975 4.86 4.655 4.6 ...
        4.535 4.455 4.42 4.39 4.29 4.28 4.215 4.2 4.19 4.15]

```

```

1 function [ pH,NO2 ] = ...
    Find_NO2_rate(NO2_rate,pH_in_H2O,Mass_NaHCO3,time,NO2_in,k)
2 %% pH vs time
3
4
5 %NO2_rate = [4.5E-7 5E-6]; % Moles/min
6 %NO2_rate = [1.83E-06 1.83E-06]; % Moles/min
7 %NO2_rate = [2.63E-06 2.63E-06]; % Moles/min
8

```

```

9
10
11 MM = 84.007; % Molar Mass of NaHCO3
12
13
14 C_NaHCO3_mol = Mass_NaHCO3./MM;
15 % pH_in_HNO3 = [4.46 4.44 4.92 6.55 4.84];
16 % C_HNO3 = 10.^(-pH_in_HNO3);
17
18
19
20 Kw = (10.^(-pH_in_H2O)).^2;
21 Ka1 = 4.46*10^-7; % [HCO3-][H+]/[H2CO3]
22 Ka2 = 4.69*10^-11; % [CO32-][H+]/[HCO3]
23
24 Vb = [250]/1000;
25 C_NaHCO3 = C_NaHCO3_mol./Vb;
26
27
28 % Va_3 = 0:0.025:0.250; % [Liters]
29
30 NO2 = 0;
31 pH = zeros(length(C_NaHCO3),length(time));
32 Alk = zeros(length(C_NaHCO3),length(time));
33 i = 0;
34 j = 0;
35 for j = 1:length(C_NaHCO3)
36     for i = 1:length(time)
37
38         [pH,NO2] = ...
            pH_curve_fit_MODEL_3(C_NaHCO3(j),NO2_rate(j),time,Vb(j),Kw(j),NO2_in,k)
39         if i ==1
40             break;
41         end
42     end
43 end
44
45 % for i = 1:length(C_NaHCO3)
46 %     plot(time,pH(i,:), 'DisplayName','NO2 Model')
47 % end
48 % xlabel('time (minutes)')
49 % ylabel('pH')
50 % legend('show')
51
52 end

```

```

1 function [ pH,NO2 ] = ...
    pH_curve_fit_MODEL_3(C_NaHCO3,NO2_rate,time,Vb,Kw,NO2_in,k)
2 %UNTITLED3 Summary of this function goes here
3 %     NaHCO3 + HNO3 Reaction, Finding [H+]
4
5 %Kw = 1*10^-14;
6 Ka1 = 4.46*10^-7; % [HCO3-][H+]/[H2CO3]
7 Ka2 = 4.69*10^-11; % [CO32-][H+]/[HCO3]
8 Ka = 27.29; % [NO3-][H+]/[HNO3]

```

```

9
10
11 % M_NaHCO3 = 1; [grams]
12
13 % C_HCO3 = 10^-3; % NAHCO3 Concentration [Moles/Liters]
14
15 if k == 2
16     NO2 = (time(k)-time(k-1)) .* NO2_rate;
17 else
18     NO2 = NO2_in(k-2) + (time(k)-time(k-1)) .* NO2_rate;
19 end
20
21 C_NO2 = NO2/Vb; % moles/Liter
22 C_NO3 = 2/3 .* C_NO2;
23 % V_t = Va;
24 C1 = C_NaHCO3;
25 % C2 = C_HNO3 * Va/V_t;
26
27
28 F_1 = @(x) (1/Kw)*((10.^(-x)).^2 - ...
    ((C1.*Ka1.*((10.^(-x)).^2))./((10.^(-x).^2) + ...
    Ka1.*(10.^(-x)) + Ka1.*Ka2)).*(1+2.*Ka2./(10.^(-x))) - ...
    (10.^(-x)).*(C_NO3-C1) - Kw);
29 %F_1 = @(x) (1/Kw)*((10.^(-x)).^2 + C1.*((10.^(-x)) - ...
    (Ka1.*((10.^(-x)).^2))./((10.^(-x).^2)).*(1+2.*Ka2./(10.^(-x)))) ...
    - Kw - C_NO3.*10.^(-x));
30 x0 = 1e-3;
31
32 options = optimset('Display', ...
    'iter','MaxFunEvals',100000,'MaxIter',15000);
33 pH = fsolve(F_1, x0, options);
34
35
36 end

```

```

1 %%
2 clc
3 clear
4 close all
5
6 %%%%%%%%% INPUT %%%%%%%%%
7 NO2_rate = .1E-7; % Moles/min
8 %%%%%%%%% INPUT %%%%%%%%%
9 pH_in_H2O = [6.35];
10 %%%%%%%%% INPUT %%%%%%%%%
11 Mass_NaHCO3 = 50.0/1000; % HNO3 Concentration[Moles/Liters] % ...
    might have to divide by volume
12 t1 = 0:15/60:1;
13 t2 = 2:1:22;
14 time = [t1 t2];
15
16 NO3_m = [5.5 5.5 5.5 6.5 6.5 8 8 9 9.5 10.5 11.5 13.5 14 15.5 16 ...
    17.5 18.5 18.5 19.5 22 24.5 27.5 27 27.5 28.5 29.5];

```



```

17 pH_m = [8.15 8.086666667 8.063333333 8.033333333 7.976666667 ...
          7.913333333 7.813333333 7.76 7.703333333 7.676666667 7.62 ...
          7.593333333 7.566666667 7.563333333 7.55 7.526666667 ...
          7.513333333 7.483333333 7.49 7.476666667 7.473333333 7.48 ...
          7.466666667 7.453333333 7.43 7.413333333];
18 %pH = zeros(1,length(pH_m));
19 NO3 = 0;
20 pH = 0;
21 i = 2;
22 j = 1;
23 NO2_s = zeros(1,length(pH_m)-1);
24 NO2 = zeros(1,length(pH_m)-1);
25 NO2_s(j) = 0;
26 t = 0.5;
27 % options = optimset('Display', ...
    'iter','MaxFunEvals',100000,'MaxIter',15000);
28 % pH = fsolve(Find_NO2_rate(NO2_rate,pH_in_H2O,Mass_NaHCO3), ...
    NO2_rate, options);
29 while abs(NO3-NO3_m(i)) ≥ 0.0001
30     [pH,NO2_t,NO3] = ...
        Find_NO2_rate_2(NO2_rate,pH_in_H2O,Mass_NaHCO3,time,NO2,i);
31     NO3 = NO3 * 62.0049 * 1000; % moles/liter ---> mg/liter
32     if abs(NO3-NO3_m(i)) ≤ t
33         %if abs(10^-pH-10^-pH_m(i)) ≤ t
34             NO2_s(j) = NO2_rate;
35             pH_T(j) = pH;
36             NO2(j) = NO2_t; %moles
37             NO3_t(j) = NO3;
38             j = j + 1;
39             i = i + 1;
40         %         if i == 24
41         %             t = 10^-7;
42         %         end
43         if i > length(pH_m)
44             break;
45         end
46         NO2_rate = .1E-7;
47     end
48     if NO2_rate ≥ 1E-3
49         NO2_rate = NO2_rate + .1E-4
50     elseif NO2_rate ≥ 1E-4
51         NO2_rate = NO2_rate + .1E-5
52     elseif NO2_rate ≥ 1E-5
53         NO2_rate = NO2_rate + .1E-6
54     else
55         NO2_rate = NO2_rate + .1E-7
56     end
57     if i > length(pH_m)
58         break;
59     end
60 end
61 pH
62 NO2_rate
63
64 t3 = 15/60:15/60:1;
65 time_s = [t3 t2];

```

```

66
67 average = mean(NO2_s);
68 waverage = sum(NO2_s.*time_s)./sum(time_s);
69 NO2_z = zeros(1,length(pH_m)-1);
70 for k = 1:length(NO2)
71     NO2_z(k) = NO2(k)/(time(k+1)-time(k));
72     aver(k) = average;
73     waver(k) = waverage;
74 end
75 Vb = 250/1000; %liter
76 NO3_minus = NO2./Vb .* 2/3 * 62.0049 * 1000; % ppm (NO3-)
77
78 NO2_a(1) = time(1)*NO2_s(1)+3/2*NO3_m(1)/62.0049/1000*Vb(1);
79 for i = 2:length(time)
80     NO2_a(i) = NO2_a(i-1) + NO2_s(i-1)*(time(i)-time(i-1));
81 end
82
83 C_NO2 = NO2_a/Vb(1); % moles/Liter
84 C_NO3 = 2/3 .* C_NO2 * 62.0049 * 1000 ; %ppm
85
86
87 figure (1)
88 hold on
89 scatter(time_s,NO2_s,'*')
90 scatter(time_s,NO2_z)
91 plot(time_s,aver)
92 hold off
93 figure (2)
94 hold on
95 scatter(time, pH_m)
96 scatter(time_s,pH_T)
97 hold off
98 figure (3)
99 hold on
100 scatter(time_s,NO2_s,'*')
101 plot(time_s,NO2_s)
102 plot(time_s,aver)
103 plot(time_s,waver)
104 hold off
105 figure (4)
106 hold on
107 scatter(time_s,NO3_minus)
108 scatter(time,NO3_m)
109 scatter(time_s,NO3_t,'*')
110 scatter(time,C_NO3,'>')
111 hold off
112 percent_error_1 = (abs(pH_m - [0 pH_T]))./pH_m*100
113 percent_error_2 = (abs(NO3_m - [0 NO3_t]))./pH_m*100
114 [NO2_s(:) NO2_z(:) NO2(:)]
115
116 % pH
117 %R5 0-22 [6.28 5.77 4.99 4.64 4.49 4.11 3.93 3.83 3.73 3.67 3.6 ...
          3.55 3.5 3.45 3.42 3.39 3.35 3.31 3.28 3.25 3.23 3.2 3.17 ...
          3.14 3.11 3.09]

```

```

118 %R5 0-22 [6.14 5.68 4.65 4.44 4.3 4.06 3.95 3.86 3.74 3.69 3.6 ...
      3.57 3.51 3.45 3.4 3.37 3.34 3.3 3.28 3.25 3.22 3.18 ...
      3.17 3.14 3.13]
119 %R5 0-22 [5.36 5.35 4.88 4.45 4.17 4.01 3.85 3.81 3.76 3.7 3.65 ...
      3.61 3.55 3.52 3.48 3.45 3.41 3.36 3.35 3.31 3.29 3.26 3.25 ...
      3.23 3.21 3.18]
120 %R3 0-15,22 [7.1 6.09 5.9 5.5 5.31 5.04 4.86 4.79 4.56 4.52 4.41 ...
      4.33 4.28 4.26 4.23 4.17 4.16 4.14 4.14 4.09]
121 %R3 0-15,22 [7.58 6.58 6.16 5.8 5.73 5.31 5.09 4.93 4.75 4.68 ...
      4.66 4.58 4.56 4.52 4.35 4.39 4.27 4.26 4.24 4.21]
122 %R5 0-22 [6.98 5.11 4.3 4.18 4.09 3.81 3.77 3.7 3.63 3.59 3.53 ...
      3.49 3.46 3.4 3.36 3.36 3.32 3.29 3.27 3.24 3.23 3.21 3.2 ...
      3.18 3.14 3.13]
123 %R5 0-17 [7.12 6.12 5.65 5.39 5.26 4.89 4.69 4.6 4.49 4.41 4.37 ...
      4.3 4.27 4.24 4.19 4.18 4.14 4.1 4.08 4.03 4.04]
124
125
126 % 0mg [5.902857143 5.274285714 4.707142857 4.447142857 ...
      4.292857143 4.02 3.868571429 3.775714286 3.682857143 ...
      3.618571429 3.557142857 3.511428571 3.475714286 3.425714286 ...
      3.388571429 3.35 3.32 3.281428571 3.248571429 3.217142857 ...
      3.19 3.165714286 3.141428571 3.118571429 3.085714286 3.06]
127 % 1mg [6.8425 6.7825 6.62 6.4325 6.26 5.5775 4.6575 4.26 4.0625 ...
      3.9625 3.86 3.8 3.725 3.665 3.61 3.57 3.5375 3.5025 3.4775 ...
      3.4425 3.4075 3.3775 3.3525 3.325 3.3025 3.2575]
128 % 2mg [7.205 6.95 6.8875 6.823333333 6.7 6.32 6.0775 5.27 4.9075 ...
      4.5575 4.2725 4.075 3.945 3.865 3.7975 3.7425 3.685 3.6425 ...
      3.595 3.56 3.52 3.475 3.4375 3.4 3.375 3.3375]
129 % 5mg [7.425 7.303333333 7.238333333 7.138333333 7.053333333 ...
      6.741666667 6.456666667 6.123333333 5.545 4.95 4.556666667 ...
      4.268333333 4.07 3.955 3.868333333 3.783333333 3.718333333 ...
      3.661666667 3.601666667 3.556666667 3.511666667 3.475 ...
      3.433333333 3.401666667 3.363333333 3.333333333]
130 % 10mg [7.728333333 7.538333333 7.48 7.405 7.355 7.175 7.03 ...
      6.886666667 6.751666667 6.611666667 6.476666667 6.268333333 ...
      6.013333333 5.505 4.756666667 4.425 4.225 4.093333333 3.98 ...
      3.875 3.803333333 3.736666667 3.678333333 3.628333333 3.58 ...
      3.531666667]
131 % 15mg [7.9 7.753333333 7.72 7.693333333 7.33 7.503333333 ...
      7.363333333 7.283333333 7.17 7.086666667 7.016666667 6.93 ...
      6.846666667 6.756666667 6.653333333 6.513333333 6.323333333 ...
      6.036666667 5.65 5.253333333 4.98 4.743333333 4.443333333 ...
      4.203333333 4.06 3.966666667]
132 % 20mg *[7.994 7.784 7.742 7.696 7.648 7.48 7.378 7.268 7.206 ...
      7.128 7.072 7.016 6.94 6.89 6.826 6.764 6.68 6.61 6.522 ...
      6.418 6.28 6.062 5.692 5.288 5.002 4.652]
133 % 50mg *[8.15 8.086666667 8.063333333 8.033333333 7.976666667 ...
      7.913333333 7.813333333 7.76 7.703333333 7.676666667 7.62 ...
      7.593333333 7.566666667 7.563333333 7.55 7.526666667 ...
      7.513333333 7.483333333 7.49 7.476666667 7.473333333 7.48 ...
      7.466666667 7.453333333 7.43 7.413333333]
134

```

```

135 % 1mg [6.923333333 6.85 6.693333333 6.593333333 6.406666667 5.77 ...
        4.776666667 4.316666667 4.103333333 3.996666667 3.883333333 ...
        3.826666667 3.74 3.68 3.616666667 3.573333333 3.543333333 ...
        3.506666667 3.48 3.44 3.4 3.366666667 3.336666667 3.31 ...
        3.286666667 3.236666667]
136 % 15mg *[7.8975 7.7875 7.76 7.725 7.425 7.505 7.3675 7.285 7.17 ...
        7.0875 7.0175 6.94 6.8625 6.78 6.6925 6.5775 6.42 6.1975 ...
        5.89 5.5775 5.35 5.155 4.9025 4.6875 4.535 4.41]
137 % 20mg [7.965 7.8425 7.79 7.7375 7.6825 7.4925 7.385 7.265 7.2 ...
        7.1125 7.0575 6.9975 6.9125 6.86 6.785 6.725 6.6325 6.5625 ...
        6.4675 6.3525 6.195 5.9475 5.5025 5.0325 4.6525 4.3525]
138 % 50mg [8.23 8.15 8.13 8.105 8.025 7.955 7.835 7.79 7.725 7.71 ...
        7.64 7.62 7.595 7.585 7.57 7.535 7.525 7.485 7.495 7.48 ...
        7.475 7.485 7.465 7.455 7.42 7.395]
139
140 % Reactor (3)
141 % 0mg [7.34 6.335 6.03 5.65 5.52 5.175 4.975 4.86 4.655 4.6 ...
        4.535 4.455 4.42 4.39 4.29 4.28 4.215 4.2 4.19 4.15]
142
143 % NO3-
144 % 0mg [3.5 5 8.125 10.625 13.125 18.375 22.375 25.75 29.875 ...
        34.625 37.25 39.875 45.875 50 54.25 60.25 65.625 70.875 ...
        78.125 83 90.625 95.75 104.25 112.75 125.125 131.25]
145 % 1mg [5.333333333 5.333333333 5.333333333 6 6 8 9.666666667 13 ...
        15.33333333 17.33333333 21.33333333 24 29.33333333 32 34 ...
        37.33333333 39.33333333 43.33333333 49 50.33333333 58 62 69 ...
        74.66666667 79 81.33333333]
146 % 2mg [6 7.333333333 6.666666667 6.5 7.666666667 8.333333333 ...
        8.666666667 9.333333333 12 15 16.33333333 19 21.66666667 ...
        25.33333333 27.66666667 31.33333333 33.66666667 39.33333333 ...
        43.66666667 48.66666667 52.5 61.66666667 69.33333333 ...
        74.33333333 81.66666667 91.33333333]
147 % 5mg [5.5 6 6 6 7.25 7.25 8.25 9.25 10.75 12.75 15.25 18 ...
        20.75 23.75 27.5 31 36.33333333 40.75 44.75 48.5 56.5 63.25 ...
        71.25 79.25 88.75]
148 % 10mg [6.833333333 7.833333333 7.833333333 8.333333333 8 8.5 ...
        9.5 10 10.66666667 11.33333333 12 12.66666667 12.83333333 ...
        12.83333333 13.66666667 16 18 20.83333333 24.66666667 28 ...
        31.66666667 35.5 40 45.5 51.5 58.16666667]
149 % 15mg [7 6 6.666666667 6.666666667 6.666666667 7.333333333 ...
        7.333333333 7.666666667 8.666666667 9.333333333 10.33333333 ...
        11.33333333 11 12 12.66666667 13.33333333 14 14.33333333 15 ...
        15.66666667 17 19 20.66666667 23.66666667 27.33333333 ...
        31.33333333]
150 % 20mg [5.4 5.8 6.2 6.8 6.2 7.2 7.2 7.8 8.8 9 10 9.8 10.4 11.4 ...
        12.2 13 14 14.4 14.6 15.8 16.4 16.6 17 17.4 19 20.8]
151 % 50mg [5.5 5.5 5.5 6.5 6.5 8 8 9 9.5 10.5 11.5 13.5 14 15.5 16 ...
        17.5 18.5 18.5 19.5 22 24.5 27.5 27 27.5 28.5 29.5]

```

```

1 function [ pH,NO2,NO3 ] = ...
        Find_NO2_rate_2(NO2_rate,pH_in_H2O,Mass_NaHCO3,time,NO2_in,k)
2 %% pH vs time
3
4
5 %NO2_rate = [4.5E-7 5E-6]; % Moles/min

```

```

6 %NO2_rate = [1.83E-06 1.83E-06]; % Moles/min
7 %NO2_rate = [2.63E-06 2.63E-06]; % Moles/min
8
9
10
11 MM = 84.007; % Molar Mass of NaHCO3
12
13
14 C_NaHCO3_mol = Mass_NaHCO3./MM;
15 % pH_in_HNO3 = [4.46 4.44 4.92 6.55 4.84];
16 % C_HNO3 = 10.^(-pH_in_HNO3);
17
18
19
20 Kw = (10.^(-pH_in_H2O)).^2;
21 Ka1 = 4.46*10^-7; % [HCO3-][H+]/[H2CO3]
22 Ka2 = 4.69*10^-11; % [CO32-][H+]/[HCO3]
23
24 Vb = [250]/1000;
25 C_NaHCO3 = C_NaHCO3_mol./Vb;
26
27
28 % Va_3 = 0:0.025:0.250; % [Liters]
29
30 NO2 = 0;
31 NO3 = 0;
32 pH = zeros(length(C_NaHCO3),length(time));
33 Alk = zeros(length(C_NaHCO3),length(time));
34 i = 0;
35 j = 0;
36 for j = 1:length(C_NaHCO3)
37     for i = 1:length(time)
38
39         [pH,NO2,NO3] = ...
            pH_curve_fit_MODEL_4(C_NaHCO3(j),NO2_rate(j),time,Vb(j),Kw(j),NO2_in,k)
40         if i ==1
41             break;
42         end
43     end
44 end
45
46 % for i = 1:length(C_NaHCO3)
47 %     plot(time,pH(i,:), 'DisplayName','NO2 Model')
48 % end
49 % xlabel('time (minutes)')
50 % ylabel('pH')
51 % legend('show')
52
53 end

```

```

1 function [ pH,NO2,C_NO3 ] = ...
    pH_curve_fit_MODEL_4(C_NaHCO3,NO2_rate,time,Vb,Kw,NO2_in,k)
2 %UNTITLED3 Summary of this function goes here
3 %     NaHCO3 + HNO3 Reaction, Finding [H+]
4

```

```

5 %Kw = 1*10^-14;
6 Ka1 = 4.46*10^-7; % [HCO3-][H+]/[H2CO3]
7 Ka2 = 4.69*10^-11; % [CO32-][H+]/[HCO3]
8 Ka = 27.29; % [NO3-][H+]/[HNO3]
9
10
11 % M_NaHCO3 = 1; [grams]
12
13 % C_HCO3 = 10^-3; % NAHCO3 Concentration [Moles/Liters]
14
15 if k == 2
16     NO2 = (time(k)-time(k-1)) .* NO2_rate;
17 else
18     NO2 = NO2_in(k-2) + (time(k)-time(k-1)) .* NO2_rate;
19 end
20
21 C_NO2 = NO2/Vb; % moles/Liter
22 C_NO3 = 2/3 .* C_NO2; % moles/Liter
23 % V_t = Va;
24 C1 = C_NaHCO3;
25 % C2 = C_HNO3 * Va/V_t;
26
27
28 F_1 = @(x) (1/Kw)*((10.^(-x)).^2 - ...
    ((C1.*Ka1.*((10.^(-x)).^2))./((10.^(-x).^2) + ...
    Ka1.*(10.^(-x)) + Ka1.*Ka2)).*(1+2.*Ka2./(10.^(-x))) - ...
    (10.^(-x)).*(C_NO3-C1) - Kw);
29 %F_1 = @(x) (1/Kw)*((10.^(-x)).^2 + C1.*((10.^(-x)) - ...
    (Ka1.*((10.^(-x)).^2))./((10.^(-x).^2)).*(1+2.*Ka2./(10.^(-x)))) ...
    - Kw - C_NO3.*10.^(-x));
30 x0 = 1e-3;
31
32 options = optimset('Display', ...
    'iter','MaxFunEvals',100000,'MaxIter',15000);
33 pH = fsolve(F_1, x0, options);
34
35
36 end

```

```

1 %% pH vs time
2
3
4 clc
5 clear
6 close all
7
8 %NO2_rate = [4.5E-7 5E-6]; % Moles/min
9 %NO2_rate = [1.83E-06 1.83E-06]; % Moles/min
10 %NO2_rate = [2.63E-06 2.63E-06]; % Moles/min
11
12 %%%%%%%%% INPUT %%%%%%%%%
13 NO2_rate = [1.8e-06 15.0e-06 4.05e-06 33.75e-06]; % Moles/min
14
15 MM = 84.007; % Molar Mass of NaHCO3
16 %%%%%%%%% INPUT %%%%%%%%%

```

```

17 Mass_NaHCO3 = [50.0 50.0 50.0]/1000; % HNO3 Concentration[Moles]
18
19 C_NaHCO3_mol = Mass_NaHCO3./MM;
20 % pH_in_HNO3 = [4.46 4.44 4.92 6.55 4.84];
21 % C_HNO3 = 10.^(-pH_in_HNO3);
22
23 %%%%%%%%% INPUT %%%%%%%%%
24 pH_in_H2O = [6.35 6.35 6.35];
25
26 tbreak = 30.0; % break time for different NO2 rate
27
28 Kw = (10.^(-pH_in_H2O)).^2;
29 Ka1 = 4.46*10^-7; % [HCO3-][H+]/[H2CO3]
30 Ka2 = 4.69*10^-11; % [CO32-][H+]/[HCO3]
31
32 Vb = [250 250 250]/1000;
33 C_NaHCO3 = C_NaHCO3_mol./Vb; % [Moles/Liter]
34
35 time = 0:15/60:22;
36 % Va_3 = 0:0.025:0.250; % [Liters]
37
38 NO3_ave = [5.333333333 5.333333333 5.333333333 6 6 8 9.666666667 ...
13 15.33333333 17.33333333 21.33333333 24 29.33333333 32 34 ...
37.33333333 39.33333333 43.33333333 49 50.33333333 58 62 69 ...
74.66666667 79 81.33333333];
39
40
41 NO2(1) = time(1)*NO2_rate(2); % 3/2*NO3_ave(1)/62.0049/1000*Vb(1);
42 for i = 2:length(time)
43     if (time(i) ≤ tbreak)
44         k = 3;
45     else
46         k = 4;
47     end
48     NO2(i) = NO2(i-1) + NO2_rate(k)*(time(i)-time(i-1));
49 end
50
51 C_NO22 = NO2./Vb(1); % moles/Liter
52 %C_NO3 = 2/3 .* C_NO2 * 62.0049 * 1000; %ppm
53
54
55 pH = zeros(length(C_NaHCO3),length(time));
56 Alk = zeros(length(C_NaHCO3),length(time));
57 i = 0;
58 j = 0;
59 for j = 1:length(C_NaHCO3)
60     for i = 1:length(time)
61
62         pH(j,i) = pH_curve_fit_MODEL_5(C_NaHCO3(j),C_NO22(i),Kw(j));
63
64         H_plus = 10.^(-pH(j,i));
65         HCO3 = ...
            C_NaHCO3(j)*((H_plus*Ka1)/(H_plus^2+H_plus*Ka1+Ka1*Ka2));
66         CO3 = (HCO3*Ka2)/H_plus;
67         OH = Kw(j)/H_plus;
68         Alk(j,i) = HCO3 + 2*CO3 + OH + H_plus;

```

```

69     end
70 end
71
72 %NO2 = zeros(length(C_NaHCO3),length(time));
73 %for i = 1:length(NO2_rate)
74 %     NO2 = time .* NO2_rate(i); %NO2_init +
75 %     C_NO2 = NO2/Vb(i); % moles/Liter
76 %     C_NO3(i,:) = 3/2 .* C_NO2 * 62.0049 * 1000; %ppm
77 %end
78
79
80
81
82 pH
83 % pH_20 = [7.71 7.66 7.61 7.58 7.54 7.53 7.5 7.44 7.41 7.38 7.32 ...
            7.3 7.38 7.25 7.22 7.2 7.16 7.21 7.19 7.13 7.12 7.08 7.06 ...
            7.04 7.04 7.01 6.97];
84 % t_1 = [0 10 15 30 45 60]/60;
85 % t_2 = 2:1:22;
86 % time_20 = [t_1 t_2];
87 %
88 % pH_19 = [7.78 7.67 7.56 7.48 7.45 7.42 7.36 7.25 7.17 7.11 ...
            7.05 6.98 6.94 6.87 6.81 6.78 6.74 6.67 6.63 6.55 6.41 6.18 ...
            6.05 5.86 5.63 5.5 5.35];
89 % t_3 = 2:1:15;
90 % t_4 = 19:1:24;
91 % time_19 = [t_1 t_3 17 t_4];
92
93 pH_ave = [8.15 8.086666667 8.063333333 8.033333333 7.976666667 ...
            7.913333333 7.813333333 7.76 7.703333333 7.676666667 7.62 ...
            7.593333333 7.566666667 7.563333333 7.55 7.526666667 ...
            7.513333333 7.483333333 7.49 7.476666667 7.473333333 7.48 ...
            7.466666667 7.453333333 7.43 7.413333333];
94 t_1 = [0 15 30 45 60]/60;
95 t_2 = 2:1:22;
96 time_19 = [t_1 t_2];
97
98 pH_UE = [6.88 6.03 5.77 5.62 5.52 5.31 5.23 5.12 5.11 5.04 5.01 ...
            4.98 4.96 4.95 4.95 4.94 4.94 4.91 4.92 4.94 4.92 4.98 4.98 ...
            4.99 4.99 5.0];
99 time_20 = [t_1 t_2];
100
101 pH_LE = [6.28 5.31 4.76 4.56 4.45 4.11 4.11 3.87 3.93 3.72 3.68 ...
            3.63 3.59 3.54 3.50 3.47 3.44 3.40 3.37 3.35 3.32 3.27 3.24 ...
            3.22 3.19 3.17];
102
103 %%%%%%%%%%% INCORRECT NO3- DO NOT COPY %%%%%%%%%%%
104 NO2(1) = time(1)*NO2_rate(1)+2/3*NO3_ave(1)/62.0049/1000*Vb(1);
105 for i = 2:length(time)
106     if (time(i) ≤ tbreak)
107         k = 1;
108     else
109         k = 2;
110     end
111     NO2(i) = NO2(i-1) + NO2_rate(k)*(time(i)-time(i-1));
112 end

```



```

113
114 C_NO2 = NO2/Vb(1); % moles/Liter
115 C_NO3 = 3/2 .* C_NO2 * 62.0049 * 1000 ; %ppm
116
117 %%%%%%%%%% Correct NO3- to copy %%%%%%%%%%
118 NO22(1) = time(1)*NO2_rate(3)+3/2*NO3_ave(1)/62.0049/1000*Vb(1);
119 for i = 2:length(time)
120     if (time(i) ≤ tbreak)
121         k = 3;
122     else
123         k = 4;
124     end
125     NO22(i) = NO22(i-1) + NO2_rate(k)*(time(i)-time(i-1));
126 end
127
128 C_NO22 = NO22/Vb(1); % moles/Liter
129 C_NO33 = 2/3 .* C_NO22 * 62.0049 * 1000 ; %ppm
130
131 figure (1)
132 hold on
133 %plot(Va_3,pH_24)
134 %plot(Va_3,pH_25)
135 scatter(time_19,pH_ave,'r', 'filled', 'DisplayName','pH ave')
136 %scatter(time_20,pH_UE,'b', 'd', 'DisplayName','Upper Error')
137 %scatter(time_20,pH_LE,'b', 'd', 'DisplayName','Lower Error')
138 % scatter(Va_3,pH_39,'m', '+', 'DisplayName','Exp. 39')
139 % scatter(Va_3,pH_41, '*', 'DisplayName','Exp. 41')
140 % scatter(Va_3,pH_43, 'x', 'DisplayName','Exp. 43')
141 % scatter(Va_6,pH_33,'g', 'h')
142 rate_s = num2str(NO2_rate);
143 mass_s = num2str(Mass_NaHCO3*1000);
144 for i = 1:length(C_NaHCO3)
145     plot(time,pH(i,:), 'DisplayName','NO2 Model')
146 end
147 xlabel('time (minutes)')
148 ylabel('pH')
149 legend('show')
150 text(20,7.6,strcat('d[NO2]/dt = ',rate_s,' mol/min'))
151 text(20,7.55,strcat('NaHCO3 = ',mass_s,' mg'))
152 hold off
153
154 figure (2)
155 hold on
156 for i = 1:length(C_NaHCO3)
157     plot(time,Alk(i,:)*1000, 'DisplayName','NO2 Model')
158 end
159 xlabel('time (minutes)')
160 ylabel('Alkalinity (mg/L)')
161 legend('show')
162 hold off
163
164 figure (3)
165 hold on
166 % % for i = 1:length(C_NaHCO3)
167 %     plot(time,C_NO3(i,:), 'DisplayName','NO2 Model')
168 % end

```

```

169 plot(time,C_NO3)
170 plot(time,C_NO33,'--')
171 scatter(time_19,NO3_ave,'r','filled','DisplayName','NO3- ave')
172 xlabel('time (minutes)')
173 ylabel('NO3- (ppm)')
174 legend('show')
175 hold off

```

```

1 function [ pH ] = pH_curve_fit_MODEL_5(C_NaHCO3,C_NO2,Kw)
2 %UNTITLED3 Summary of this function goes here
3 % NaHCO3 + HNO3 Reaction, Finding [H+]
4
5 %Kw = 1*10^-14;
6 Ka1 = 4.46*10^-7; % [HCO3-][H+]/[H2CO3]
7 Ka2 = 4.69*10^-11; % [CO32-][H+]/[HCO3]
8 Ka = 27.29; % [NO3-][H+]/[HNO3]
9
10
11 % M_NaHCO3 = 1; [grams]
12
13 % C_HCO3 = 10^-3; % NAHCO3 Concentration [Moles/Liters]
14
15
16 % NO2 = time .* NO2_rate; %NO2_init +
17 % C_NO2 = NO2/Vb; % moles/Liter
18 C_NO3 = 2/3 .* C_NO2;
19 % V_t = Va;
20 C1 = C_NaHCO3;
21 % C2 = C_HNO3 * Va/V_t;
22
23
24 F_1 = @(x) (1/Kw)*((10.^(-x)).^2 - ...
    ((C1.*Ka1.*((10.^(-x)).^2))./( (10.^(-x)).^2) + ...
    Ka1.*(10.^(-x)) + Ka1.*Ka2)).*(1+2.*Ka2./(10.^(-x))) - ...
    (10.^(-x)).*(C_NO3-C1) - Kw);
25 %F_1 = @(x) (1/Kw)*((10.^(-x)).^2 + C1.*((10.^(-x)) - ...
    (Ka1.*((10.^(-x)).^2))./( (10.^(-x)).^2)).*(1+2.*Ka2./(10.^(-x)))) ...
    - Kw - C_NO3.*10.^(-x));
26 x0 = 1e-3;
27
28 options = optimset('Display', ...
    'iter','MaxFunEvals',100000,'MaxIter',15000);
29 pH = fsolve(F_1, x0, options);
30
31
32 end

```